Chapter 6

DEVELOPMENT OF ECRF FIELD
MEASUREMENT SYSTEMS

In Mini-RT, directly measurements of electron cyclotron range of frequency (ECRF) electric and magnetic fields have been carried out to identify whether the EBW heating is a promising and an actual mechanism of producing overdense plasmas in the dipole magnetic field [86]. On the steady injection experiments, the profiles of ECRF electric and magnetic field from which one can evaluate a wavelength, a polarization, a phase velocity and a Poynting vector, which corresponds to the energy flux of electromagnetic modes, can be obtained. On the other hand, the pulse injection experiments, one can directly obtain the direction of energy the flux, which corresponds to the group velocity, of both of electromagnetic and electrostatic (longitudinal) modes. Therefore, ECRF field measurements provide the characteristics of waves in a Mini-RT plasma, especially that in an overdense plasma.

6.1 Principles of Diagnostics in Mini-RT

6.1.1 Schematic Diagram of Steady Injection Experiments

Interferometry enables one to obtain a snapshot of the profiles of an electric or a magnetic field [5]. Figure 6.1 shows the schematic diagram of diagnostics. This system has 3 oscillators, which are synchronized by a Phase Locked Loop (PLL) [65].

One oscillator, named LO1, sends a microwave signal to excitation antennas with frequency of 1—2.1 GHz (100 MHz step). A variable attenuator (V-att, 10 dBc, 1dBc step) and a phase
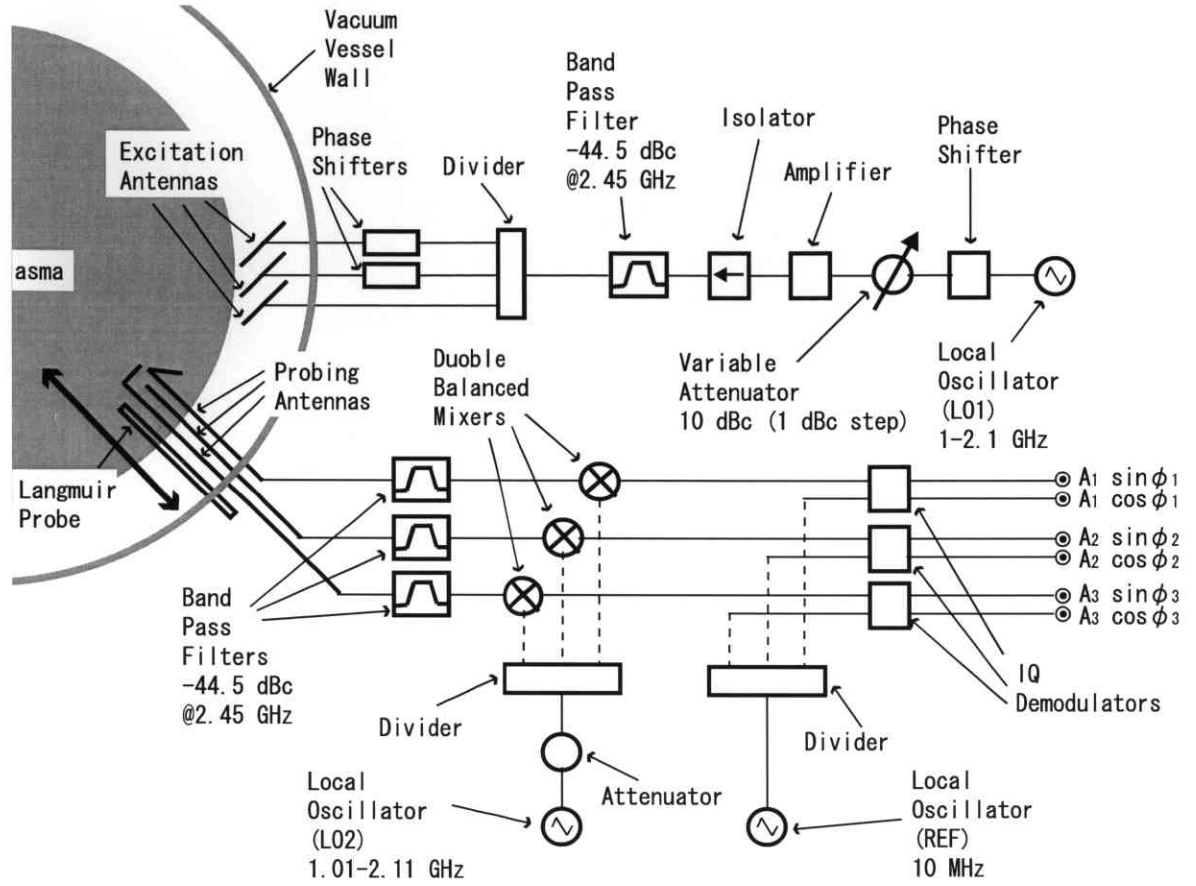
Figure 6.1: Schematic diagram of the steady injection experiments.

shifter control the injection power and phase, respectively. The microwave signal is amplified by an amplifier up to a power level of 10 W, and is launched from excitation antennas. Figure 6.2 shows the excitation unit, which contains the LO1, a phase shifter, an amplifier and an isolator. A microwave with 2.45 GHz and 2.5 kW produces and heats a plasma, thus the diagnostic microwave does not affect to plasma heating.

Probing antennas detect the injected signals and send it to a mixer. The second oscillator, named LO2, is connected to the mixer's second leg with frequency of 1.01—2.11 GHz (100 MHz step). One has to lock the difference of the frequency between LO1 and LO2 to 10 MHz. By using an IQ demodulator, one can obtain the two signals , i.e. $A\cos\phi$ and $A\sin\phi$, where A and ϕ are the amplitude of signal detected by a probing antenna and its phase, respectively. Figure 6.3 shows the receiver unit, which contains three mixers, two local oscillators (one of them has 1.01-2.11 GHz (100 MHz step), and the other has 10 MHz) and three IQ demodulators. Furthermore, the phase ϕ can be written as $\phi(\mathbf{r}) + \phi_{ph}$ where $\phi(\mathbf{r})$ represents the phase of the measurement point and ϕ_{ph} depends on the length of a transmission line.
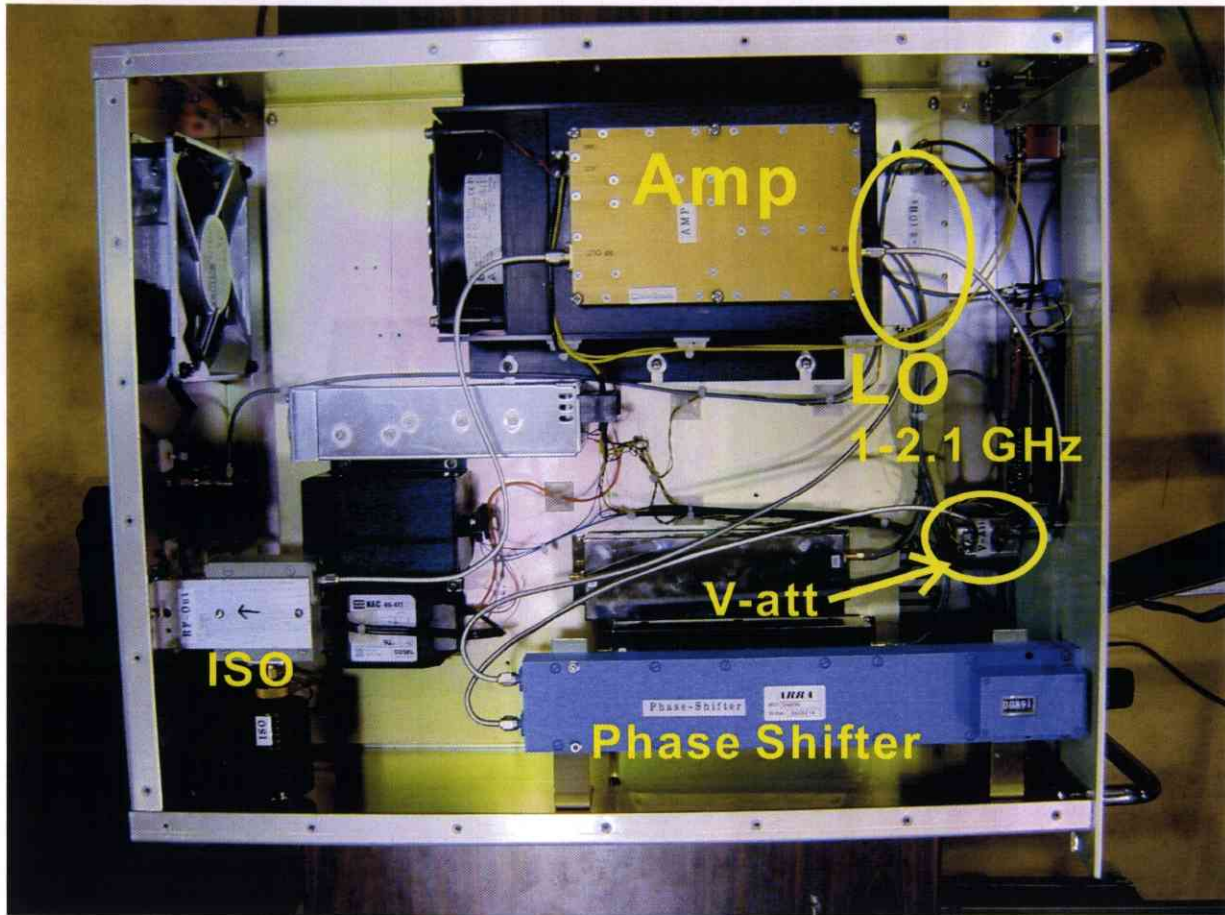
Figure 6.2: A photograph of the excitation unit. Signals excited by a Local Oscillator is sent to excitation antennas via a Band Pass Filter.

By changing the phase of the microwave launched from the excitation antennas with a phase shifter, one can obtain a snapshot of ECRF signals of any phase in a period. Figure 6.4 shows output signals of an IQ demodulator. In this figure, results with frequencies of 1.0, 1.5 and 2.0 GHz are shown, where horizontal and vertical axis denote the indicator of a phase shifter and an output signal. One can see that each signal can be fitted by a sinusoidal function, moreover, the period is inversely proportional to a frequency. In addition, Fig. 6.4(b) shows the phase of this signal, i.e. the argument of it corresponds to the phase. One can see that when the length of a transmission line is increased, i.e. it corresponds to the increasing of an indicator of a phase shifter, the phase decreases. As shown in Fig. 6.1, the phase shifter is set at the front side of excitation antennas, so that the increment of the indicator of the phase shifter corresponds to the interference between reference signal and delayed one. Thus one can understand that the gradient of a phase corresponds to the direction of a phase velocity because a larger phase represents a more advanced arrival of a signal.
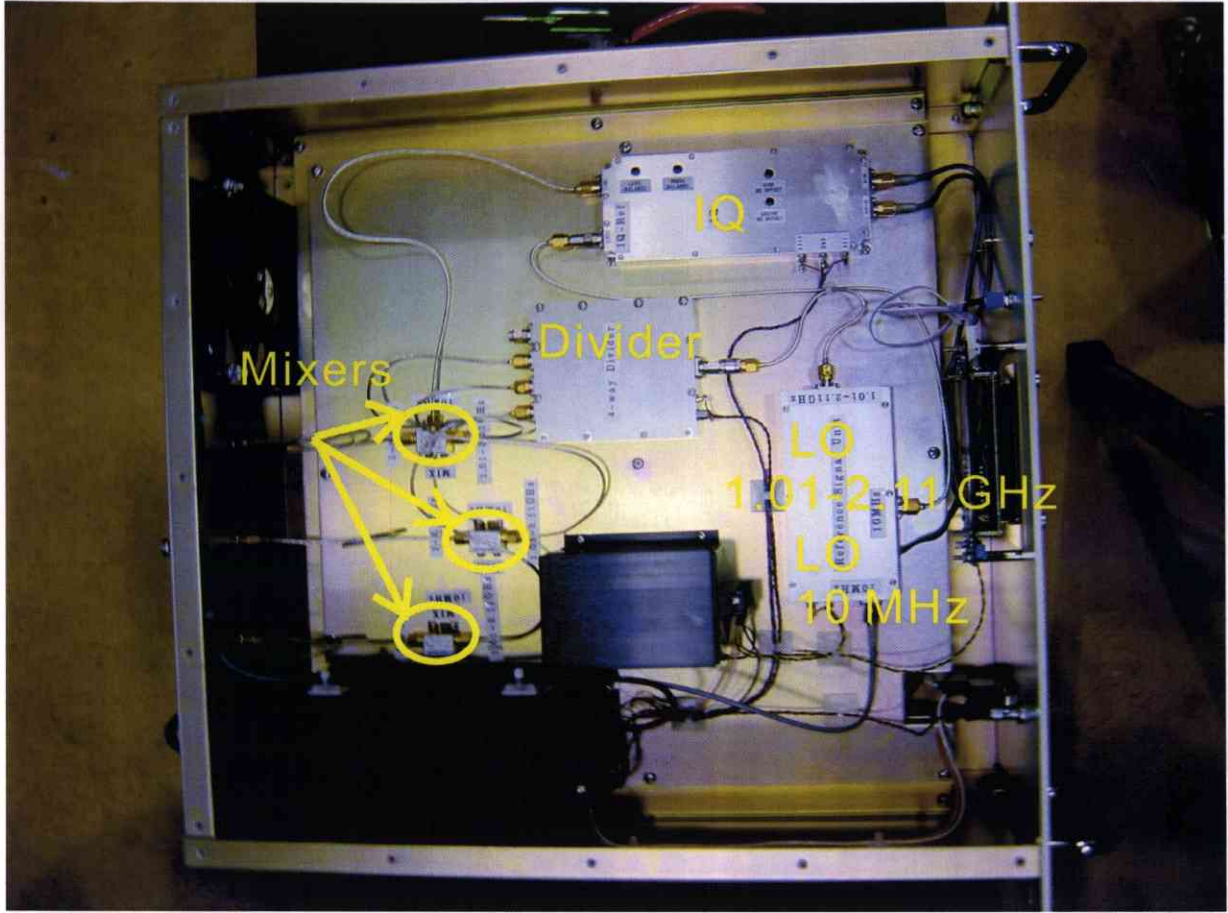
Figure 6.3: A photograph of the receiver unit. A received signals is interferenced at a mixer and is down-converted to 10 MHz. The phase of this output signal can be obtained by an IQ demodulator. Since this system has three channels, three mixers and three IQ demodulators are used simultaneously and independently.

By changing a frequency of the diagnostic microwave, we can investigate wave characteristics for various plasma conditions such as an overdense and a low-density plasmas for the same discharge condition. Since the O and X modes are governed by the ratio of wave (angular) frequency to plasma frequency ω_{pe} (O-wave) or to left hand frequency ω_L (X-wave), the wave propagation characteristics can be studied by sweeping of the frequency of the diagnostic microwave. Such frequencies are determined by the electron density and the magnetic field strength.
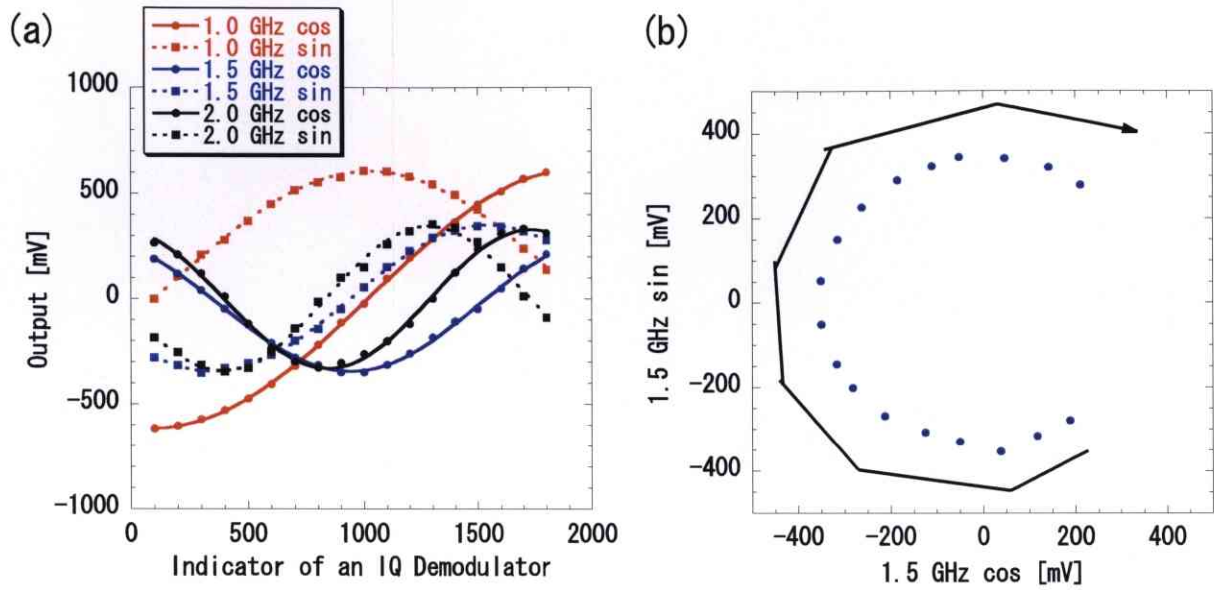
Figure 6.4: Examples of an IQ demodulator signal; (a) shows raw data of three, i.e. 1.0 GHz, 1.5 GHz and 2.0 GHz, frequencies, and (b) shows the polar plot of the 1.5 GHz in (a). Here, for this test, the transmission line is short-circuited via an attenuator of 40 dBc. An arrow in (b) represents the direction when the indicator of an IQ demodulator is increased, which corresponds to increasing of a length of the transmission line.
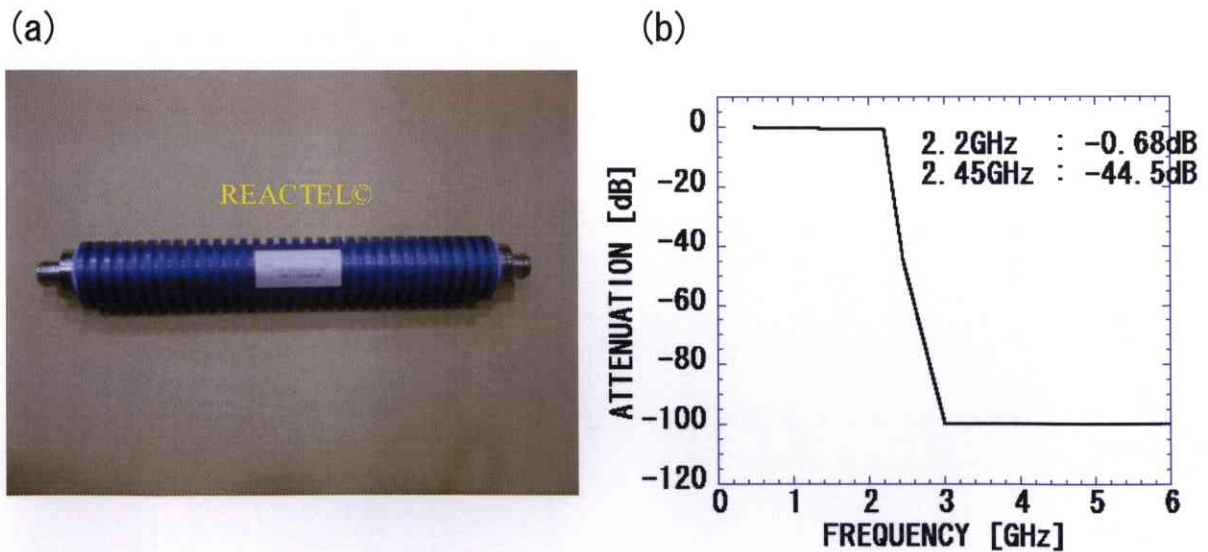

Figure 6.5: A photograph of Band Pass Filter is shown in (a), and the frequency characteristics of it is shown in (b), respectively.

A Band Pass Filter (BPF) prevents the 2.45 GHz ECH microwave for the plasma production from penetrating the diagnostic circuits (see Fig. 6.5 (a)). Since we investigate frequency of 1-2.1 GHz, which is nearly as high as 2.45 GHz, BPFs need to have a steep enough frequency characteristic to pass 2.1 GHz and cut 2.45 GHz effectively. BPFs have the frequency characteristic of -0.68 dBc at 2.2 GHz, -44.5 dBc at 2.45 GHz and -100 dBc at 3.0 GHz (see Fig. 6.5 (b)). If one assumes all the power of the heating microwave with power of 2.5 kW, i.e. +64 dBm, is sent to a BPF, only $\sim$100 mW, i.e. 20 dBm, of power penetrates into the circuit.

6.1.2 Poynting Vector Measurements

If an electromagnetic field can be described by a propagating wave, the direction of the Poynting vector is conserved, and it corresponds to the direction of an energy flux of an electromagnetic wave. On the other hand, if it can be described by a standing wave, the direction of the Poynting vector vibrates. From the temporal variation of a Poynting vector, one can obtain a reflection coefficient of an injected wave. If the mode-conversion efficiency is around unity, little proportion of an injected wave is reflected, thus it is expected that there are correlations between the reflection coefficient and the mode-conversion efficiency.

For simplicity, we consider one-dimensional case. Let the directions of magnetic field, wavenumber vector be z direction and x direction, respectively. The electric field of an X-wave has y components, and the magnetic field of it has z components. The electric field can be written as

$$
\begin{aligned}
E_y &= A \sin\left(\int_{R_0}^{x} k \mathrm{d}x - \omega t + \phi_1\right) + \alpha A \sin\left(\int_{R_0}^{x} (-k \mathrm{d}x) - \omega t + \phi_2\right), \\
&= A\sqrt{(1+\alpha^2) + 2\alpha \cos\left(2\int_{R_0}^{x} k \mathrm{d}x + \phi_1 - \phi_2\right)} \\
&\quad \times \sin\left[-\omega t + \frac{\phi_1 + \phi_2}{2} + \tan^{-1}\left(\frac{1-\alpha}{1+\alpha}\tan\left[\int_{R_0}^{x} k \mathrm{d}x + \frac{\phi_1 - \phi_2}{2}\right]\right)\right], \quad (6.1)
\end{aligned}
$$

where A, α, k, R_0, ϕ_1 and ϕ_2 denote an amplitude, a reflection coefficient, a wavenumber, the reference position, a phase factor of an injected wave at R_0 and that of a reflected wave at there, respectively. The magnetic field can be derived from Maxwell equation (Eq. (A.25)):

$$
\begin{aligned}
B_z &= \frac{k}{\omega} A\sqrt{(1+\alpha^2) + 2\alpha \cos\left(2\int_{R_0}^{x} k \mathrm{d}x + \phi_1 - \phi_2\right)} \\
&\quad \times \sin\left[-\omega t + \frac{\phi_1 + \phi_2}{2} + \tan^{-1}\left(\frac{1+\alpha}{1-\alpha}\tan\left[\int_{R_0}^{x} k \mathrm{d}x + \frac{\phi_1 - \phi_2}{2}\right]\right)\right]. \quad (6.2)
\end{aligned}
$$

Therefore the Poynting vector can be represented as

$$Y_x = \frac{kA^2}{2\mu_0\omega}\left[(1+\alpha^2)+2\alpha\cos\left(2\int_{R_0}^x k\mathrm{d}x+\phi_1-\phi_2\right)\right]$$
$$\times\left[\cos\left(\theta_E-\theta_B\right)-\cos\left(-2\omega t+\phi_1+\phi_2+\theta_E+\theta_B\right)\right], \tag{6.3}$$

where θ_E and θ_B is written as

$$\theta_E = \tan^{-1}\left(\frac{1-\alpha}{1+\alpha}\tan\left[\int_{R_0}^x k\mathrm{d}x+\frac{\phi_1-\phi_2}{2}\right]\right), \tag{6.4}$$

$$\theta_B = \tan^{-1}\left(\frac{1+\alpha}{1-\alpha}\tan\left[\int_{R_0}^x k\mathrm{d}x+\frac{\phi_1-\phi_2}{2}\right]\right). \tag{6.5}$$

If the parameter α equals to 0, i.e. mode-conversion or absorption occurs efficiently, Eq. (6.3) is represented as

$$Y_x = \frac{kA^2}{2\mu_0\omega}\cos^2\left(\int_{R_0}^x k\mathrm{d}x-\omega t+\phi_1\right). \tag{6.6}$$

On the other hand, if the parameter α equals to unity, i.e. completely reflected, it is

$$Y_x = -\frac{kA^2}{2\mu_0\omega}\cos^2\left(\int_{R_0}^x k\mathrm{d}x+\frac{\phi_1+\phi_2}{2}\right)$$
$$\times\cos\left(-2\omega t+\phi_1+\phi_2+\frac{\pi}{2}\right). \tag{6.7}$$

Obviously, in order to measure a Poynting vector, an ECRF magnetic field measurement is necessary. ECRF magnetic field measurement and electric one use common circuit system. The only difference is the shape of antennas, i.e. monopole or dipole antennas are used for an electric field measurement whereas loop antennas are used for a magnetic field measurement.

6.1.3 Pulse Injection Experiments for the Direct Evaluation of a Group Velocity

It is well known that a group velocity is equivalent to a velocity of an energy flux. By injecting a pulse signal and detecting the spacial dependence of arrival time of it, one can obtain an energy flux velocity experimentally. In order to carry out the pulse injection experiments, we used a PIN diode switch which opens when the gate signal exceeds a threshold voltage. Unfortunately, the switch used in this research does not have a sufficiently short time constant to flatten the transmitted pulse, and it is quite difficult to make a flat gate signal of the order of nanosecond. Figure 6.6 shows the comparison between the steady and the pulse injection experiments. The only difference between these two experiments is whether the PIN diode

91

switch is assembled or not; Fig. 6.7 shows a photograph of a switch and a circuit of generating a gate signal. Moreover, Fig. 6.8 shows the circuit of the pulse injection system. By connecting the manual trigger switch (see Fig. 6.7), which lies around A in Fig. 6.8, one can send the trigger signal to two transistor-transistor logics (TTLs), which correspond to B and C in Fig. 6.8. And the output signals from these two TTLs are fed to another TTL (D in Fig. 6.8), i.e. SN74ALS00AL, which outputs a low level signal when both of the two input signals are high level. This signal is divided and be sent to PIN Diode Switch and an oscilloscope via buffers. The signal sent to an oscilloscope corresponds to a trigger signal of this measurement, and the sampling rate of the oscilloscope is 20 GS/s (maximum), which enables one to observe a waveform of microwave with frequency of the order of GHz directly. Figure 6.9 shows two examples of a pulse generation. An output signal from B never change, whereas it from C is changed by resistance of a potentiometer. The output form D corresponds to the gate signal, which outputs high-level when both of B and C are high-level, then PIN diode switch opens.
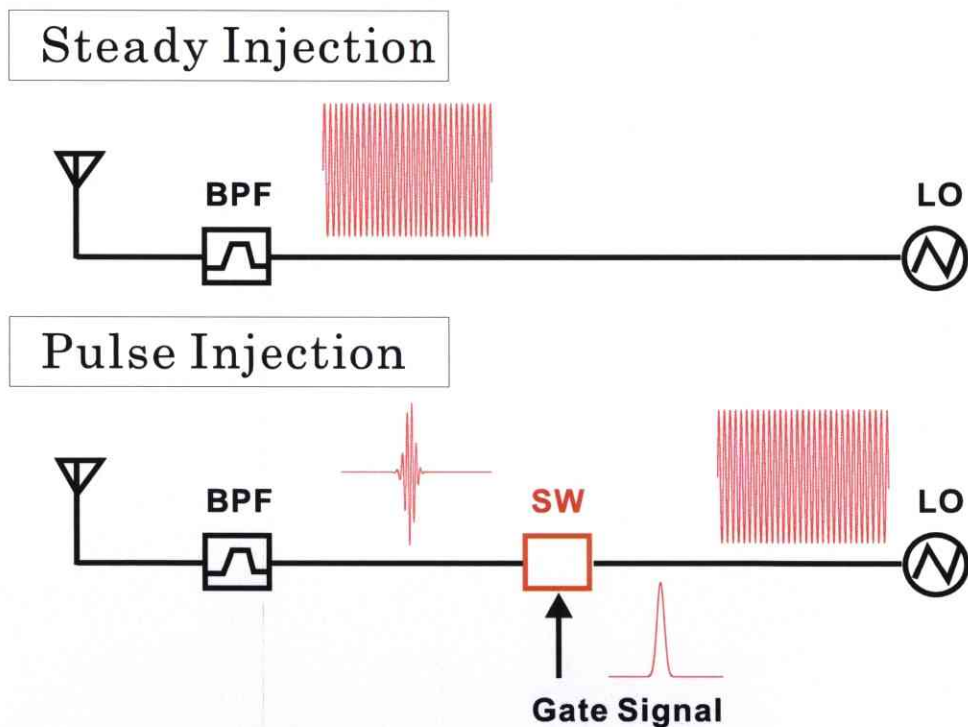

Figure 6.6: Comparison between a steady injection and a pulse injection experiments.
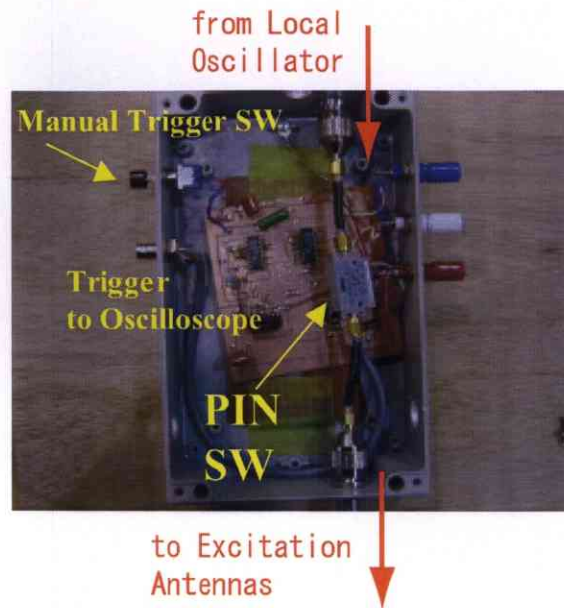
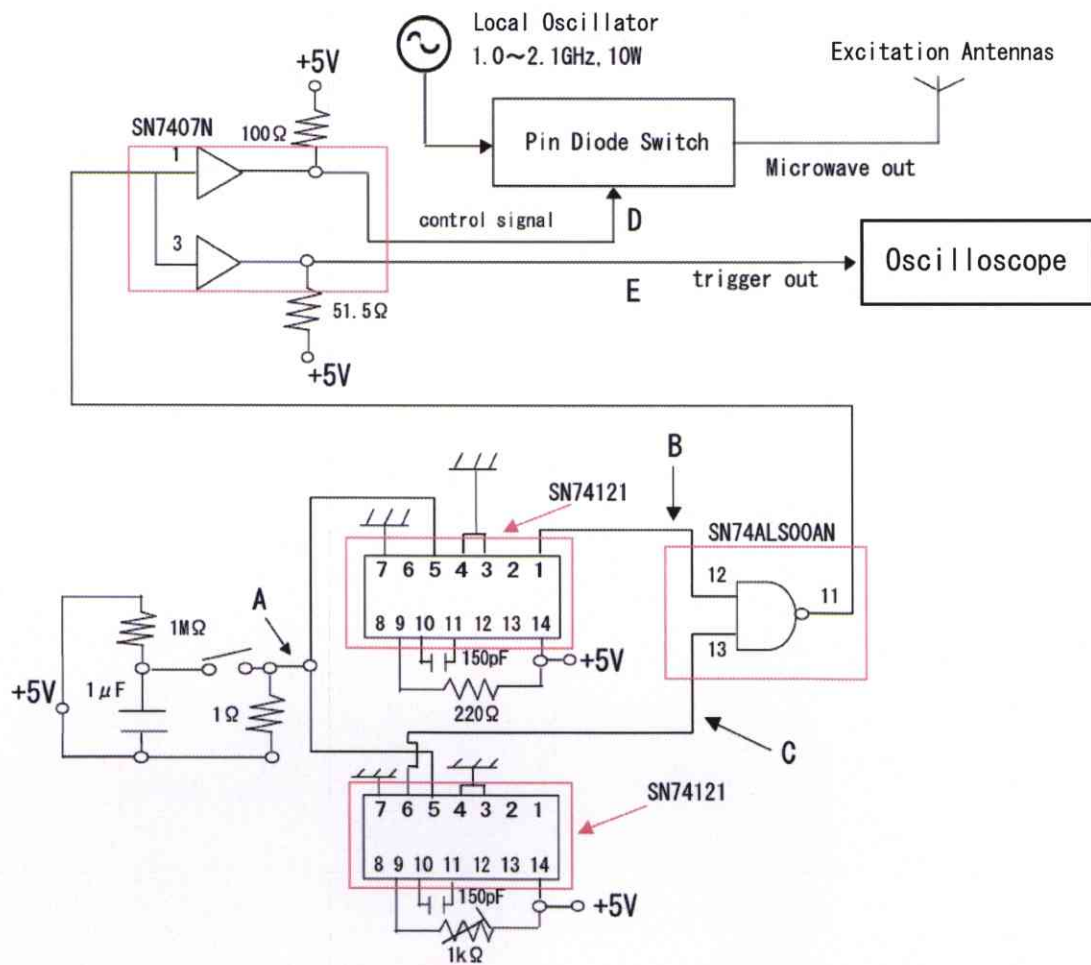Figure 6.7: A photograph of a switch of the pulse injection experiments.

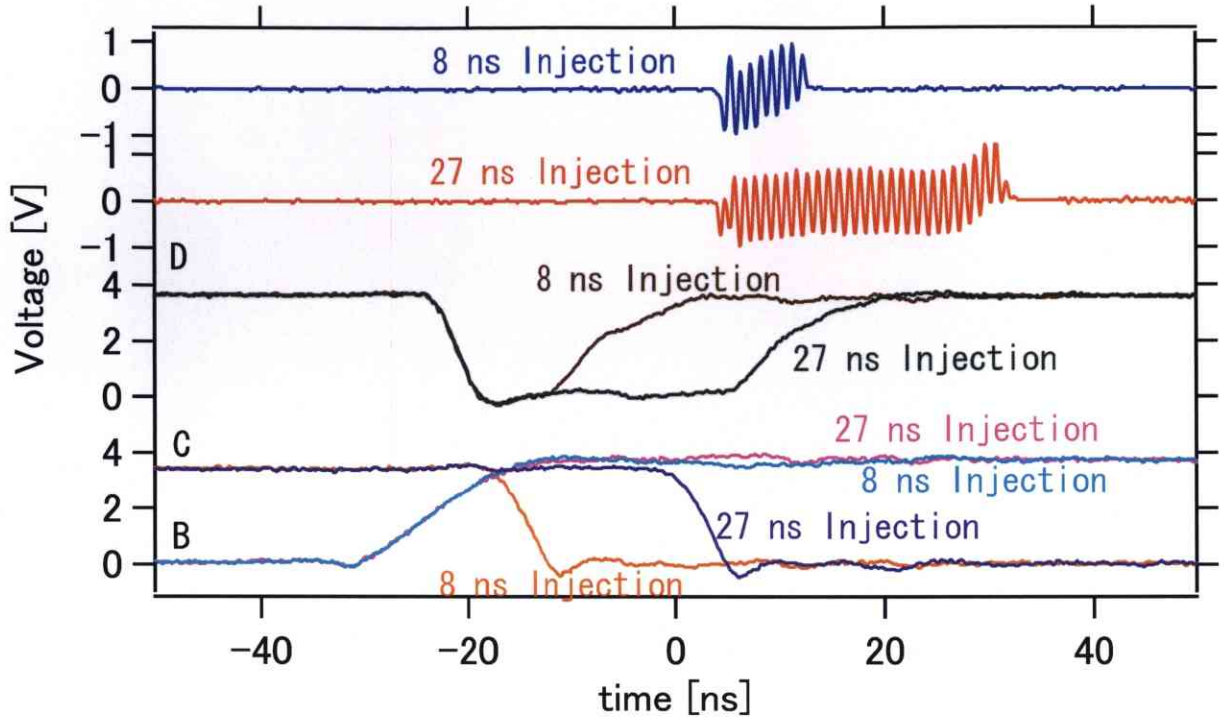Figure 6.8: The circuit of the pulse generator.

Figure 6.9: Examples of a pulse injection. The time-lug of an output of a pulse microwave from a gate signal is due to the difference of a length of a measurement cable.

6.2 Excitation Antennas

Dipole antennas were adopted for excitation antennas because of the flexibility of interconnection between antenna elements and the diagnostic circuit. Design of excitation antennas has been carried out as follows. As described in Sec. 3.4, in Mini-RT, the X-wave injection from low field side is expected to be the most efficient methods for excitation of an EBW from electromagnetic mode. Therefore, excitation antennas have to fulfill the following three demands. At first, antennas have to be set at the low field side of a plasma. Second, antennas inject microwaves with the extraordinary (X) polarization. Magnetic field directs the poloidal direction, and what we investigate is the wave propagating into a plasma core across the magnetic flux (radial direction). Thus an ECRF electric field excited by antennas need to direct toroidal direction. Third, the excited X-wave propagates perpendicular to the magnetic field.

Excitation antennas are located at $R = 450$ mm on the mid-plane. Since antennas are set in the vacuum vessel, one should protect antennas from touching by a plasma. A feeder cable is protected by an Alumina (Al_2O_3) tube, and an antenna element is sheathed in ceramic glue. Figures 6.10 and 6.11 show photographs of an antenna element before and after ceramic sheath, respectively.

Figure 6.10: Photograph of an excitation antenna element, which is made of copper.
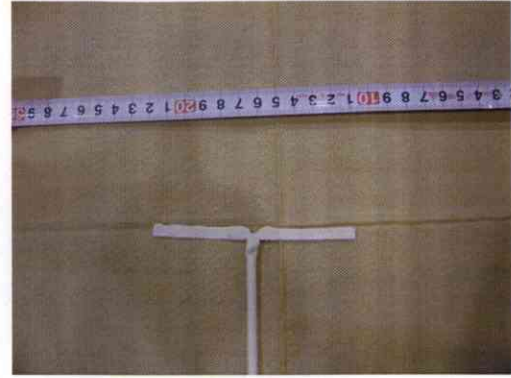

Figure 6.11: An excitation antenna element sheathed in ceramic glue.

A polarization of an excited wave is determined by the direction of an antenna element. In order to check whether an excitation antenna used in Mini-RT produces a pure linear polarization, a polarization selectivity has been measured experimentally. Figure 6.12 shows the polarization selectivity of a dipole antenna used in Mini-RT. The abscissa denotes an external phase given by a phase shifter, and the ordinate denotes the output of cosine and sine signals. One can evaluate the amplitude from a cosine signal by sinusoidal fitting. Parallel and perpendicular mean the experimental conditions, i.e. fixed half-wavelength dipole antenna excite microwaves, and another antenna, which has been used as excitation antenna in Mini-RT, directs its element parallel or perpendicular to the fixed antenna. Figure 6.12 shows an almost linear polarization since the amplitude of a detected signal in the case of parallel antennas is ten times larger than that of perpendicular antennas.

The phasing of multiple antennas enables one to control the direction of launching. This technique has been adopted to a lower hybrid wave current drive (LHCD) and an ion Bernstein wave (IBW) excitation, and so on [9][53][54]. In order to launch electromagnetic waves perpendicular to the magnetic field, antennas need to be located parallel to the magnetic field and phases of them should be matched. Finiteness of an antenna width causes the spreading of the $k_{//}$ spectrum, where $k_{//}$ denotes a wavenumber parallel to the magnetic field. Let the width of an excitation antenna element and the distance between each antenna be d and a. If the amplitude of the antenna currents are same, antenna currents are represented as

$$j(x) = \begin{cases} Je^{inqa} & (na - d/2 \leq x \leq na + d/2) \\ 0 & (\text{others}) \end{cases}, \tag{6.8}$$
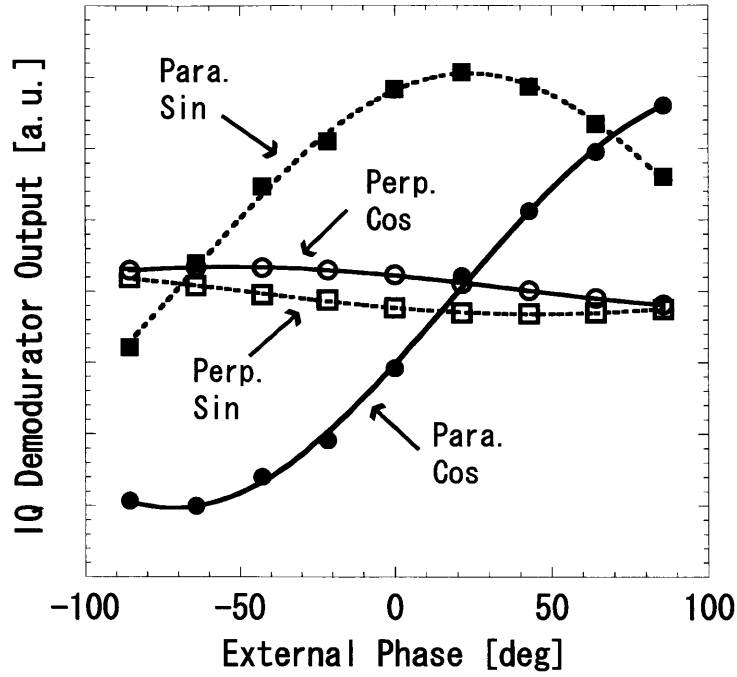
95

Figure 6.12: Polarization selectivity of an excitation antenna; parallel and perpendicular mean the relative direction between fixed reference antenna and testing (excitation) antenna. In the parallel case, amplitude is approximately ten times larger than that in the perpendicular case.

where n, J and qa denote an integer, an amplitude of an antenna current and a phase difference between adjacent antennas (see Fig. 6.13). Therefore the Fourier transformation of it is

$$
\begin{aligned}
j(k) &= \int_{-\infty}^{\infty} dx e^{ikx} j(x) \\
&= J \sum_{n=n'}^{n''} e^{inqa} \int_{na-d/2}^{na+d/2} dx e^{ikx} \\
&= Jd \frac{\sin(kd/2)}{kd/2} \frac{e^{i\frac{n'+n''}{2}(k+q)a} + \sin\frac{n''-n'+1}{2}(k+q)a}{\sin\frac{k+d}{2}a},
\end{aligned}
\tag{6.9}
$$

where n' and n'' are also integers, i.e. $n'' - n' + 1$ is the number of antenna element pieces, thus

$$
j(k)j^*(k) = JJ^* \frac{\sin^2(kd/2)}{(kd/2)^2} \frac{\sin^2(\frac{n''-n'+1}{2}(k+q)a)}{\sin^2(\frac{k+q}{2}a)}.
\tag{6.10}
$$

In Fig. 6.14(a), a wave spectrum is shown for different antenna numbers, where the distance between antenna elements a is fixed to twice of the antenna element width d. We can see that the wave spectrum becomes narrower as the antenna number is increased, and an antenna system with more than three elements might be necessary. Next, the effect of the distance

96

between adjacent antennas on the wave spectrum is calculated in Fig. 6.14(b), where three antennas are employed. We can see that the side band of the wave spectrum cannot be neglected, with increased distance. From these considerations, three dipole antennas were introduced in Mini-RT, and the distance between these antennas were fixed to be a/d of 5/3 with an antenna element width d of 6 mm. Figure 6.15 shows the drawing of the excitation antenna system. Antenna elements are arranged not to be interfered by elements themselves, and they are coated by ceramic glue. Feeder lines are made of semi-rigid co-axial cables and coated by ceramic tubes, and they are connected to transmission line by BNC connectors.
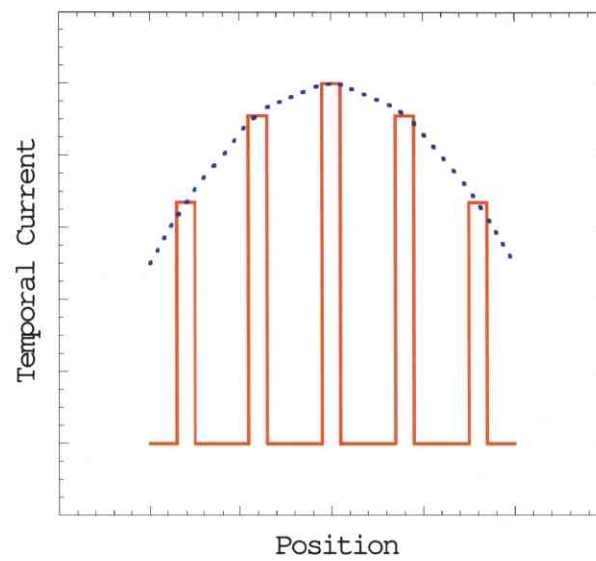
Figure 6.13: Spacial distribution of antenna current: In this figure, five antennas case with $a/d = 4$ and $qa = \pi/7.5$.

Figure 6.14: Relations between antenna configuration and power spectrum. (a) Increment of the number of antennas reduces the spectrum broadening. (b) Parameter a and d denote the distance between antennas and antenna element width. Separating the distance between antennas leads to high-level sidebands.

Figure 6.15: Drawing of the excitation antennas.

6.3 Probing Antennas
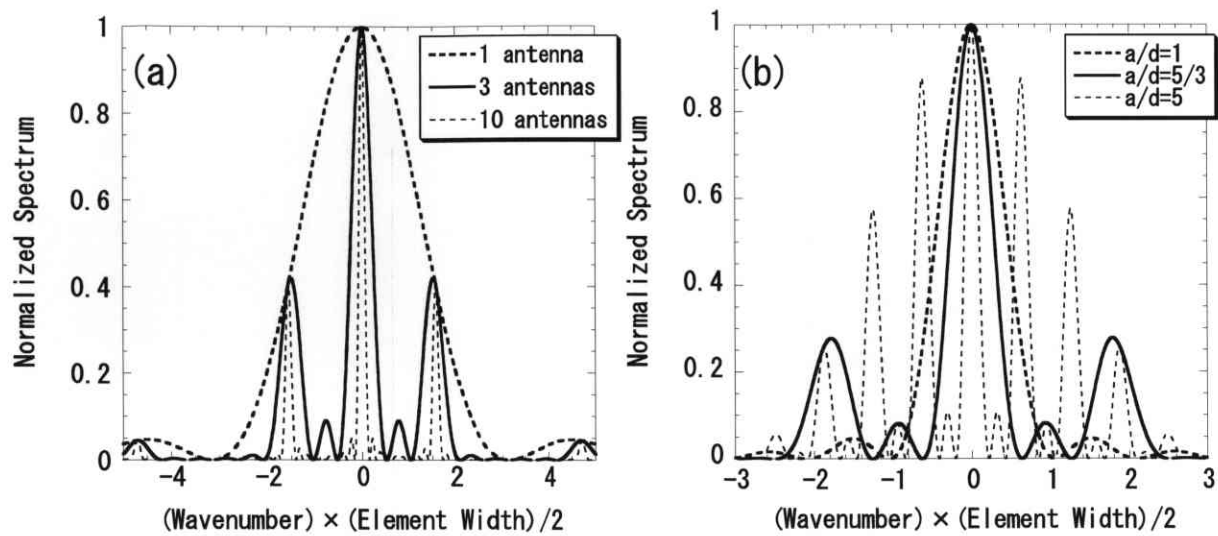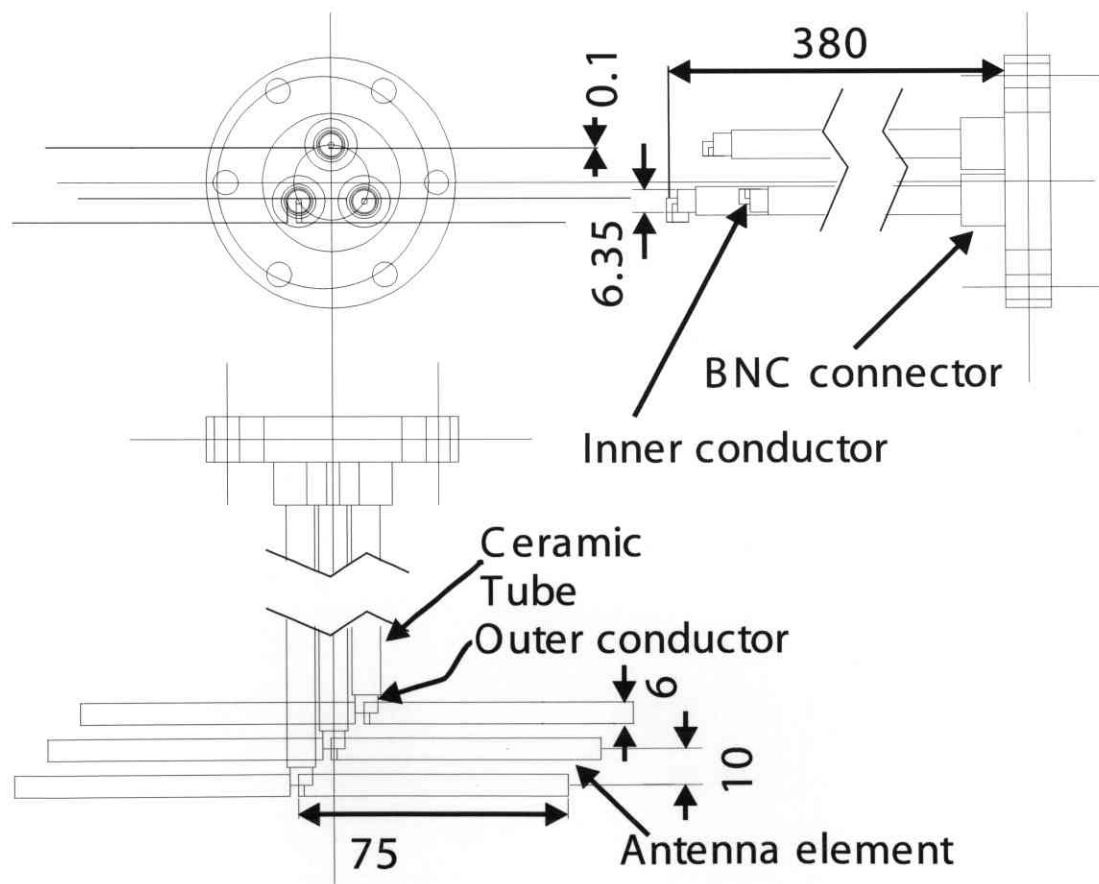
6.3.1 For the ECRF Electric Field Measurements

The ECRF electric field is directly measured with the probing antennas inserted inside a torus plasma. These antennas should hold a high selectivity of polarization for an ECRF electric field. However, so as to keep a high spatial resolution for the measurement, a small antenna is requisite for the probing antenna. The polarization selectivities of the antennas, which is hereafter defined by the ratio of the amplitude of two signals when the source antenna is parallel and perpendicular to the testing one, are experimentally examined in Fig. 6.16, where the 1 GHz of frequency, a half-wavelength dipole antenna as source one are used for this calibration. We can see that a quarter-wavelength antenna has a high selectivity. Here we employed a monopole antenna with a length of 35 mm. Although the resolution between different components of the electric field is not so superior, the separation of the poloidal (O-wave) and toroidal (X-wave) components of an ECRF electric field could be available with this type of an antenna. Elements of these monopole antennas are straight rods with 35 mm of a length. When an element is directed to the toroidal direction, the difference of radial positions of antenna head and end is evaluated to be 2 mm when an antenna end lies at $R = 300$ mm. In the poloidal direction, this special difference is smaller because the magnetic field directs approximately to the poloidal direction on the mid-plane. To measure a radial component of the electric field, a small tip electrode with a length of 1 mm is prepared, so as to ensure a high spatial resolution. This electrode is not sheathed in an insulator like a ceramic. This is just an electrostatic probe, and has no polarization selectivity on the electromagnetic field. These three components of ECRF electric field can be measured simultaneously in plasma. Figures 6.17 and 6.18 show the allocations of antennas and a triple probe in vacuum vessel and a photograph of antennas.

Dipole antennas were also adopted for an ECRF electric field measurement. An element length is 40 mm, i.e. one side of it is 20 mm. In Chap. 7, several experimental results in Mini-RT are shown with above mentioned two types of probing antennas. Thus the author mentions every time that which antenna is used in that experiment.
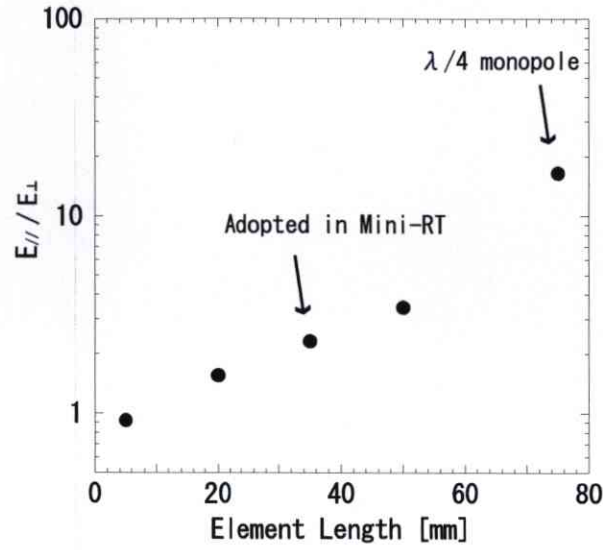
Figure 6.16: Polarization selectivity of a probing antenna; Short (5 mm) monopole antenna does not have selectivity, whereas quarter-wavelength monopole antenna has high selectivity.
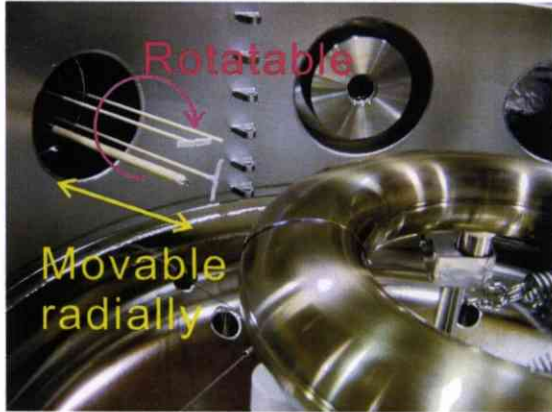
Figure 6.17: Photograph of the allocation of the antennas and a triple probe.
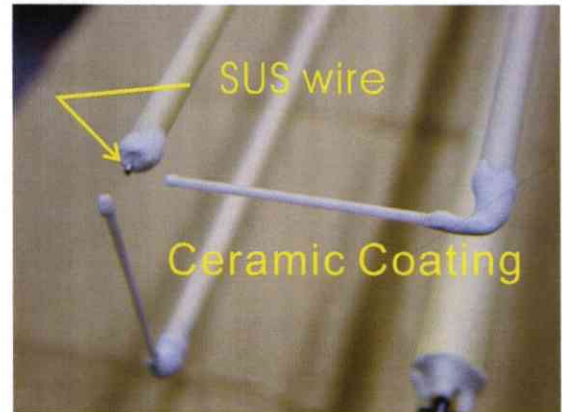
Figure 6.18: Photograph of the head of the probing antennas.

6.3.2 For the ECRF Magnetic Field Measurements

Small loop antennas were adopted for an ECRF magnetic field measurement. If a radius of a loop antenna is sufficiently smaller than a wavelength, one can consider a loop antenna as a magnetic dipole. Since the conductivity of copper is 6×10^7 m/Ω, the skin depth of the outer conductor of a loop antenna for a 1 GHz microwave δ is 0.58 μm. Therefore by shortening the gap length of an element, one can obtain signals only from the variation of the magnetic field. In addition by locating the gap at the center of a loop, one can avoid the unbalanced

feed. Figure 6.19 shows a schematic drawing of a loop antenna in Mini-RT. At the end of a loop, outer conductor of a semi-rigid cable and a copper tube are welded, and at the center of it, inner conductor of a semi-rigid cable and a copper tube is connected. The shape of a loop is a square 10 mm on a side. Inner and outer conductor of a semi-rigid cable are 0.32 mm and 1.6 mm, respectively, and an insulator of them is a Teflon. Whole this cable is coated by a ceramic. Figures 6.20 and 6.21 show photographs of a loop antenna in Mini-RT before and after the coating by a ceramic.

Figure 6.19: Schematic drawing of a loop antenna on Mini-RT.

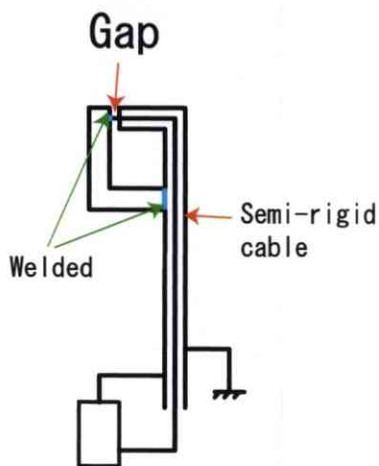Figure 6.20: Photograph of a loop antenna element before ceramic coating.

Figure 6.21: Photograph of a loop antenna element after ceramic coating.
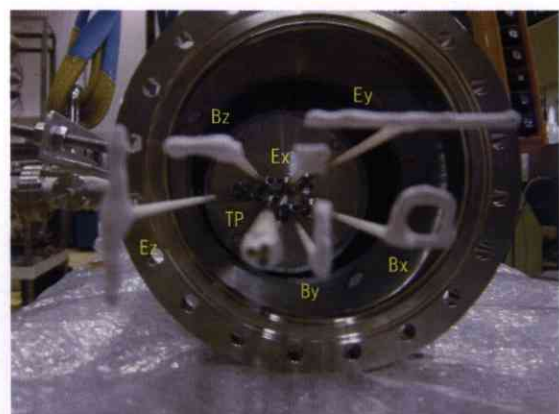

Figure 6.22: Photograph of the modified probing antenna system.

Three loop antennas are fixed to the manipulator with two dipole antennas, an electrostatic antenna and a triple probe. Figure 6.22 shows a photograph of antennas of the simultaneously ECRF electric and magnetic field measurement system. Here x, y, z is defined as radial, toroidal and poloidal direction, respectively.

If a time constant of a measurement circuit is longer than a signal, the waveform skews. Sinusoidal wave is turned down its amplitude and delayed its phase due to a long time constant of a measurement circuit, i.e. the shape of a signal is not changed. The self-inductance L of a square loop antenna is written as

$$L = 8a \left(\ln \frac{2a}{r} - 1.467 \right) \quad [\mu\text{H}], \tag{6.11}$$

where a and r denote a side length and a radius of an antenna element, respectively. Therefore it is 85 nH. The time constant of the measurement circuit on Mini-RT is 1.7 ns, where the characteristic impedance of it is 50 Ω. This time constant is as fast as a period of a diagnostic microwave, so that the calibration of a phase is a crucial issue. However the absolute calibration of a phase of an ECRF electric and magnetic field has not been established yet.

6.3.3 For the Pulse Injection Experiments

Since an EBW is an electrostatic mode, an above mentioned small tip (1 mm) antenna was used for a pulse detection. However the amplitude of signal is so small that we used a center-fed square antenna whose length of a side is 6 mm. In addition, this antenna is sheathed in ceramic glue, whereas a small tip antenna is not be done. This antenna detects a mirror charge at an element. Whether an antenna element is sheathed in an insulator or not gives essentially no difference. Figures 6.23 and 6.24 show photographs of a center-fed square antenna before and after ceramic coating, respectively.

By feeding at the center of an element, one can approximately cancel an induction current due to an electromagnetic (transverse) signal. It enables one to detect a fluctuation of the charge due to an electrostatic (longitudinal) wave. However relatively small signal from an electromagnetic wave remains. We compared the amplitude of signal between a center-fed square antenna and a usual, i.e. the edge, fed one. As the result the latter one was about 10 times larger than the former one. Thus we considered this antenna detects an electrostatic signal selectively.
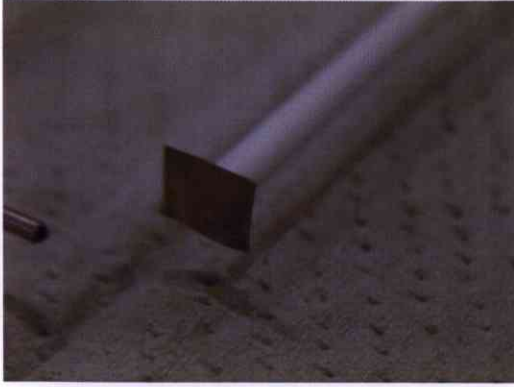
Figure 6.23: Photograph of a center-fed antenna before ceramic coating.

Figure 6.24: Photograph of a center-fed antenna after ceramic coating.

6.4 Verification of the Measurement Principles

Signals measured with the probing antenna include information of the amplitude and the phase of the electric field. By utilizing the IQ demodulator, the amplitude and phase can be derived from two output signals, i.e. cosine and sine components. Figure 6.25 shows the waveforms in vacuum, where suffixes 1, 2 and 3 correspond to electrostatic, poloidal (parallel to the magnetic field) and toroidal (perpendicular to the magnetic field) components of ECRF electric field, respectively. The wave frequency is 1.2 GHz. Cosine and sine components derive the amplitude and the phase of the signal as follows,

$$X = A\cos\phi,$$

$$Y = A\sin\phi,$$

$$A = \sqrt{X^2 + Y^2},$$

$$\phi = \mathrm{sgn}Y\tan^{-1}(Y/X), \tag{6.12}$$

where X, Y, A and ϕ denote cosine and sine components of signal, amplitude and phase, respectively. Figure 6.26 shows the amplitude and the phase profile of ECRF electric field derived from channel 2 of Fig. 6.25. The wavelengths measured are comparable to that in vacuum, i.e. 250 mm.

The validity of our diagnostics system was examined in more detail. Figure 6.27 shows profiles of cosine component, where black lines are results in the case that the phase is artificially changed, whereas red lines correspond to reconstruction data from the amplitude and the phase profiles in 6.26. We could see a fairly good agreement of the experimental data with reconstruction ones.
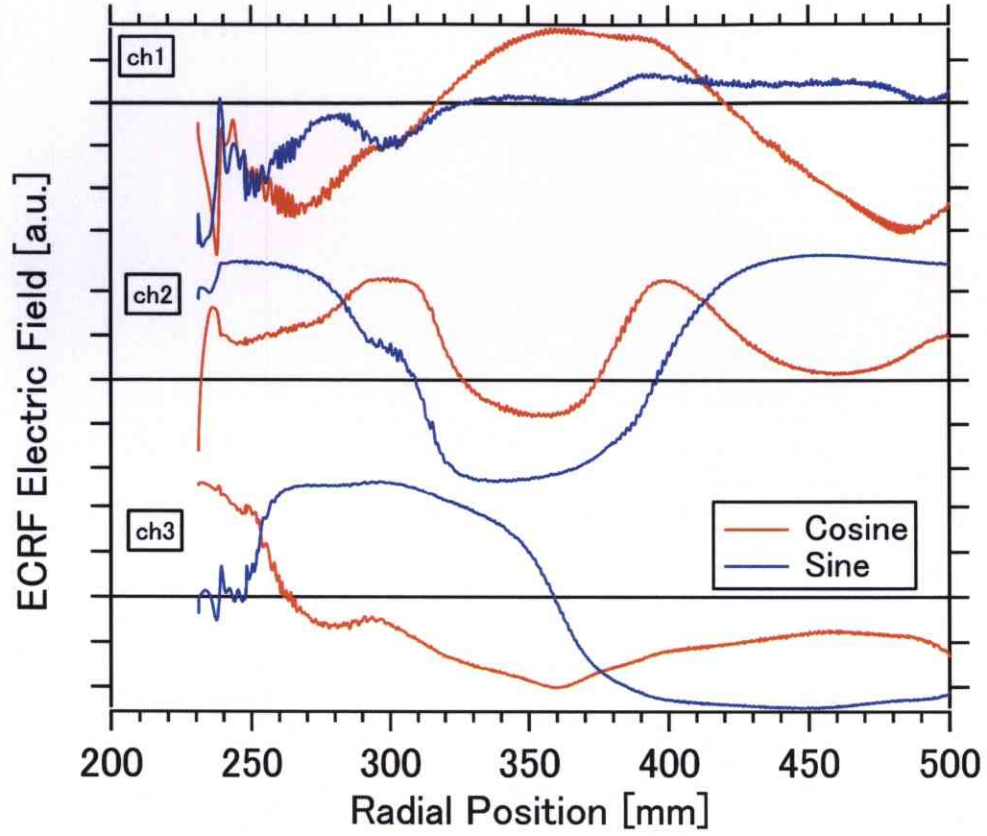
Figure 6.25: Cosine and sine signals of each channel, (ch1) rf electrostatic potential, (ch2) poloidal (Ordinary) component, (ch3) toroidal (eXtraordinary) component.
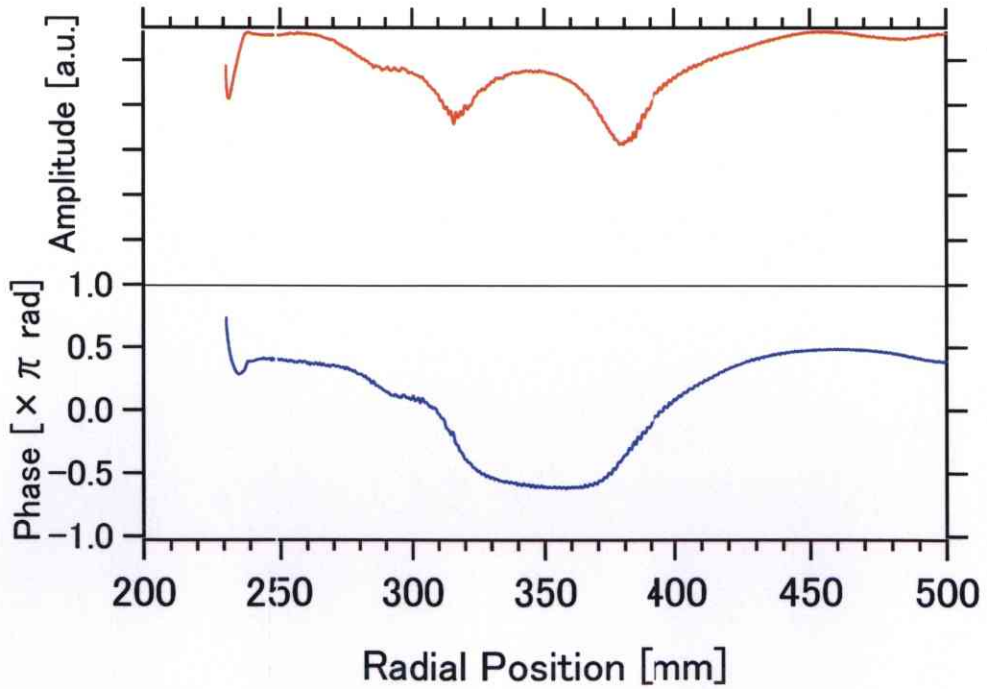
Figure 6.26: Red (Blue) corresponds to the amplitude (phase) profile.
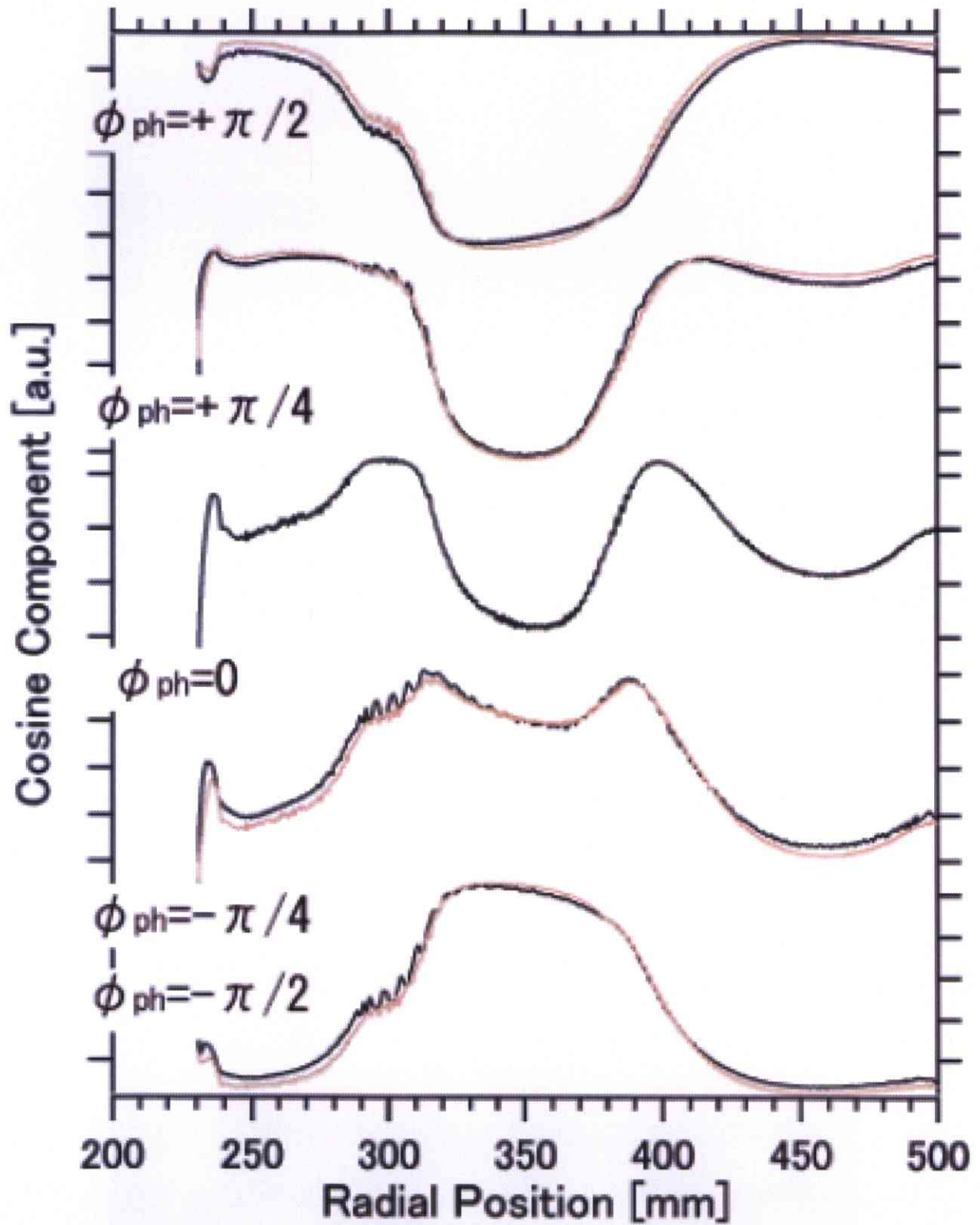
Figure 6.27: Black and red lines denote experimentally and numerically time-delayed data, respectively. Experimental time-delay means time-delay was given by phase shifter, whereas numerical time time-delay means adding phase into phase profile artificially and reconstruct cosine signal profile from amplitude and phase profiles (see Fig. 6.26). Results coincide each other.

Reproducibility of wave characteristics during scanning measurement of the probing antenna has been examined. Figure 6.28 shows a typical waveform of the electric field, where plasma is confined inside of the last closed flux surface located at R = 320 mm. Fluctuations on the ECRF electric fields measured by scanning the probing antenna can be seen in Fig. 6.28, and it is found that electric field fluctuation in the vacuum region (R>320 mm) seems to be relatively larger than that inside the plasma. To check the reproducibility of the ECRF electric field, we have measured the spatial profile of the ECRF electric field shot by shot, by holding the antennas at a radially-fixed position during one shot. In Fig. 6.28, the scatters of the signals of this shot-by-shot measurement are shown with vertical bars. Measurement over multiple shots at different radial positions are in good agreement with scanning measurements over a single shot.
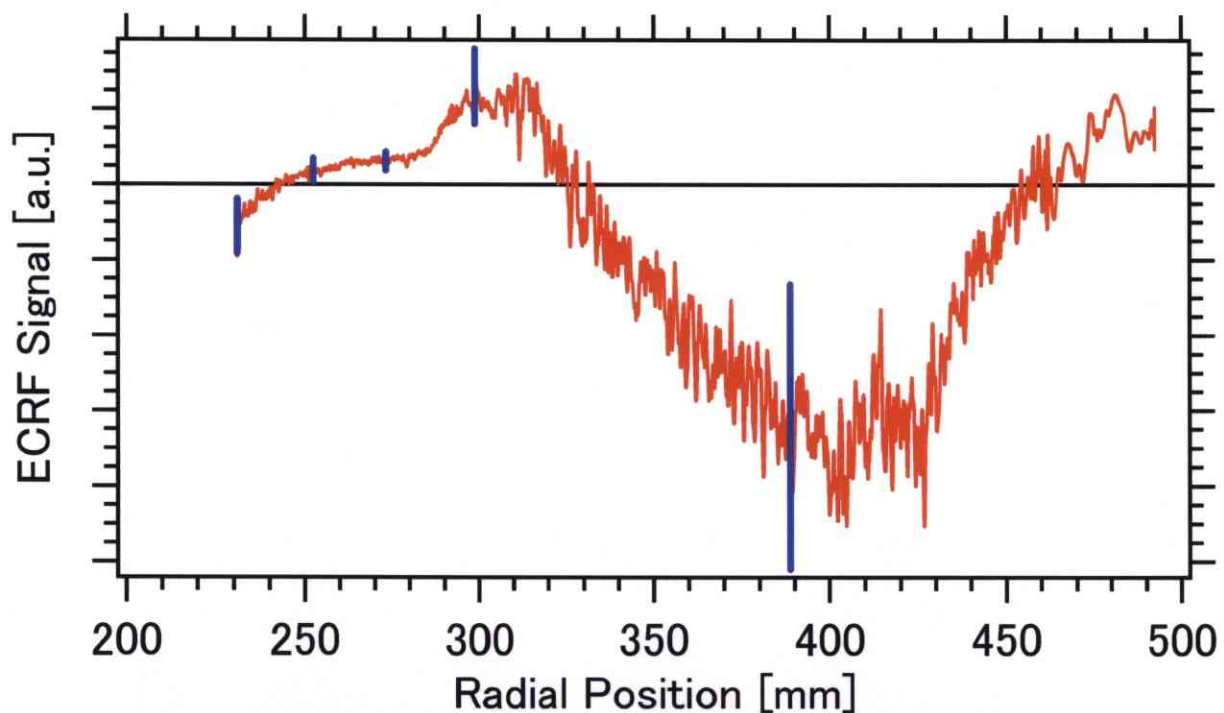
Figure 6.28: A solid line is a smoothed ECRF electric field profile of O-mode, and the dots show accuracy of signal in plasma.

Since an EBW has a group velocity of the order of an electron thermal velocity, it arrives at a probing antenna with a time delay from an electromagnetic wave. Figure 6.29 shows an example of signals of a 35 mm monopole antenna and a 1 mm small tip antenna. A pulse signal arrives at a monopole antenna at approximately the same time in a plasma, whereas it arrives at a small tip antenna, and the time delay depends on a location of a small tip antenna.

Therefore one can evaluate a group velocity of an electrostatic wave in a plasma. This is due to a difference between an electron thermal velocity and a light speed. Although a monopole antenna also breaks a symmetry between grounded and ungrounded sides of an elements, i.e. there is not an ungrounded one, it is sensitive to a signal owing to an electromagnetic wave. It seems that signals from both of an electromagnetic and an electrostatic wave reach at a monopole antenna. However a signal from an electromagnetic wave may be larger than that form an electrostatic wave due to a dimension of the antenna. On the other hand, it may be smaller when a small tip antenna is used.
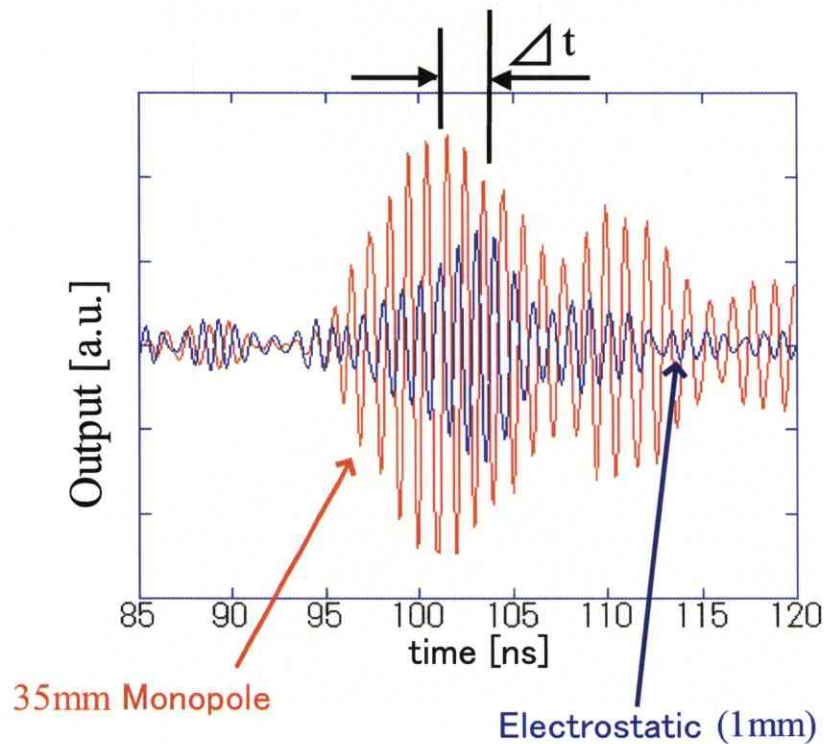
Figure 6.29: Time delay of a signal on a small tip antenna. By comprising the arrival time in several locations in a plasma, one can evaluate a group velocity of an electrostatic wave in a plasma.

Chapter 7

ECRF ELECTRIC FIELD PROPERTY IN MINI-RT

As described in Chap. 3, the EBW has several characteristics, i.e.

1. An EBW does not have the density limit.

2. An EBW has a long-wavelength at the UHR, i.e. an EBW is excited at the UHR from an electromagnetic wave.

3. The typical value of the wavelength of an EBW is of the order of an electron Larmor radius.

4. Polarization of an EBW is electrostatic (longitudinal).

5. EBW resonates with an electron gyro-motion at any harmonic ECR layers.

6. EBW has a negative group velocity, i.e. the direction of a group velocity is opposite to a phase velocity.

7. The phase velocity and the group velocity of an EBW is of the order of an electron thermal velocity.

7.1   Short-Wavelength Excitation

Since an EBW is excited around the UHR, electron density profile plays a crucial role to determine the location of excitation of an EBW. In Mini-RT, an electron density depends on

the heating power, the magnetic configuration (levitation coil current), a filling gas pressure and a working gas species. The location of the UHR is determined by an electron density and a magnetic field strength, so that the author investigated following cases. One is the configuration dependence, the other is the injection frequency dependence. ECRF electric field measurements were carried out in several density profiles to investigate a relationship between a location of the UHR and a short-wavelength region. Figure 7.1 shows an electron density profile and three components of an ECRF electric field. In this case, injection frequency of the diagnostic microwave is 1.0 GHz, and the height of the measurement position is 20 mm above the mid-plane. Two 35 mm monopole antennas and a 1 mm small tip antenna were used for this experiment. The location of the separatrix is $R = 303$ mm. The electrostatic component exhibits a relatively short-wavelength at which an electron density gradient is steep, whereas the transverse (electromagnetic) components do not show such a characteristic. The wavelength of this signal is around 20 mm, which is evaluated from the waveforms, i.e. the refractive index of this wave is 15. The location of the UHR can be evaluated from a vacuum magnetic field, i.e. $\beta = 0$, and a density profile that is obtained from a triple probe measurement. The location of the UHR is $R = 300$ mm, which approximately coincides with the location of a short-wavelength excitation. Figure 7.2 shows the various frequency, i.e. a plasma frequency, the absolute value of the electron cyclotron frequency, an upper hybrid frequency, a right hand frequency, a left hand frequency and an injection frequency. Figure 7.3 shows the expanding of it around the separatrix. The locations of the plasma cutoff (P-cutoff) and the left hand cutoff (L-cutoff), which correspond to the cutoff of O-wave and X-wave, are $R = 297$ mm and $R = 293$ mm, respectively. Therefore the short-wavelength signal mainly propagates in the evanescent region of the cold waves, moreover the amplitude of the longitudinal (electrostatic) component is relatively small outside of the separatrix. Figure 7.4 shows the amplitude profiles of each component of an ECRF electric field in Fig. 7.1. Note tat the scale of an electrostatic component is different from another ones, i.e. the toroidal and the poloidal components are shown in a same scale. However in the present circumstances, the absolute value of an amplitude cannot be obtained. The ordinary component is smaller than the extraordinary component, both of them decrease inside the evanescent region. The wall of vacuum vessel lies at $R = 500$ mm, where tangential components of an ECRF electric field go to zero.

As expected theoretically and shown experimentally above, the short-wavelength signal is observed around the separatrix (or the UHR), so that one can consider the excitation of a
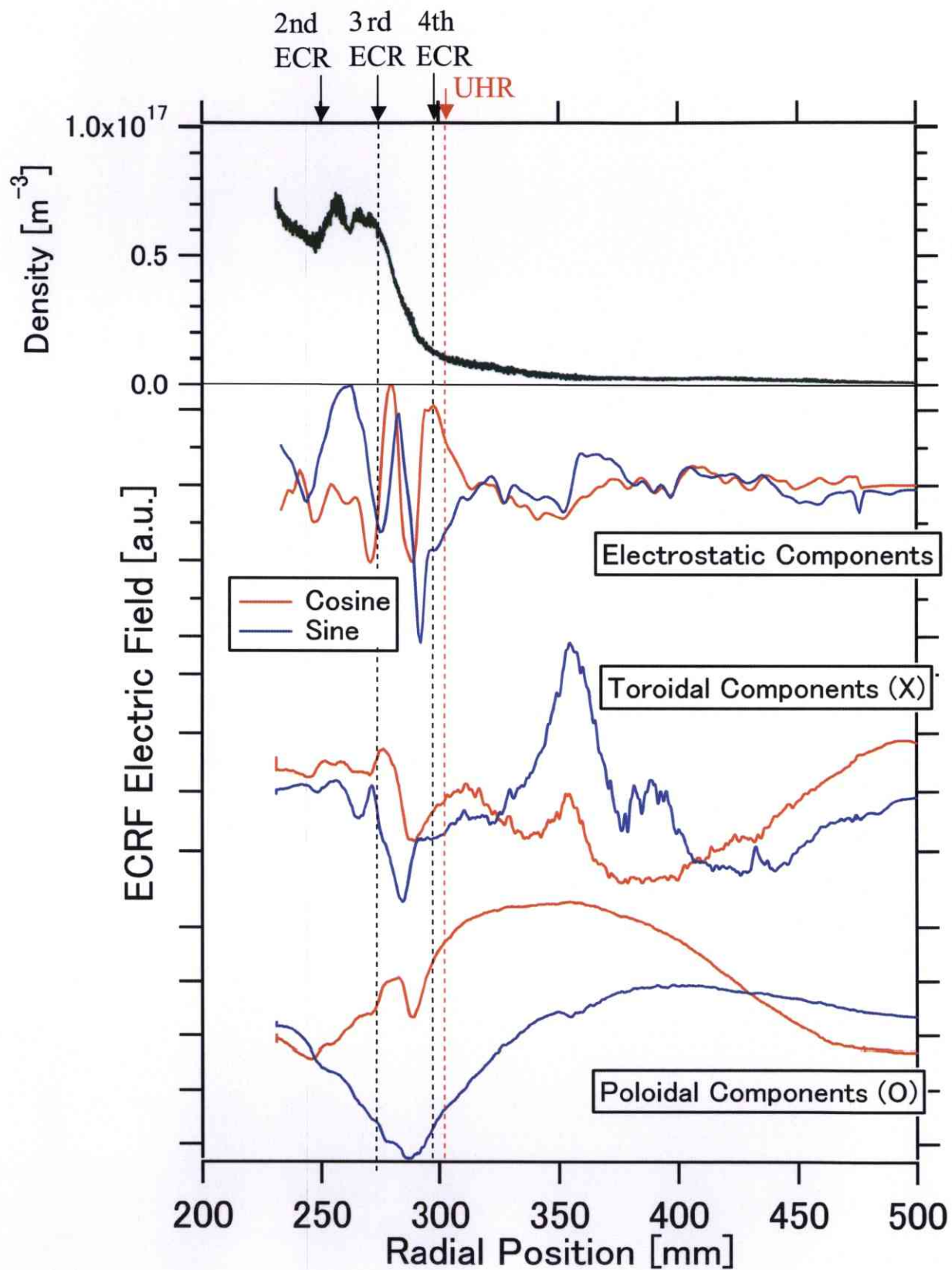
Figure 7.1: A result of an ECRF electric field measurement.
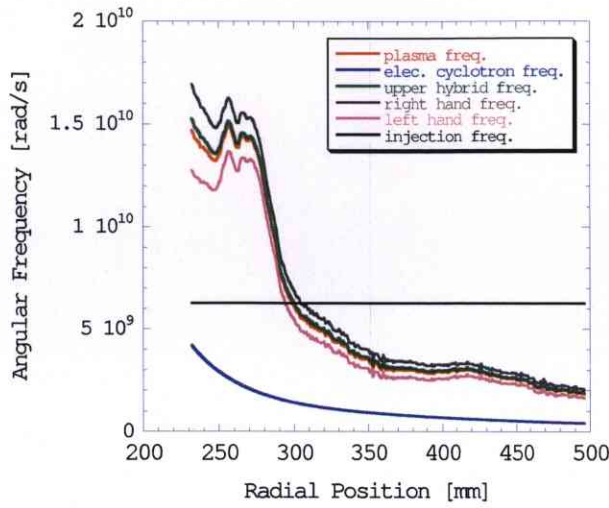
Figure 7.2: Spatial variation of several specific frequencies.
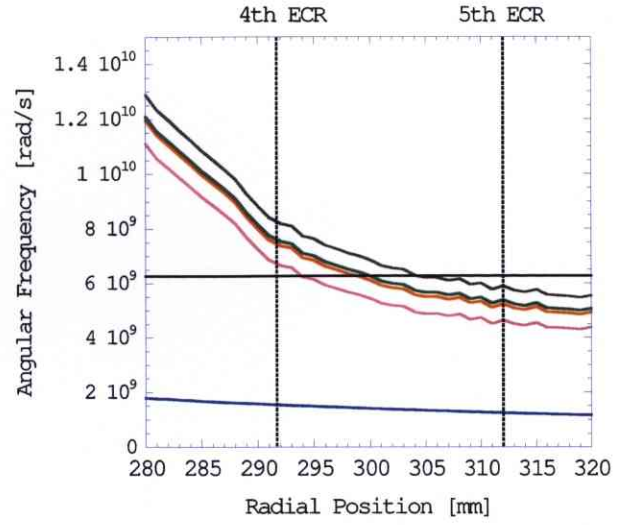
Figure 7.3: Expanding of Fig. 7.2 around the separatrix.
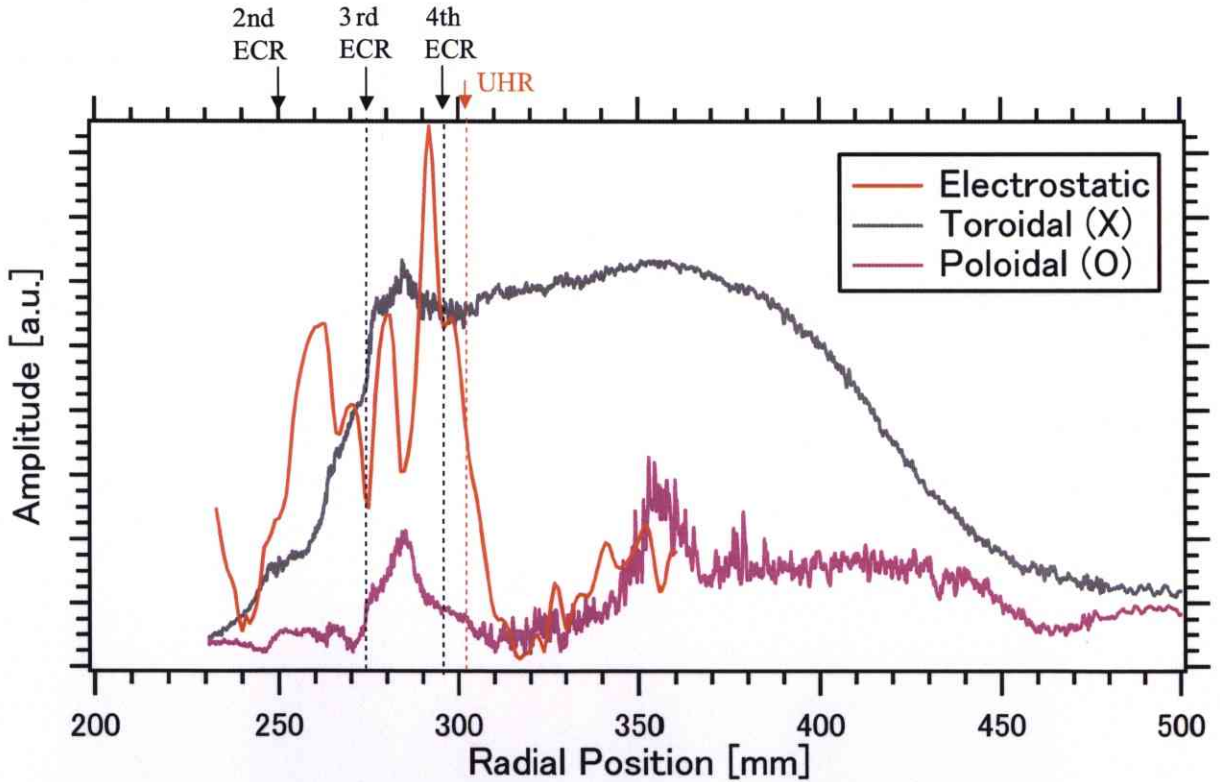
Figure 7.4: Profiles of an amplitude of each component of an ECRF electric field.

wave with an electrostatic component is dominated by a plasma shape. In the separatrix configuration, a plasma is not symmetric to the vertical direction. Thus one can expect that a profile of an ECRF electric field at a different vertical location differs from Fig. 7.1. Figure 7.5 shows the electrostatic component on different measurement paths, i.e. one is $z = +20$

mm which corresponds to Fig. 7.1 and the other is $z = -20$ mm. Similarly to Fig. 7.1, the short-wavelength (10 mm) signal is observed around the separatrix in this case. In addition the amplitude is quite small at outside a plasma. Thus one can realize a plasma having a steep density gradient affects the excitation of a short-wavelength wave. The reason why there is a difference of the harmonic ECR locations of $z = +20$ mm and $Z = -20$ mm cases is due to the vertical asymmetry of the magnetic field configuration. Since the levitation coil, which determines the location of the separatrix, is located above the vacuum vessel, influence by the levitation coil is more strong at $z = +20$ mm path.

Same behavior is observed when the electron density profiles are changed. When an electron density profile is spread, the location of excitation of the short-wavelength wave goes to outward of the device. In fact, the region where a short-wavelength wave is observed always locates around the UHR. Figure 7.6 shows profiles of an electrostatic component in several configurations. In this figure, each color of an electron density profile corresponds to the same color of an electrostatic component of an ECRF electric field profile. This property suggests the excitation of an electrostatic wave around the UHR, and wavelengths of them are of the order of 10 mm, which corresponds to a refractive index of $10 \sim 30$. Typical wavelength of an EBW in Mini-RT was calculated, and it predicts a refractive index of 100 to 200 around the harmonic ECR layers [84]. Experimental wavelength is approximately ten times greater than the calculated one. This discrepancy is discussed in Sec. 7.5.
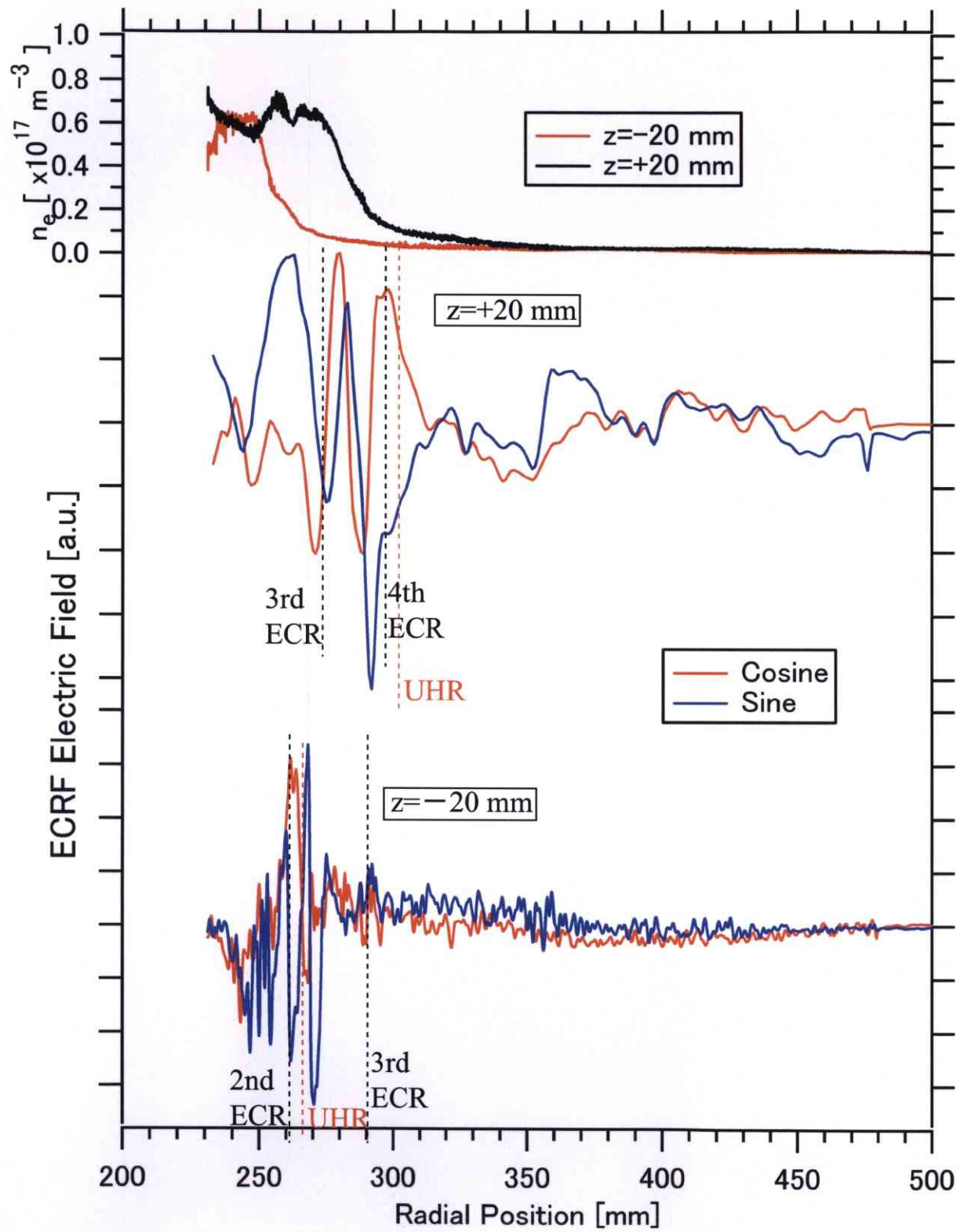
Figure 7.5: Comparison of profiles of an electrostatic component on the two different measurement paths.
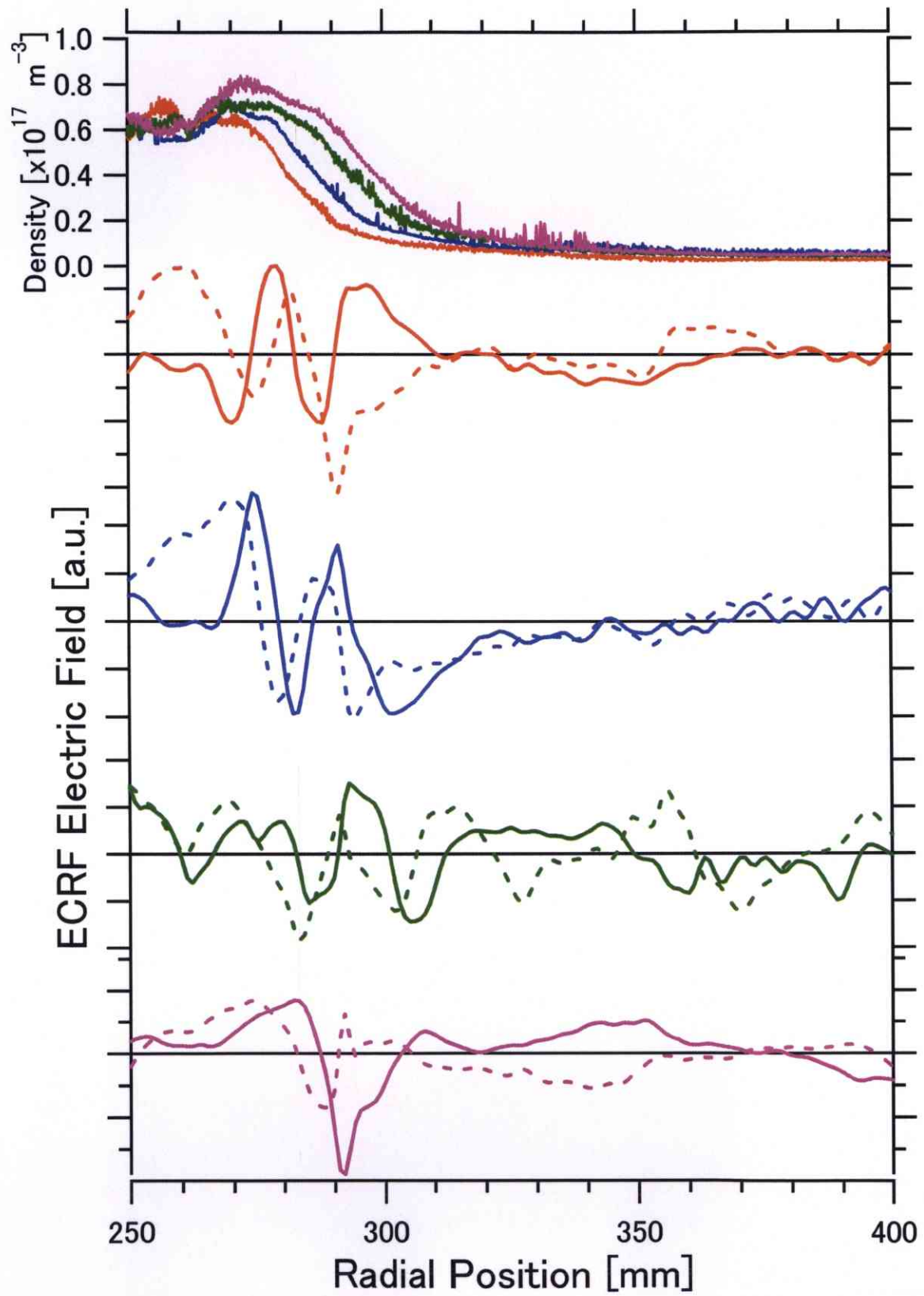
Figure 7.6: Comparison of electrostatic component results in several density profiles.

Since the electron Bernstein wave has a short-wavelength, it is absorbed sufficiently at the harmonic electron cyclotron resonance layer. For instance, in Fig. 7.1, the short-wavelength signal damps around $R = 270$ mm, which locates the 3rd harmonic ECR layer, i.e. $R = 275$ mm. In addition an EBW propagates locally, i.e. between the excited location, which corresponds to the UHR, and absorbed location, which corresponds to the 3rd harmonic ECR layer. Figure 7.5 also shows such a local propagation of short-wavelength wave, and it propagates in the evanescent regions of cold plasma waves. Similar results were obtained in many foregone experiments [83][84][85].

By changing an injection frequency of a diagnostic microwave, it is possible to change the location of the UHR without changing any condition of a discharge. Figure 7.7 shows the profiles of an electrostatic component of an ECRF electric field for various injection frequencies.

The location of a short-wavelength excitation moves inside the plasma with increasing of the injection frequency. Therefore this result also support the excitation of EBW around the UHR.

Although the quantitative verification is remained as a future work, excitation of EBW at the UHR is suggested qualitatively.
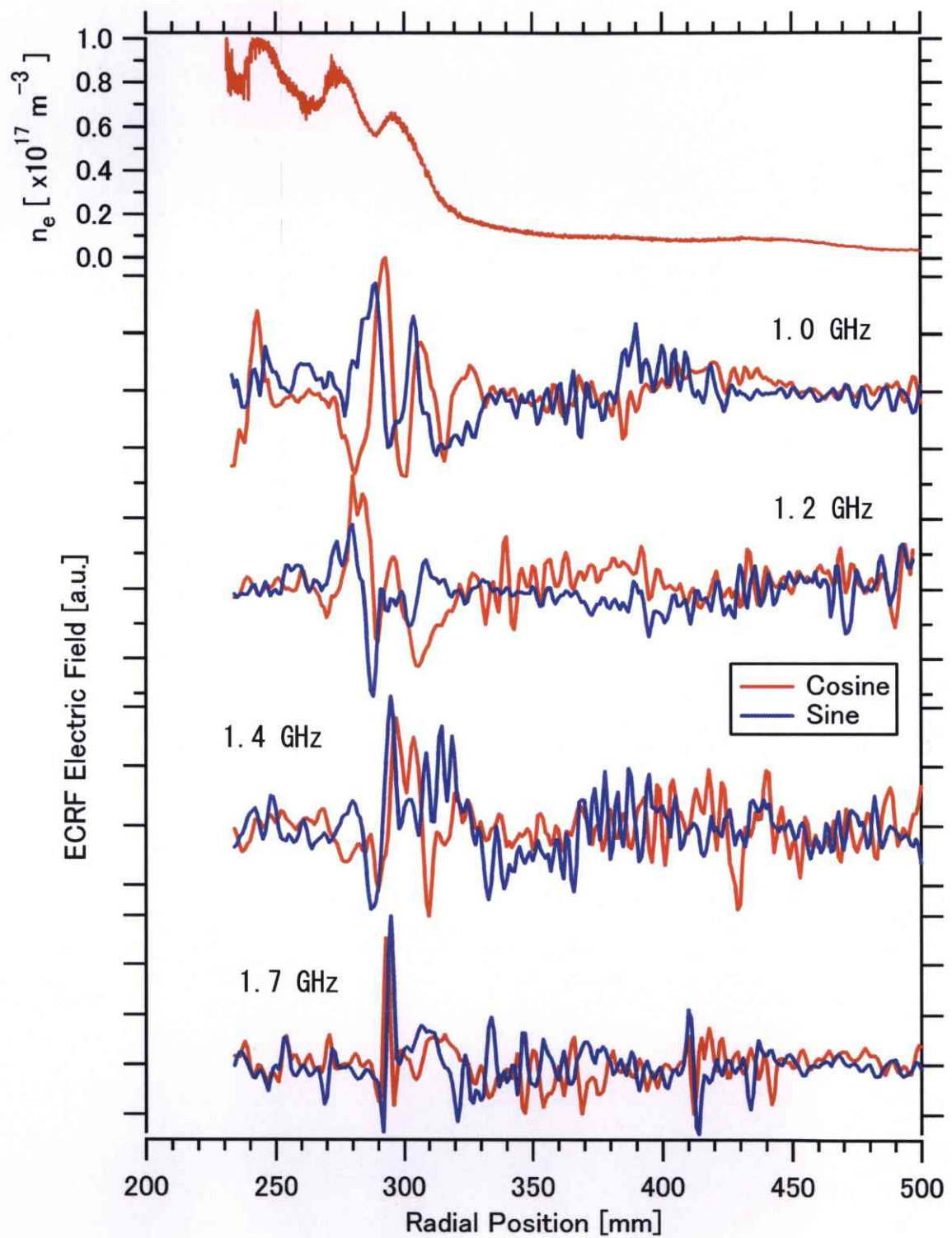
Figure 7.7: Comparison of electrostatic component results under several injection frequencies.

7.2 Phase Profile of ECRF electric Fields

As shown in Chap. 3, an EBW has a backward characteristic, i.e. a phase velocity directs opposite to a group velocity [71]. The phase is a function of spatial location and the lengths of a transmission line. Moreover, the gradient of the phase (gradient of the eikonal) gives the direction of phase velocity, i.e. if the gradient is positive, the phase velocity directs outward of the device.

Profiles of the phase of each component are shown in Fig. 7.8, and we have confirmed the phase reversal around the UHR. Similar experiments have been conducted for different frequencies, and the characteristic of the phase reversal has been observed in all cases for each frequency (see Fig. 7.9) [84]. Results also indicate that this phenomenon occurs on the high-field side of the cyclotron harmonic resonance layer of each frequency, and the location coincides with a short-wavelength region. It is well known that there are two extraordinary modes around the UHR, i.e., the slow X-wave and the EBW. A slow X-wave, which is all-(non-) reflective at the L-cutoff (UHR), would represent a characteristic of a standing wave, where a phase is constant between the nodes, whereas the experimentally observed phases (Fig. 7.9) change gradually around the UHR. This might indicate a propagating wave, such as a mode-converted EBW. Moreover, we consider the direction of group velocity, i.e., energy flux, which should be inward of the device. Since the EBW has characteristics of a backward wave with a short wavelength [13], experimental results shown in Figs. 7.8 and 7.9 suggest the direct measurement of the mode-converted EBW between cyclotron harmonic resonance surfaces.
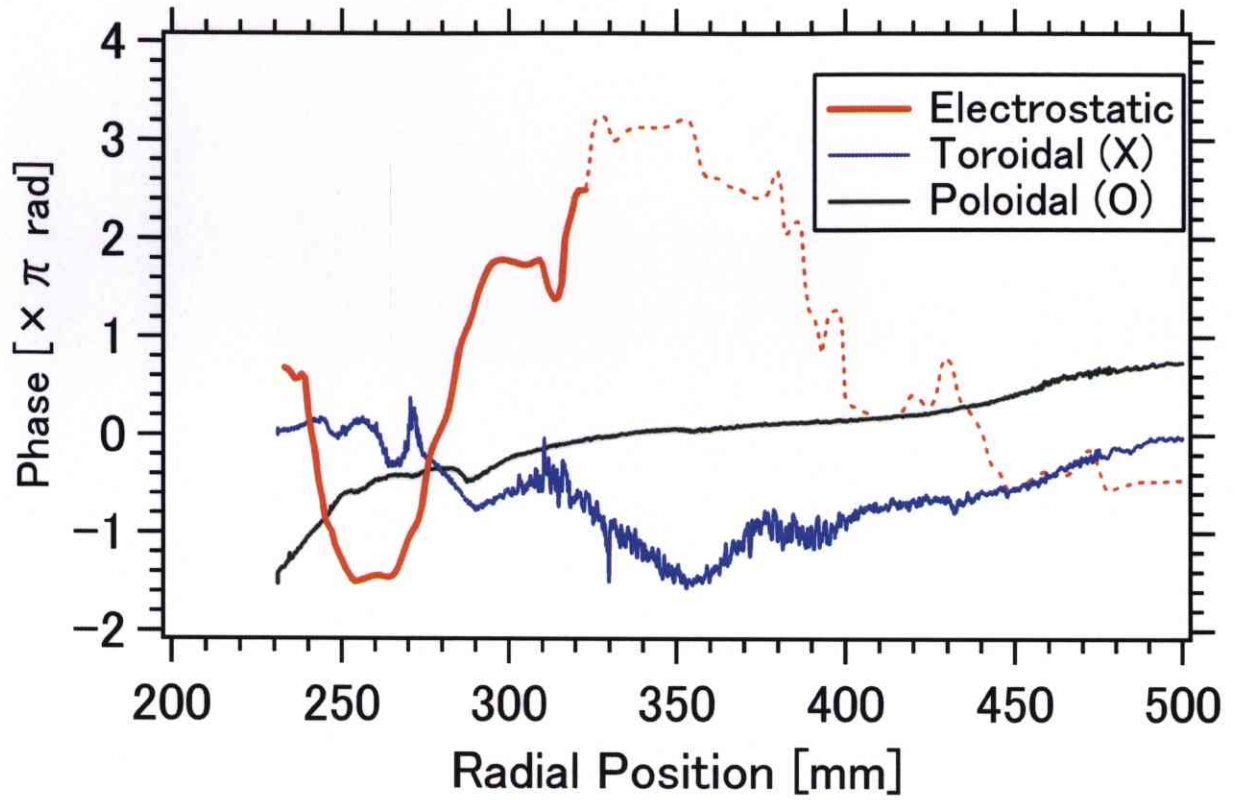
Figure 7.8: Phase profiles of each component of an ECRF electric field.
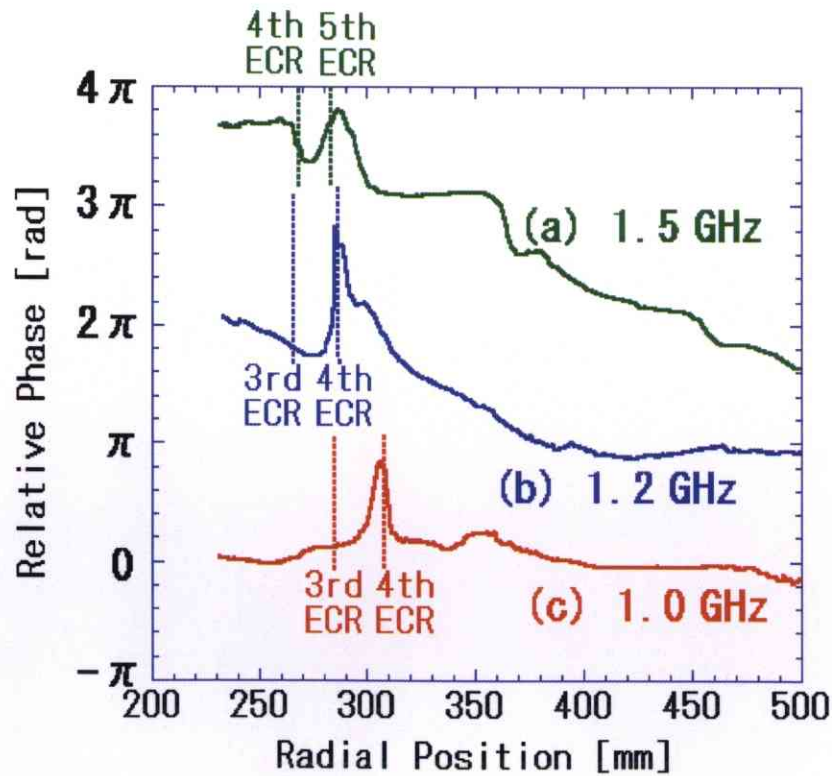
Figure 7.9: Phase profiles of electrostatic component of an ECRF electric field for various injection frequencies.

7.3 Simultaneous Measurements of ECRF Electric and Magnetic Fields

ECRF magnetic field measurements support that the detected short-wavelength wave is a mode-converted EBW from an electromagnetic wave. Figure 7.10 shows profiles of ECRF electric and magnetic fields. We used a square plate antenna for an electrostatic wave detection, two 40 mm dipole antennas for the electric field of an electromagnetic one and three loop antennas for the magnetic field measurement. Here x, y and z directions correspond to radial, toroidal and poloidal directions, respectively. In addition, y component of an electric field and z component of a magnetic field correspond to the X-wave. The amplitude of an X-wave decreases around at which the short-wavelength wave is excited. The observed wavelength of the short-wavelength wave is around 20 mm, which coincides with former results. Unfortunately, the location of the UHR could not obtained by a triple probe. It is expected that the UHR lies around at $R = 300$ mm. Moreover the short-wavelength wave is damped at the 2nd harmonic ECR layer. This result suggests an X-wave is mode-converted into an EBW around the UHR.

Profiles of a phase of Fig. 7.10 is shown in Fig. 7.11. It does not coincide with a notion, i.e. we injected an X-wave from outside of a plasma the phase velocity of it directs outward at outside a plasma. Moreover the phase velocity of a short-wavelength wave directs inward. Such a property was observed in former fundamental experiments in another device [23]. Figure 7.11 may show the inverse process of mode-conversion, i.e. the B-SX-FX conversion. However, at the current moment, detailed discussions have not be done sufficiently.
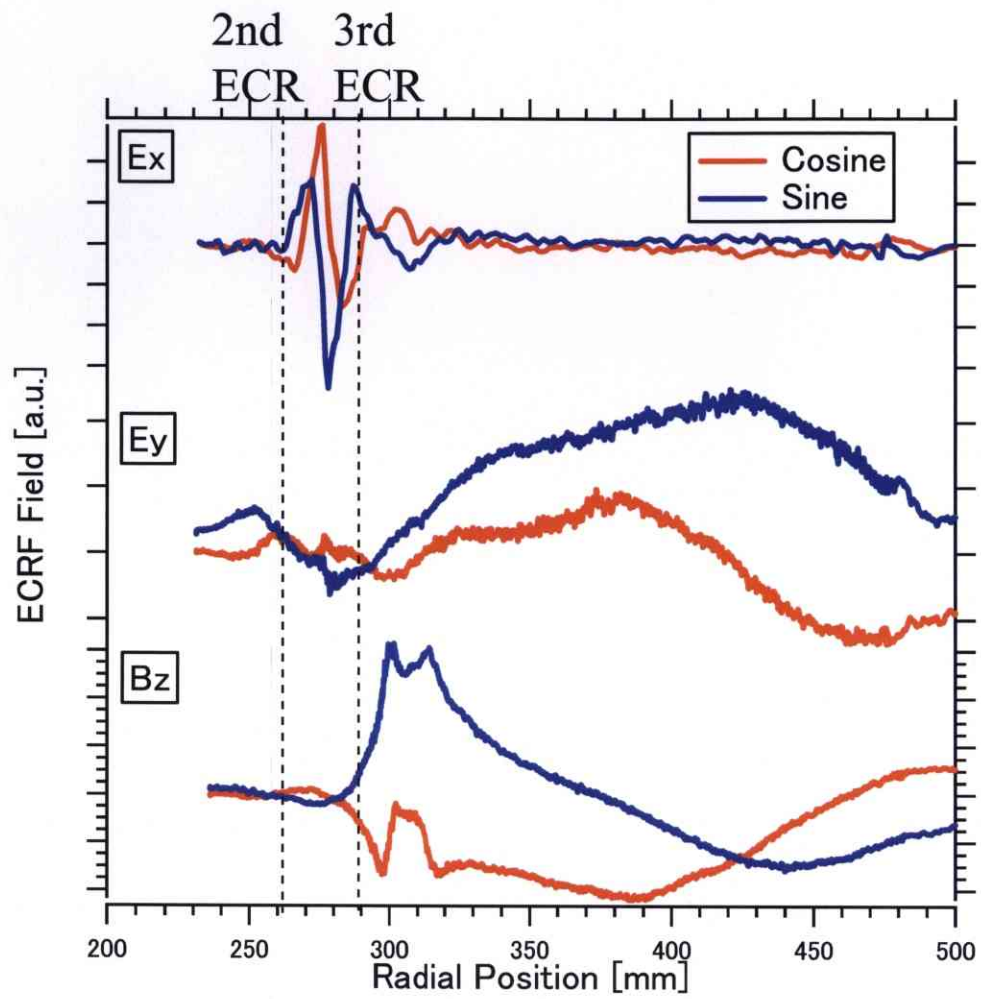
Figure 7.10: ECRF electric and magnetic fields. The x, y and z directions denote radial, toroidal and poloidal directions, respectively.
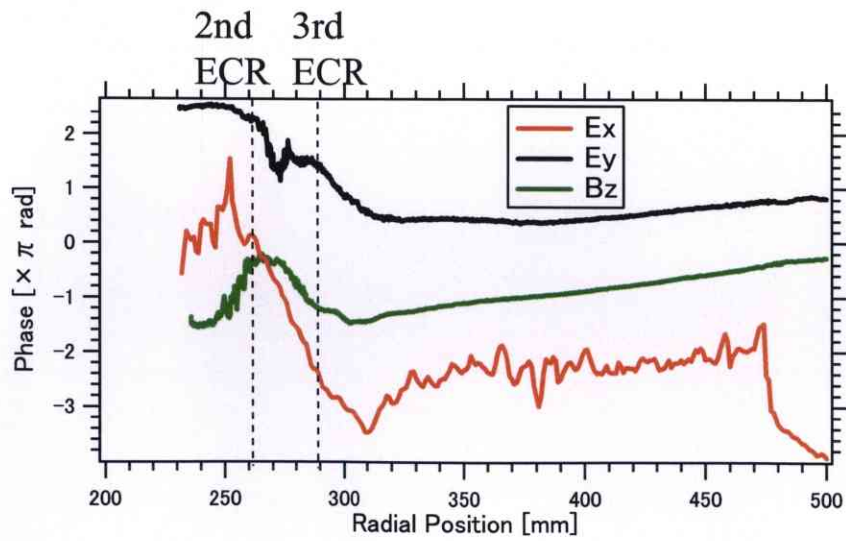
Figure 7.11: Profiles of a phase of Fig. 7.10.

120

7.4 Group Velocity Measurements

Figure 7.12 shows the preliminary results of a pulse injection experiment with a small tip antenna [31]. The arrival time of a pulse depends on the measurement point. It tend to be later as the location of the antenna lies inward. Therefore the direction of the group velocity is inward direction. Since this measurement was not carried out simultaneously with a steady injection experiment, one cannot conclude whether this wave is a backward wave or not. However, the direction of the phase velocity is outward in a number of experiments. Thus it is feasible to think that a detected time delay is due to such a wave which has the outward phase velocity. The locations which can be observed the time delay approximately coincides the short-wavelength region.

Figure 7.13: Spacial dependence of the time delay, i.e. the arrival time, of the signal.
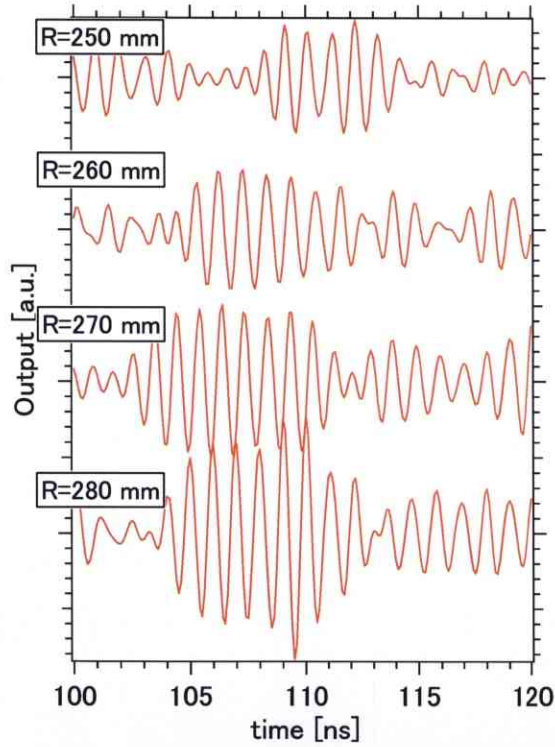
Figure 7.12: A typical result of the arrival time of the signal.

By comparing the arrival time, one can evaluate the group velocity of this wave. Figure 7.13 shows the spacial dependence of the arrival time in a plasma. Around the plasma edge, the arrival time is spatially independent within the margin of error, whereas there is significant difference for $R = 270$ mm. From the gradient of this figure, one can evaluate the group velocity is approximately 5×10^6 m/s, which corresponds to an electron thermal velocity of 50

eV electron. As mentioned in Chap. 3, an EBW has a group velocity of the order of an electron thermal velocity. In addition Chap. 5 shows a typical value of an electron temperature, i.e. mean energy of electrons, is 10 eV. Therefore this experiment also supports the excitation of an EBW around the UHR, of coarse this model cannot explain completely the experimental results. Note the light speed is approximately 100 times larger than the group velocity of the detected wave. If the electron thermal speed doubles, the energy, i.e. temperature quadruples.

7.5 Consideration of the Discrepancy of a Wavelength Between an Experiment and a Theory

Although observed signals have most of characteristics of an EBW, i.e. propagates in the evanescent region, damps at the cyclotron harmonic layer, be excited around the UHR, has a short-wavelength, an electrostatic wave and a backward wave, there were quantitatively discrepancies between observation and theoretical values. Since an EBW has wavelength of the order of the electron Larmor radius, electron temperature is one of the most important parameters for determining a wavelength of it. Moreover, as derived in Chap. 3, finite Larmor radius effect is effective when the wavelength is comparable with the electron Larmor radius. Therefore it is expected that a wave energy is coupled with relatively high energy electrons.

As well known, the ECH enables one to produce high energy electrons due to the quasi-linear diffusion of resonant electrons [29]. In Mini-RT, a plasma is produced by the ECH, thus we have prospects of production of high energy electrons. We estimate the effective temperature of high energy electron is 5 keV by using the scaling law of Ref. [76].

$$\rho/L = 5 - 6 \times 10^{-2}, \tag{7.1}$$

where ρ and L are a high energy electron Larmor radius and a magnetic scale length, respectively. We have estimated $L \sim 4$ cm and the magnetic field strength B equals to 0.0875 T. We assumed an electron distribution function has two components isotropic Maxwellian, i.e. summation of bulk electrons (10 eV) and high energy electrons (5 keV), for simplicity. We calculated for four cases, i.e. (a) no high energy electrons, (b) 10% of them exist, (c) 30% of them exist and (d) hot electrons. We also assumed the internal coil current $I_F = 30$ kA and the levitation coil current $I_L = 15$ kA, which corresponds to a typical magnetic configuration in Mini-RT. In this configuration, the mode-conversion occurs between 3rd and 4th harmonic

ECR layers. The dispersion relation of hot waves propagating perpendicular to the magnetic field is written as

$$K_{xx}(K_{yy} - N^2) - K_{xy}K_{yx} = 0, \tag{7.2}$$

where N and $\overleftrightarrow{K}$ are a refractive index and a specific dielectric tensor of a hot wave, respectively. And each component of $\overleftrightarrow{K}$ is defined in Eqs. (A.167), (A.177)-(A.179). High energy electrons affect the dispersion relation of a hot wave especially around the UHR. If there is no high energy electron, i.e. under the case of (a), the refractive index dramatically rises around the UHR. Refractive indices have relatively a long wavelength region (refractive index is small) when the fraction of high energy electrons is increased. The reason why the refractive indices, for (b) and (c), are so complex is due to assumption of two components Maxwellian distribution function. The finite Larmor radius (FLR) effect from high-energy electrons around the UHR causes the propagation with a long wavelength. On the other hand, the refractive indices show identical characteristics around the 3rd harmonic ECR, for the case with (a), (b) and (c) of Fig. 7.16. Around the resonance region, a wavelength is comparable to an electron Larmor radius, therefore sufficient FLR effect from bulk electrons can be expected.
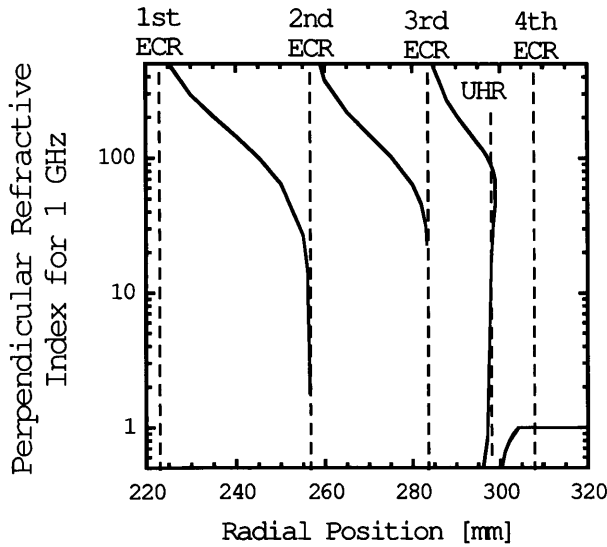
Figure 7.14: Radial profile of perpendicular refractive indices for 1 GHz of hot waves on typical profiles of density and magnetic field.
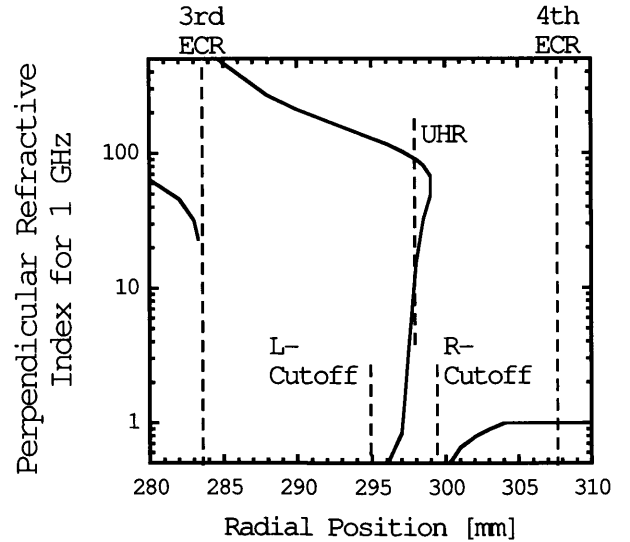
Figure 7.15: Expanding of Fig. 7.14 around the UHR.

Temperature of the high energy electrons only affects the wavelength of a hot plasma wave. Figure 7.17 shows the variation of wavelength with respect to the temperature of high energy electrons. One can see that temperature affects only the wavelength, i.e. not affect to the

width of the middle-wavelength region, at where the wavelength is between EBW's and cold X-mode's values. Experiments shows middle wavelength not only around the UHR but also around the harmonic ECR layer.
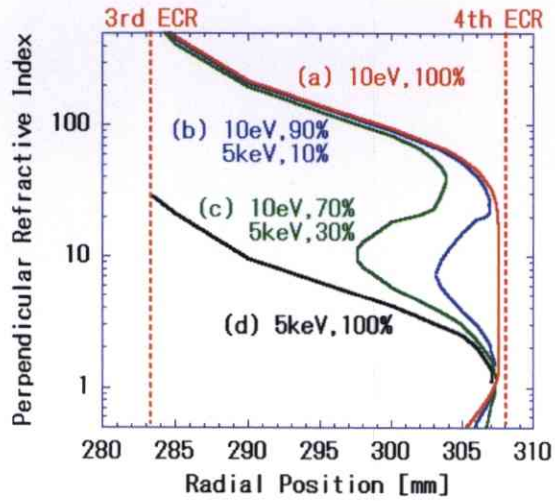
Figure 7.16: Radial profile of perpendicular refractive indices, for 1 GHz, of hot waves with (a) all electrons has temperature of 10 eV, (b ,c ,d) 10, 30, 100 percents high-energy electrons has that of 5 keV. Dotted lines denote the location of harmonic ECR on mid-plane.
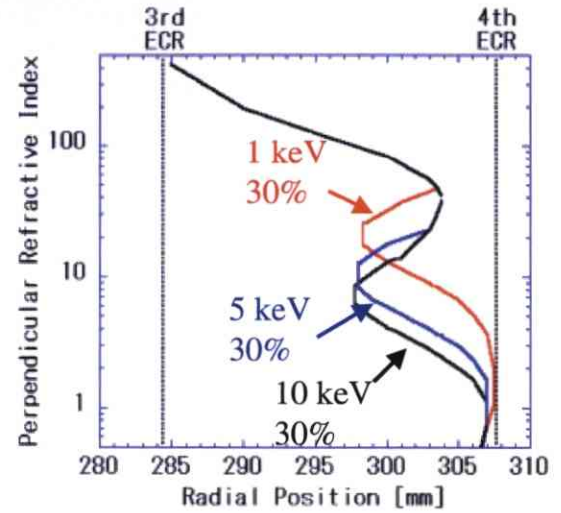
Figure 7.17: Temperature of high energy electrons affects only to the wavelength.

Chapter 8

Conclusion

8.1 Summary of this Research

This work is concerned with the dipole plasma confinement, which is carried out in the Mini-RT device. Researchers who works on dipole devices are oriented to the high beta, i.e. high ratio of plasma pressure to the magnetic field, plasma confinement by the nature's way, e.g. like the Jovian magnetosphere. In order to produce and sustain such a plasma, an advanced auxiliary heating method plays a crucial role. As well known a conventional electron heating by rf-waves have difficulties due to the cutoff by a plasma. The electron Bernstein wave (EBW) heating is one of the most promising methods for the high beta plasma heating because it can propagate without a density limit and effectively absorbed at any harmonic electron cyclotron resonance layer. This wave is studied in many spherical tori, which is oriented to the high beta plasma heating and non-inductive sustainment, or sterallators, which can achieve super-dense discharges.

Overdense plasmas were observed in Mini-RT when the internal coil was magnetically levitated. In order to investigate the mechanism of such a high density plasma only with an rf-heating, the heating properties were investigated from the profiles of an electron density and electron temperature. Moreover directly electron cyclotron range of frequency (ECRF) electric and magnetic field measurements by inserting antennas into plasma were carried out. The author showed experimentally an EBW heating is quite favorable method of producing and sustaining an overdense plasma in Mini-RT, which is a dipole confinement device and oriented to producing a high beta plasma.

As mentioned in Chapter 1, in order to enhance a plasma performance on a magnetic

fusion, one should produce high beta plasmas. The EBW heating seems to be most promising method, and it is investigated experimentally and theoretically. In 1960s and 1970s, many fundamental experiments of waves in plasmas were carried out, and the existence of EBWs were verified experimentally in linear devices. On the other hand, from electron cyclotron emission measurements, mode-conversion from an electromagnetic wave into an EBW was investigated in many torus devices.

In Chapter 2, the concept of a high beta plasma confinement with a dipole device and the overall of the Mini-RT device are described. Self-organization of a flowing plasma enables one to confine a high beta, i.e. of the order of unity, plasma confinement. Driving of Alfvénic flow is necessary to achieve this concept. This is a candidate mechanism of extremely high beta plasma confinement in the Jovian magnetosphere. Mini-RT is a dipole device having an internal coil, which produces a magnetic field like a planet. The internal coil is made from a high temperature superconducting coil to avoid the energy loss of a plasma due to mechanical support structures of it.

Chapter 3 mentions theoretical basis of waves in plasmas with electron cyclotron range of frequency. Since an EBW has a wavelength of the order of an electron Larmor radius, it cannot be excited outside the plasma. One should excite it in a plasma through the mode-conversion process. In order to achieve it, one should reach an extraordinary wave (X-wave) to the upper hybrid resonance (UHR) layer with overcoming the evanescent region. In Mini-RT X-wave injection from the low field side is most promising way because it has a steep density gradient around the separatrix.

In chapter 4, the basic diagnostic tools in Mini-RT were referred. We obtain the profiles of an electron density and electron temperature by a triple probe. In addition, the integrated electron density is measured by a transmitting interferometer.

Chapter 5 shows the heating property of plasmas in Mini-RT. By applying a current to the levitation coil, one can change a location of the separatrix without touching to a plasma. From experiments with the supported internal coil, density transition was observed when the heating power exceeds a threshold value. It depends on a size of the plasma confinement region. Such a transition has been observed in many other devices, e.g. low confinement (L) and high confinement (H) mode transition in tokamaks. However, even if a plasma shows good confinement property, the peak value of an electron density is approximately up to the cutoff density of an O-mode of 2.45 GHz. On the other hand, more improvement of the

plasma performance was experimentally verified when the internal coil was levitated. One can produce a plasma with relatively low filling gas pressure of 10^{-3} Pa. It suggests the decrease of energy loss from mechanical structures. Moreover overdense plasmas were produced in such condition. This suggests the heating mechanism without density limit.

In chapter 6, the electron cyclotron range of frequency (ECRF) electric and magnetic field measurement system is described. There are two kind of operations, i.e. a steady injection and a pulse injection. In the steady injection experiments, interferometry is adopted to obtain snap-shots of ECRF electric and magnetic field. The frequency and the power of a diagnostic microwave are 1-2.1 GHz and 10 W, respectively. By using a separate frequency form the heating microwave, i.e. 2.45 GHz, one can obtain waves in overdense plasmas and low density plasmas with the same discharge condition. This system has 3 channels, so that each component of an ECRF electric or magnetic field can be obtained simultaneously. In the pulse injection experiments, the time of arrival of a wave in an antenna is measured. By comprising the time delay signal at several locations in a plasma, one can obtain a group velocity of this wave.

Chapter 7 shows experimental results of ECRF electric and magnetic field measurements. Relatively short-wavelength wave is detected when a plasma has a steep density gradient around the separatrix. This wave propagates in the evanescent region of cold waves, and the polarization of it is electrostatic (longitudinal). In addition, this wave excites around the UHR and dumps around the harmonic electron cyclotron resonance layer. Moreover the phase reversal is observed at which the short-wavelength wave is detected. If we assume that the group velocity of this wave is inward of the device, this suggests the negative group velocity characteristic. Pulse injection measurements directly verify that the group velocity is inward to the device; however, the phase reversal and inward group velocity have not identified from same experimental condition. These characteristics coincide with the characteristics of an EBW qualitatively. However the experimentally obtained wavelength is approximately 10 times longer than the theoretically obtained one. The existence of high energy electrons has possibility of increasing of a wavelength, but if we want to explain the discrepancy of the wavelength only by high energy electrons, quite high fraction, i.e. several ten %, is needed. This is one of the open questions.

8.2 Future Visions and Issues

There still be mainly two open questions, i.e. one is the quantitative discussion of a wavelength and the other is mode-conversion efficiency.

In order to investigate the former one, the parallel component of the wavenumber may need to be considered. In this work the discussions about a wavelength were carried out by neglecting the parallel component of a wavenumber since an EBW is an electrostatic wave propagating perpendicular to the magnetic field. One possibility of the experimental investigation method of it is phasing of the excitation antennas by phase shifters. Or one can change the direction of the propagation by using a waveguide for the injection and controlling the frequency of a diagnostic microwave. In addition, the parallel component of a wavenumber plays an important role for absorption, and it can be generated by the reflection at the vacuum vessel wall.

The latter one is crucial for applying the EBW heating and current drive to larger device, e.g. RT-1. The establishment of the Poynting vector measurement is quite a promising principle because one can evaluate the energy flux and its reflection only from the electromagnetic mode, i.e. it may be possible to evaluate the mode-conversion efficiency at outside the plasma directly. The calibration of relative phases of different channels is necessary to achieve it. One should carefully evaluate not only the length of a transmission line but also the inductance and the capacitance of each component of the diagnostic system, e.g. an antenna element, a band pass filter, a mixer and so on.

Bibliography

[1] "ITER Physics Basis", Nucl. Fus. **39**, 2137 (1999).

[2] "Progress in the ITER Physics Basis", Nucl. Fus. **47**, S1 (2007).

[3] M. Abramowitz, *et al.*, "Handbook of Mathematical Functions", Dover (1970).

[4] W. R. Arnold *et al.*, "Cross Sections for the Reactions $D(d,p)T$, $D(d,n)He^3$, $T(d,n)He^4$, and $He^3(d,p)He^4$ below 120 keV", Phys. Rev. **93**, 483 (1954).

[5] P. J. Barrett *et al.*, "Dispersion of Electron Plasma Waves", Plasma Phys. **10**, 911 (1968).

[6] J. G. Bak *et al.*, "Fast reciprocating probe assembly for the Hanbit magnetic mirror device", Rev. Sci. Instr. **71**, 2071 (2000).

[7] I. B. Bernstein, "Waves in a Plasma in a Magnetic Field", Phys. Rev. **109**, 10 (1958).

[8] M. Bornatici, "Electron Cyclotron Emission and Absorption in Fusion Plasmas", Nucl. Fus. **23**, 1153 (1983).

[9] M. Brambilla, "Slow-wave Launching at the Lower Hybrid Frequency Using a Phased Waveguide Array", Nucl. Fus. **16**, 1 (1976).

[10] K. G. Budden, *Radio Waves in the Ionosphere*, Cambridge Univ. Press, London (1961).

[11] S. L. Chen *et al.*, "Instantaneous Direct-Display System of Plasma Parameters by Means of Triple Probe", J. Appl. Phys. **36**, 2363 (1965).

[12] S. A. Colgate *et al.*, "Stabilization of Pinch Discharge", Phys. Fluids **3** 982 (1960).

[13] F.W. Crawford *et al.*, "On the Interpretation of Ionospheric Resonances Stimulated by Alouette 1", J. Geophys. Res., **72**, 57 (1967).

[14] H. Derfler *et al.*, "Cyclotron Harmonic Waves in an Inhomogeneous Plasma-I. Theory", Plasma Phys. **14**, 473 (1972).

[15] S. J. Diem *et al.*, "Investigation of Electron Bernstein Wave (EBW) Coupling and its Critical Dependence on EBW Collisional Loss in High-β, H-Mode ST Plasmas", In *22nd IAEA Fusion Energy Conference*, EX/P6-17 (2008).

[16] P. C. Efthimion *et al.*, "New electron cyclotron emission diagnostics for measurement of temperature based upon the electron Bernstein wave", Rev. Sci. Instr. **70**, 1018 (1999).

[17] B. D. Fried and S. D. Conte, *The Plasma Dispersion Function*, Academic Press, New York (1961).

[18] R. W. Fredricks, "Structure of generalized ion Bernstein modes from the full electromagnetic dispersion relation", J. Plasma Phys. **2**, 365 (1968).

[19] D. T. Garnier *et al.*, "Design and initial operation of the LDX facility", Fus. Eng. Design **81**, 2371 (2006).

[20] J. A. Goetz *et al.*, "Lower Hybrid and Electron Bernstein Wave Current Drive Experiments in MST", In *22nd IAEA Fusion Energy Conference*, EX/P6-19 (2008).

[21] R. J. Goldston and P. H. Rutherford, *Introduction to Plasma Physics*, Institute of Physics Publishing, London (1995).

[22] T. Goto *et al.*, "Plasma Production by Electron Cyclotron Heating on the Internal Coil Device Mini-RT", Jpn. J. Appl. Phys. **45**, 5197 (2006).

[23] S. Gruber *et al.*, "Excitation of Longitudinal Waves near Electron-Cyclotron Harmonics", Phys. Fluids **11**, 122 (1968).

[24] I. H. Hatchinson, *Principles of Plasma Diagnostics*, Cambridge Univ. Press, London (2002).

[25] A. Hasegawa *et al.*, "AD $-^3$He Fusion Reactor Based on a Dipole Magnetic Field", Nucl. Fus. **30**, 2405 (1990).

[26] H. Igami *et al.*, "Electron Bernstein Wave Heating via the Slow X-B Mode Conversion Process with Direct Launching from the High Field Side in LHD", In *22nd IAEA Fusion Energy Conference*, EX/P6-13 (2008).

[27] B. Jones *et al.*, "Controlled Optimization of Mode Conversion from Electron Bernstein Waves to Extraordinary Mode in Magnetized Plasma", Phys. Rev. Lett. **90**, 165001 (2003).

[28] H. Kato, "Development of the Winding of a YBCO Coil and Progresses of the Magnetic Levitation of a Superconducting Coil" (in Japanese), Master Thesis, The University of Tokyo (2007).

[29] C. F. Kennel *et al.*, "Velocity Space Diffusion from Weak Plasma Turbulence in a Magnetic Field", Phys. Fluids **9**, 2377 (1966).

[30] L. J. Kieffer *et al.*, "Electron Impact Ionization Cross-Section Data for Atoms, Atomic Ions, and Diatomic Molecules: I. Experimental Data", Rev. Mod. Phys. **38**, 1 (1966).

[31] K. Kinjo, "Measurement of the Group Velocity on Electron Bernstein Wave by using Ultra-short Pulse Electromagnetic Wave" (in Japanese), Master Thesis, The University of Tokyo (2009).

[32] J. Kesner *et al.*, "Helium Catalyzed D-D Fusion in a Levitated Dipole", Nucl. Fus. **44**, 193 (2004).

[33] S. Konishi, "Use of Fusion Energy as a Heat for Various Applications", Fus. Eng. Design **58-59**, 1103 (2001).

[34] S. M. Krimigis *et al.*, "Hot Plasma Environment at Jupiter: Voyager 2 Results", Science **206**, 977 (1979).

[35] H. P. Laqua *et al.*, "Resonant and Non-resonant Electron Cyclotron Heating at Densities above the Plasma Cutoff by O-X-B Mode Conversion at the W7-As Stellarator", Phys. Rev. Lett. **78**, 3467 (1997).

[36] H. P. Laqua, "Electron Bernstein wave heating and diagnostic", Plasma Phys. Control Fus. **49**, R1 (2007).

[37] H. P. Laqua *et al.*, "Fundamental Investigation of Electron Bernstein Wave Heating and Current Drive at the WEGA Stellarator", In *22nd IAEA Fusion Energy Conference*, EX/P6-18 (2008).

[38] J. D. Lawson, "Some Criteria for a Power Producing Thermonuclear Reactor", Proc. Phys. Soc. (London) **B70**, 6 (1957).

[39] F. Leuterer, "Forward and Backward Bernstein Waves", Plasma Phys. **11**, 615 (1969).

[40] F. Leuterer, "Cyclotron Harmonic Waves in an Inhomogeneous Plasma-II. Experiment", Plasma Phys. **14**, 499 (1972).

[41] S. M. Mahajan *et al.*, "Double Curl Beltrami Flow: Diamagnetic Structures", Phys. Rev. Lett. **81**, 4863 (1998).

[42] O. Mitarai *et al.*, "Plasma Current Start-up by ECW and Vertical Field in the TST-2 Spherical Tokamak", J. Plasma Fus. Res. **80**, 549 (2004).

[43] T. Mito *et al.*, "Design and Construction of a Mini-RT Device" (in Japanese), J. Cryo. Soc. Jpn. **39**, 182 (2004).

[44] K. Miyamoto, "Plasma Physics and Controlled Nuclear Fusion" chapter 10 (in Japanese), University of Tokyo Press (2004).

[45] D. Montgomery *et al.*, "Three-dimensional magnetohydrodynamic turbulence in cylindrical geometry", Phys. Fluids **21**, 757 (1978).

[46] J. Morikawa *et al.*, "Levitation Experiment Using a High-Temperature Superconductor Coil for a Plasma Confinement Device", Jpn. J. Appl. Phys. **40**, L1029 (2001).

[47] J. Morikawa *et al.*, "Plasma Production and Levitation Experiments of a High-temperature Superconductor Coil in a Mini-RT Internal Coil Device" (in Japanese), J. Cryo. Soc. Jpn. **39**, 209 (2004).

[48] H. M. Mott-Smith *et al.*, "The Theory of Collectors in Gaseous Discharges", Phys. Rev. **28**, 727 (1926).

[49] C. Nakashima *et al.*, "Injection of electron beam into a toroidal trap using chaotic orbits near magnetic null", Phys. Rev. E **65**, 036409 (2002).

[50] Y. Ogawa *et al.*, "Construction and Operation of an Internal Coil Device with a High Temperature Superconductor", J. Plasma Fusion Res. **79** 643 (2003).

[51] Y. Ogawa *et al.*, "System Design of a Magnetically Levitated Internal Coil Device Mini-RT" (in Japanese), J. Cryo. Soc. Jpn. **39**, 175 (2004).

[52] T. Ohkawa *et al.*, "Stable Plasma Confinement by Multipole Fields", Phys. Lev. Lett. **7** 41 (1961).

[53] K. Ohkubo *et al.*, "Current Drive by Fast Magnetosonic Waves near the Lower Hybrid Frequency in the JIPP T-IIU Tokamak", Phys. Rev. Lett. **56**, 2040 (1986).

[54] M. Ono *et al.*, "Externally Launched Ion Bernstein Wave in the ACT-1 Toroidal Device", Phys. Rev. Lett. **45**, 1105 (1980).

[55] A. Pochelon *et al.*, "Electron Bernstein wave heating of over-dense H-mode plasmas in the TCV tokamak via O-X-B double mode conversion", Nucl. Fus. **47**, 1552 (2007).

[56] Y. Y. Podoba, "Radio Frequency Heating on the WEGA Stellarator", PhD Thesis, Max-Planck Institut für Plasmaphysik (2006).

[57] Y. Y. Podoba *et al.*, "Direct Observation of Electron-Bernstein Wave Heating by *O-X-B*-Mode Conversion at Low Magnetic Field in the WEGA Stellarator", Phys. Rev. Lett. **98**, 255003 (2007).

[58] J. Preinhaelter *et al.*, "Plans for Electron Bernstein Waves Emission Detection in COMPASS", In *35th EPS Conference on Plasma Physics*, P2.096 (2008).

[59] S. Puri *et al.*, "Dispersion curves for the generalized Bernstein modes", J. Plasma Phys. **9**, 89 (1973).

[60] A.K. Ram *et al.*, "Mode conversion of fast Alfvén waves at the ion-ion hybrid resonance", Phys. Plasmas **3** 1976 (1996).

[61] A.K. Ram *et al.*, "Excitation, propagation and damping of electron Bernstein waves in tokamaks", Phys. Plasmas **7** 4084 (2000).

[62] A. K. Ram *et al.*, "Electron Cyclotron Current Drive in Spherical Tokamaks with Application to ITER", In *22nd IAEA Fusion Energy Conference*, TH/P3-16 (2008).

[63] H. Saitoh *et al.*, "Confinement of Pure-Electron Plasmas in a Toroidal Magnetic-Surface Configuration", Phys. Rev. Lett. **92**, 255005 (2004).

[64] D. Sakata, "Polarization Spectroscopy in the Internal Coil Device Mini-RT" (in Japanese), Master Thesis, The University of Tokyo (2008).

[65] S. M. Shahruz, "A phase-locked loop", Rev. Sci. Instr. **72**, 1888 (2001).

[66] S. Shiraiwa *et al.*, "Heating by an Electron Bernstein Wave in a Spherical Tokamak Plasma via Mode Conversion", Phys. Rev. Lett. **96**, 185003 (2006).

[67] P. C. Stangeby, *The Plasma Boundary of Magnetic Fusion Devices*, Taylor & Francis Group, New York (2000).

[68] T. H. Stix, "Absorption of Plasma Waves", Phys. Fluids **3**, 19 (1960).

[69] T. H. Stix, "Radiation and Absorption via Mode Conversion in an Inhomogeneous Collisionfree Plasma", Phys. Rev. Lett. **15**, 878 (1965).

[70] H. Sugai, "Mode Conversion and Local Heating below the Second Electron Cyclotron Harmonic", Phys. Rev. Lett. **47**, 1899 (1981).

[71] D. G. Swanson, *Plasma Waves*, Institute of Physics, London (1989).

[72] K. Tanaka *et al.*, "Non-Solenoidal Formation of Spherical Torus by ECH/ECCD in LATE", In *22nd IAEA Fusion Energy Conference*, EX/P6-8 (2008).

[73] J. B. Taylor *et al.*, "Relaxation of Toroidal Plasma and Generation of Reverse Magnetic Fields", Phys. Rev. Lett. **33**, 1139 (1974).

[74] G. Taylor *et al.*, "Enhancement of mode-converted electron Bernstein wave emission during National Spherical Torus Experiment H-mode plasmas", Phys. Plasmas **9**, 167 (2002).

[75] W. B. Thompson, "Thermonuclear Reaction Rates", Proc. Phys. Soc. (London) **B70**, 1 (1957).

[76] N.A. Uckan, "Temperature limit in ECH hot electron plasmas", Phys. Fluids **25** 2381 (1982).

[77] F. Wagner *et al.*, "Regime of Improved Confinement and High Beta in Neutral-Beam-Heated Divertor Discharges of the ASDEX Tokamak", Phys. Rev. Lett. **49**, 1408 (1982).

[78] C. F. Wandel *et al.*, "A Compilation of some Rates and Cross Sections on Interest in Controlled Thermonuclear Research", Nucl. Instr. Methods **4**, 249 (1959).

[79] T. Watanabe, "Efficient Computation of the Plasma Dispersion Function $Z(\zeta)$", J. Plasma Fus. Res. **65**, 556 (1991).

[80] N. Yanagi *et al.*, "Engineering Development of an HTS Floating Coil for the Mini-RT Project" (in Japanese), J. Cryo. Soc. Jpn. **39**, 193 (2004).

[81] N. Yanagi *et al.*, "Cool-down and Excitation Tests of the HTS Floating Coil in the Mini-RT Project" (in Japanese), J. Cryo. Soc. Jpn. **39**, 201 (2004).

[82] E. Yatsuka *et al.*, "Electron Bernstein Wave Heating on the Internal Coil Device Mini-RT", Trans. Fusion Sci. and Tech **51**, 310 (2007).

[83] E. Yatsuka *et al.*, "Direct Measurement of an Electron Bernstein Wave on the Internal Coil Device Mini-RT", In *Proceedings of the Joint Conf. of 17th International Toki Conf. and 16th International Stellarator/Heliotron Workshop*, P2-092 (2007).

[84] E. Yatsuka *et al.*, "Direct Measurement of a Mode-Converted Electron Bernstein Wave in the Internal Coil Device Mini-RT", Plasma Fus. Res. **3**, 013 (2008).

[85] E. Yatsuka *et al.*, "Excitation and Propagation of Electron Bernstein Waves in the Internal Coil Device Mini-RT", In *Proceedings of the 35th EPS Conf. on Plasma Physics*, P4.109 (2008).

[86] E. Yatsuka *et al.*, "Radio-frequency Electromagnetic Field Measurements for Direct Detection of Electron Bernstein Waves in a Torus Plasma", Rev. Sci. Instrum. **80**, 023505 (2009).

[87] Z. Yoshida *et al.*, "Beltrami fields in plasmas: High-confinement mode boundary layers and high beta equilibria", Phys. Plasmas **8**, 2125 (2001).

[88] Z. Yoshida *et al.*, "Variational Principles and Self-Organization in Two-Fluid Plasmas", Phys. Rev. Lett. **88**, 095001 (2002).

[89] Z. Yoshida *et al.*, "First Plasma in the RT-1 Device", Plasma Fus. Res. **1**, 008 (2006).

[90] Z. Yoshida *et al.*, "High-β (Hot Electron) Plasma in Ring Trap 1 (RT-1)", In *22nd IAEA Fusion Energy Conference*, EX/P5-28 (2008).

[91] S. Yoshikawa *et al.*, "Axisymmetric Minimum Average B Configuration of a Triply Connected System", Phys. Fluids **9** 2295 (1966).

[92] S. Yoshikawa, "*Plasma · Fusion*" chapter 31 (in Japanese), Kyoritu Syuppan (1979).

Related Papers

Refereed Articles

1. E. Yatsuka, K. Kinjo, J. Morikawa, Y. Ogawa, "Radio-frequency Electromagnetic Field Measurements for Direct Detection of Electron Bernstein Waves in a Torus Plasma", Rev. Sci. Instrum. **80**, 023505 (2009).

2. E. Yatsuka, D. Sakata, K. Kinjo, J. Morikawa, Y. Ogawa, "Direct Measurement of a Mode-Converted Electron Bernstein Wave in the Internal Coil Device Mini-RT", Plasma Fusion Res. **3** 013 (2008).

3. E. Yatsuka, H. Kato, D. Sakata, J. Morikawa, Y. Ogawa, N. Yanagi, T. Mito, "Electron Bernstein Wave Heating on the Internal Coil Device Mini-RT", Trans. Fus. Sci. Tech. **51** 310 (2007).

Proceedings

1. E. Yatsuka, D. Sakata, K. Kinjo, S. Tanaka, J. Morikawa and Y. Ogawa, "Excitation and Propagation of Electron Bernstein Waves in the Internal Coil Device Mini-RT", 35th EPS Conf. on Plasma Physics, Crete, Greece, P4.109 (2008).

2. E. Yatsuka, D. Sakata, K. Kinjo, J. Morikawa and Y. Ogawa, "Direct Observation of Electron Bernstein Wave on the Internal Coil Device Mini-RT", Bull. APS 49th Ann. Meeting of the DPP , Orlando, U.S., YP8-61 (2007).

3. E. Yatsuka, D. Sakata, K. Kinjo, J. Morikawa and Y. Ogawa, "Direct Measurement of an Electron Bernstein Wave on the Internal Coil Device Mini-RT", Joint Conf. of 17th International Toki Conf. and 16th International Stellarator/Heliotron Workshop, Toki, Japan, P2-092 (2007).

Related Presentations

International

1. E. Yatsuka, D. Sakata, K. Kinjo, S. Tanaka, J. Morikawa and Y. Ogawa, "Excitation and Propagation of Electron Bernstein Waves in the Internal Coil Device Mini-RT", 35th European Physical Society Conference on Plasma Physics, Crete, Greece, June 9-13, P4.109.

2. E. Yatsuka, D. Sakata, K. Kinjo, J. Morikawa and Y. Ogawa, "Direct Observation of Electron Bernstein Wave on the Internal Coil Device Mini-RT", 49th Annual Meeting of the Division of Plasma Physics on American Physical Society, Orlando, U.S., November 12-16 2007, YP8-61.

3. E. Yatsuka, D. Sakata, K. Kinjo, J. Morikawa and Y. Ogawa, "Direct Measurement of an Electron Bernstein Wave on the Internal Coil Device Mini-RT", Joint Conf. of 17th International Toki Conf. and 16th International Stellarator/Heliotron Workshop, Toki, Japan, October 15-19 2007, P2-092.

4. E. Yatsuka, H. Kato, D. Sakata, J. Morikawa, Y. Ogawa, N. Yanagi, T. Mito, "Electron Bernstein Wave Heating on the Internal Coil Device Mini-RT", The Sixth International Conference on Open Magnetic Systems for Plasma Confinement, Tsukuba, Japan, July 17-21 2006, 19P35.

Domestic

1. E. Yatsuka, K. Kinjo, K. Uchijima, J. Morikawa, Y. Ogawa, "Overdense Plasma Production and the characteristics of ECRF electromagnetic field in the Internal

Coil Device Mini-RT", 25th Annual Meeting of the Japan Society of Plasma Science and Nuclear Fusion Research, Utsunomiya, December 2-5 2008, 4pB05.

2. E. Yatsuka, K. Kinjo, J. Morikawa, Y. Ogawa, "Excitation and Propagation of Electron Bernstein Waves in the Internal Coil Device Mini-RT", 2008 Autumn Meeting of the Physical Society of Japan, Morioka, September 20-23 2008, 21pZH-6.

3. E. Yatsuka, D. Sakata, K. Kinjo, J. Morikawa, Y. Ogawa, "Electron Bernstein Wave Detection Experiments on the Internal Coil Device Mini-RT (2)", 63th Annual Meeting of the Physical Society of Japan, Higashiosaka, March 22-26 2008, 26aQF-6.

4. E. Yatsuka, D. Sakata, K. Kinjo, J. Morikawa, Y. Ogawa, "Experiments on Propagation of an Electron Bernstein Wave in the Internal Coil Device Mini-RT", 24th Annual Meeting of the Japan Society of Plasma Science and Nuclear Fusion Research, Himeji, November 27-30 2007, 30aA38P.

5. E. Yatsuka, D. Sakata, K. Kinjo, J. Morikawa, Y. Ogawa, "Electron Bernstein Wave Detection Experiments on the Internal Coil Device Mini-RT", 62th Annual Meeting of the Physical Society of Japan, Sapporo, September 21-24 2007, 23pTB-5.

6. E. Yatsuka, H. Kato, D. Sakata, J. Morikawa, Y. Ogawa, N. Yanagi, T. Mito, "ECRF Electromagnetic Field Measurement on the Internal Coil Device Mini-RT", 2007 Spring Meeting of the Physical Society of Japan, Kagoshima, March 18-21 2007, 20pQE-6.

7. E. Yatsuka, H. Kato, D. Sakata, J. Morikawa, Y. Ogawa, N. Yanagi, T. Mito, "Development of ECRF Electromagnetic Field Measurement System for the Internal Coil Device Mini-RT", 23th Annual Meeting of the Japan Society of Plasma Science and Nuclear Fusion Research, Tsukuba, November 29- December 1 2006, 29aB29P.

8. E. Yatsuka, H. Kato, D. Sakata, J. Morikawa, Y. Ogawa, N. Yanagi, T. Mito, "Excitation and Absorption of Electron Bernstein Wave on the Internal Coil Device Mini-RT", 2006 Autumn Meeting of the Physical Society of Japan, Chiba, September 23-26 2006, 25aQA-11.

9. E. Yatsuka, H. Kato, D. Sakata, J. Morikawa, Y. Ogawa, N. Yanagi, T. Mito,

"Propagation and Heating Property of ECRF Wave on Internal Coil Device Mini-RT", 6th Fusion Energy Collaboration Meeting, Toyama, June 13-14 2006, 13A49.

10. E. Yatsuka, H. Kato, D. Sakata, T. Goto, J. Morikawa, Y. Ogawa, N. Yanagi, T. Mito, "Plasma Property for ECH Injection Mode on the Internal Coil Device Mini-RT", 22th Annual Meeting of the Japan Society of Plasma Science and Nuclear Fusion Research, Tokyo, November 29- December 2, 29aC39P.

11. E. Yatsuka, T. Goto, H. Kato, D. Sakata, J. Morikawa, Y. Ogawa, N. Yanagi and T. Mito, "Study on ECH Plasma Experiments for Generation of High Energy Electrons on the Internal Coil Device Mini-RT", 2006 Autumn Meeting of the Physical Society of Japan, Kyoto, September 19-22 2005, 19aW3.

Appendix A

THEORETICAL BASIS OF WAVES IN PLASMAS

Because an electron Bernstein wave (EBW) is an electrostatic mode, and its wavelength is comparable with an electron Larmor radius. In this chapter, an EBW and a cold plasma are described as adequately defined limit of a hot plasma.

A.1 Waves in Cold Plasmas

In this section, waves in cold plasmas are described. "Cold" means that a plasma has a small Larmor radius, i.e. the Larmor radius is much shorter than a wavelength.

A.1.1 Basic Equations

A plasma behaves as a dielectric medium, so that waves in a plasma are described by Maxwell equations,

$$\nabla \cdot \mathbf{E} = \frac{\rho}{\epsilon_0}, \tag{A.1}$$

$$\nabla \cdot \mathbf{B} = 0, \tag{A.2}$$

$$\nabla \times \mathbf{E} = -\frac{\partial \mathbf{B}}{\partial t}, \tag{A.3}$$

$$\nabla \times \mathbf{B} = \frac{1}{c^2}\frac{\partial \mathbf{E}}{\partial t} + \mu_0 \mathbf{j}, \tag{A.4}$$

where ρ and $\mathbf{j}$ denote a charge density and a current density, respectively, which are determined by the 0th and 1st moment of a distribution function,

$$\rho \;=\; \sum_s q_s \int d^3 v f_s, \tag{A.5}$$

$$\mathbf{j} \;=\; \sum_s q_s \int d^3 v f_s \mathbf{v}, \tag{A.6}$$

where f_s and q_s denote a distribution function and a charge of "s", respectively, and s denotes a specie.

The distribution function is determined by the Boltzmann equation,

$$\frac{\partial f_s}{\partial t} + \mathbf{v} \cdot \nabla_r f_s + \frac{q_s}{m_s}(\mathbf{E} + \mathbf{v} \times \mathbf{B}) \cdot \nabla_v f_s = \left(\frac{\delta f_s}{\delta t}\right)_{\mathrm{coll}}, \tag{A.7}$$

where m_s denotes a mass of s, and the right hand side of this equation denotes the collisional term for distribution function. We divide f, $\mathbf{B}$ and $\mathbf{E}$ into a steady term and perturbed ones, i.e. $f_j = f_{j0} + f_{j1}$, $\mathbf{B} = \mathbf{B_0} + \mathbf{B_1}$, $\mathbf{E} = \mathbf{E_1}$. Suffix 0 and 1 correspond to a steady value and perturbed ones, respectively, and we assumed a quasi-neutral plasma, i.e. $\mathbf{E_0} = 0$. A steady electric field plays important roles for a non-neutral plasma. In addition, we also assume right hand side of Eq.(A.7) is 0 for simplicity:

$$\frac{\partial f_s}{\partial t} + \mathbf{v} \cdot \nabla_r f_s + \frac{q_s}{m_s}(\mathbf{E} + \mathbf{v} \times \mathbf{B}) \cdot \nabla_v f_s = 0. \tag{A.8}$$

Equation (A.8) is called Vlasov equation.

A.1.2 Relasionship Between Electric Fields and Current Density

There is an essential difference between conductivity of a metal or an unmagnetized plasma and that of a magnetized plasma. The former one is a scalar, i.e. the direction of a current is parallel to the applied electric field. While, the latter one is a tensor, i.e. charged particles have both parallel and perpendicular velocity components due to the Lorentz force, thus

$$\mathbf{j_1} = \sum_s \overleftrightarrow{\sigma}_s \cdot \mathbf{E}. \tag{A.9}$$

Suffix 1 denotes an induced current density due to electric field. We can consider not only a plasma is a conductor but also that it is dielectric a medium. The polarization vector is defined by an induced current density:

$$\mathbf{j_1} = \frac{\partial \mathbf{P}}{\partial t}. \tag{A.10}$$

Then Eq.(A.4) is written as,

$$\nabla \times \mathbf{B}_1 = \frac{1}{c^2} \frac{\partial \mathbf{E}}{\partial t} + \mu_0 \mathbf{j}_1 = \epsilon_0 \mu_0 \frac{\partial \mathbf{E}}{\partial t} + \mu_0 \frac{\partial \mathbf{P}}{\partial t} = \mu_0 \frac{\partial}{\partial t} \left(\epsilon_0 \mathbf{E} + \mathbf{P} \right) \equiv \mu_0 \frac{\partial \mathbf{D}}{\partial t}, \quad (A.11)$$

where $\mathbf{D}$ is an electric displacement vector. By assuming perturbed values vary as $\exp[i(\mathbf{k} \cdot \mathbf{r} - \omega t)]$, we can find relationship between conductivity and a dielectric tensor,

$$\mathbf{D} = \overleftrightarrow{\epsilon} \cdot \mathbf{E} = \left(\epsilon_0 \overleftrightarrow{I} + \frac{i}{\omega} \sum_s \overleftrightarrow{\sigma}_s \right) \cdot \mathbf{E} \equiv \epsilon_0 \left(\overleftrightarrow{I} + \sum_s \overleftrightarrow{\chi}_s \right) \cdot \mathbf{E}, \quad (A.12)$$

where $\overleftrightarrow{\epsilon}$, $\overleftrightarrow{\sigma}$, $\overleftrightarrow{\chi}$ and $\overleftrightarrow{I}$ are the dielectric tensor, the conductivity tensor, the susceptibility tensor and the unit tensor, respectively. Detailed expression of these tensors are given in Section A.1.3 and later.

A.1.3 Dielectric Tensor for a Homogeneous Cold Plasma

In a cold plasma, a motion of each charged particle is equivalent to that of its guiding center. This section mentions about the corrective motion of charged particles in a fluctuated electromagnetic field. Taking zeroth order moment of Eq. (A.8), one can derive continuity equation

$$\frac{\partial n_s}{\partial t} + \nabla \cdot (n_s \mathbf{v}) = 0, \quad (A.13)$$

where n_s denotes a density of the particle 's', and the relationship between a density and a distribution function is

$$\int \mathrm{d}^3 \mathbf{v} f_s = n_s. \quad (A.14)$$

Taking the first moment of Eq. (A.8) and substituting Eq. (A.13) into Eq. (A.8), then

$$m_s n_s \frac{\mathrm{d} \mathbf{u}_s}{\mathrm{d}t} = -\nabla \cdot \overleftrightarrow{P}_s + q_s n_s (\mathbf{E} + \mathbf{u}_s \times \mathbf{B}), \quad (A.15)$$

where $\mathbf{u}_s$ and $\overleftrightarrow{P}_s$ denote a mean velocity and a pressure tensor of 's', which is defined as

$$\int \mathrm{d}^3 \mathbf{v} f_s \mathbf{v}_s = \mathbf{u}_s, \quad (A.16)$$

$$m_s n_s \int \mathrm{d}^3 \mathbf{v} f_s \mathbf{w}_s \mathbf{w}_s = \overleftrightarrow{P}_s, \quad (A.17)$$

where $\mathbf{w}_s \equiv \mathbf{v}_s - \mathbf{u}_s$. In a homogeneous plasma, the divergence of a pressure tensor is zero. On the other hand, pressure gradient plays important role in the inhomogeneous plasmas, i.e.

drift waves. As describes above, collective motion, which causes polarization current, can be represented by the cloud of single charged particles, i.e. from Eq. (A.15)

$$m_s \frac{d\mathbf{u}_s}{dt} = q_s(\mathbf{E} + \mathbf{u}_s \times \mathbf{B}). \tag{A.18}$$

Here let average velocity $\mathbf{u}_s$ expand into

$$\mathbf{u}_s(t) = \mathbf{u}_{s0} + \mathbf{u}_{s1}(t) + \cdots . \tag{A.19}$$

Averaging in Eq. (A.19) is the time average, whereas that in Eq. (A.16) is average in the velocity space. Non-trivial zeroth term of the equation of motion and Maxwell equations are

$$m_s \frac{d\mathbf{u}_{s0}}{dt} = q_s(\mathbf{E}_0 + \mathbf{u}_{s0} \times \mathbf{B}_0), \tag{A.20}$$

$$\nabla \times \mathbf{E}_0 = -\frac{\partial \mathbf{B}_0}{\partial t}, \tag{A.21}$$

$$\nabla \times \mathbf{B}_0 = \mu_0 \sum_s \mathbf{j}_{s0} + \frac{1}{c^2}\frac{\partial \mathbf{E}_0}{\partial t} = \mu_0 \sum_s q_s n_s \mathbf{u}_{s0}, \tag{A.22}$$

$$\nabla \cdot \mathbf{E}_0 = \frac{1}{\epsilon_0} \sum_s q_s n_s = 0, \tag{A.23}$$

Equation (A.23) means a quasi-neutral plasma. These lead $\mathbf{E}_0 = 0, \mathbf{u}_{s0} = 0$. In addition, we assume first order variables vary sinusoidally. Then,

$$-i\omega m_s \mathbf{u}_{s1} = q_s(\mathbf{E}_1 + \mathbf{u}_{s1} \times \mathbf{B}_0), \tag{A.24}$$

$$i\mathbf{k} \times \mathbf{E}_1 = i\omega \mathbf{B}_1, \tag{A.25}$$

$$i\mathbf{k} \times \mathbf{B}_1 = \mu_0 \sum_s \mathbf{j}_{s1} - \frac{i\omega}{c^2}\mathbf{E}_1 = -\frac{i\omega}{c^2}(\overleftrightarrow{I} + \overleftrightarrow{\chi}) \cdot \mathbf{E}_1. \tag{A.26}$$

From Eq. (A.24)

$$\left(1 - \frac{\Omega_s}{\omega}\right)v_{s+} = \frac{iq_s}{\omega m_s}E_+, \tag{A.27}$$

$$\left(1 + \frac{\Omega_s}{\omega}\right)v_{s-} = \frac{iq_s}{\omega m_s}E_-, \tag{A.28}$$

$$v_{sz} = \frac{iq_s}{\omega m_s}E_z, \tag{A.29}$$

where v_{s+}, v_{s-}, E_+, E_- and Ω_s are

$$v_{s+} = v_{sx} + iv_{sy}, \tag{A.30}$$

$$v_{s-} = v_{sx} - iv_{sy}, \tag{A.31}$$

$$E_+ = E_x + iE_y, \tag{A.32}$$

$$E_- = E_x - iE_y, \tag{A.33}$$

$$\Omega_s = \frac{q_s B}{m_s}, \tag{A.34}$$

respectively. Parameter Ω_s is called the cyclotron frequency. A polarization current due to a motion of particle 's' is

$$j_{s\pm} = n_s q_s v_{s\pm} = \frac{i n_s q_s^2}{m_s(\omega \pm \Omega_s) E_\pm} \equiv \sigma_{s\pm} E_\pm, \tag{A.35}$$

$$j_{sz} = n_s q_s v_{sz} = \frac{i n_s q_s^2}{m_s \omega E_z} = \sigma_z E_z. \tag{A.36}$$

Equation (A.35) derives

$$j_{sx} = \frac{j_{s+} + j_{s-}}{2} = \frac{\sigma_{s+} + \sigma_{s-}}{2} E_x + \frac{\sigma_{s+} - \sigma_{s-}}{2}(iE_y), \tag{A.37}$$

$$j_{sy} = \frac{j_{s+} - j_{s-}}{2i} = \frac{-\sigma_{s+} + \sigma_{s-}}{2}(iE_x) + \frac{\sigma_{s+} + \sigma_{s-}}{2} E_y. \tag{A.38}$$

Therefore, a dielectric tensor $\overleftrightarrow{\epsilon}$ is

$$
\begin{aligned}
\overleftrightarrow{\epsilon} &= \epsilon_0 \left(\overleftrightarrow{I} + \frac{i}{\epsilon_0 \omega} \overleftrightarrow{\sigma} \right) \\
&= \epsilon_0 \begin{pmatrix} S & -iD & 0 \\ iD & S & 0 \\ 0 & 0 & P \end{pmatrix},
\end{aligned} \tag{A.39}
$$

where S, D and P are defined as

$$S = 1 - \sum_s \frac{\omega_{ps}^2}{\omega^2 - \Omega_s^2}, \tag{A.40}$$

$$D = \sum_s \frac{\Omega_s}{\omega} \frac{\omega_{ps}^2}{\omega^2 - \Omega_s^2}, \tag{A.41}$$

$$P = 1 - \sum_s \frac{\omega_{ps}^2}{\omega^2}, \tag{A.42}$$

respectively, where plasma frequency ω_{ps} is defined as

$$\omega_{ps}^2 = \frac{n_s q_s^2}{\epsilon_0 m_s}. \tag{A.43}$$

Moreover, for the later discussion, parameters R and L are defined as

$$R = S + D = 1 - \sum_s \frac{\omega_{ps}^2}{\omega(\omega + \Omega_s)}, \tag{A.44}$$

$$L = S - D = 1 - \sum_s \frac{\omega_{ps}^2}{\omega(\omega - \Omega_s)}. \tag{A.45}$$

Note that if magnetic field is zero, i.e. $\Omega_s = 0$, Eq. (A.39) becomes scalar $\epsilon_0 P$, which is corresponding to permittivity of unmagnetized plasma.

In this work, we consider a hydrogen plasma and an electron cyclotron range of frequency (ECRF) if not otherwise specified. Each component of dielectric tensor of it is

$$S = 1 - \frac{\omega_{pe}^2}{\omega^2 - \Omega_e^2}, \tag{A.46}$$

$$D = \frac{\Omega_e}{\omega} \frac{\omega_{pe}^2}{\omega^2 - \Omega_e^2}, \tag{A.47}$$

$$P = 1 - \frac{\omega_{pe}^2}{\omega^2}, \tag{A.48}$$

$$R = 1 - \frac{\omega_{pe}^2}{\omega(\omega + \Omega_e)}, \tag{A.49}$$

$$L = 1 - \frac{\omega_{pe}^2}{\omega(\omega - \Omega_e)}. \tag{A.50}$$

A.1.4   Dispersion Relation of Homogeneous Cold Plasma Waves

The dispersion relation can be obtained from a dielectric tensor, which has been derived in the previous section. Substitute Eqs. (A.25) and (A.39) into (A.26) then

$$\mathbf{N} \times \mathbf{N} \times \mathbf{E}_1 + \overleftrightarrow{K} \cdot \mathbf{E}_1 = 0, \tag{A.51}$$

where a refractive index vector $\mathbf{N}$ and a specific dielectric tensor are $\mathbf{N} = \frac{c\mathbf{k}}{\omega}$, $\overleftrightarrow{K} = \overleftrightarrow{I} + \overleftrightarrow{\chi}$, respectively. Thus, let a refractive index vector $\mathbf{N}$ be as

$$\mathbf{N} = (N_x, 0, N_z) = (N\sin\theta, 0, N\sin\theta), \tag{A.52}$$

so that Eq. (A.51) is written as follows:

$$\begin{pmatrix} S - N^2\cos^2\theta & -iD & N^2\cos\theta\sin\theta \\ iD & S - N^2 & 0 \\ N^2\cos\theta\sin\theta & 0 & P - N^2\sin\theta \end{pmatrix} \begin{pmatrix} E_{1x} \\ E_{1y} \\ E_{1z} \end{pmatrix} = 0. \tag{A.53}$$

The determinant of 3 × 3 matrix in Eq. (A.53) should be 0 to have non-trivial solutions of Eq. (A.53), i.e.

$$AN^4 - BN^2 + C = 0, \tag{A.54}$$

where A, B and C are

$$A = S\sin^2\theta + P\cos^2\theta, \tag{A.55}$$

$$B = RL\sin^2\theta + PS(1 + \cos^2\theta), \tag{A.56}$$

$$C = PRL, \tag{A.57}$$

146

respectively. Equation (A.54) is a dispersion relation of a homogeneous cold plasma and the solutions of it are

$$N^2 = \frac{B \pm F}{2A},$$ (A.58)

where the parameter F is written as

$$F^2 = B^2 - 4AC = (RL - PS)^2 \sin^4\theta + 4P^2 D^2 \cos\theta.$$ (A.59)

For instance, if the propagation angle θ is equal to 0,

$$P = 0, N^2 = R, L,$$ (A.60)

and if θ is equal to $\pi/2$,

$$N^2 = \frac{RL}{S}, P.$$ (A.61)

Figure A.1 shows the directions of a wavenumber and a magnetic field. Obviously, an assumption in Eq. (A.52) does not break the generality of the direction of propagation since the system in consideration is rotationally symmetric around the magnetic field lines.
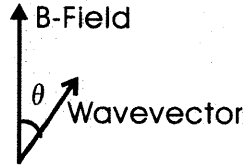
Figure A.1: Directions of a wavenumber and a magnetic field. The angle θ is the angle between the wavenumber vector and the magnetic field.

Each solution of dispersion relation, i.e. Eq. (A.54), gives its own eigenmode, so that we can obtain two independent polarizations,

$$E_x = i\frac{2AS - B \mp F}{2AD}E_y,$$ (A.62)

$$E_z = i\frac{-\dfrac{B \pm F}{2A}\cos\theta\sin\theta}{P - \dfrac{B \pm F}{2A}\sin^2\theta}\frac{2AS - B \mp F}{2AD}E_y,$$ (A.63)

where the double sign should be same order. If propagation direction θ equals to 0, then

$$E_x = \mp iE_y,$$ (A.64)

$$E_z = 0,$$ (A.65)

where the upper sign and lower one correspond to right hand mode (R-mode) and left hand mode (L-mode), respectively. In addition, if θ equals to $\pi/2$, one polarization is

$$E_x = E_y = 0, \quad E_z = \text{finite} \quad \text{(O-mode)}, \tag{A.66}$$

and another one is

$$E_z = 0, E_x = i\frac{D}{S}E_y \quad \text{(X-mode)}. \tag{A.67}$$

A.1.5 Cutoff and Resonance

The cutoff occurs when the refractive index $N = 0$, whereas the resonance does when $N = \infty$. If the refractive index is an imaginary number, the amplitude of a wave spatially increases or decreases. If $N = 0$ is the solution of the dispersion relation, parameter $C = 0$ should be satisfied, i.e.

$$P = 0, \quad \text{or} \quad R = 0, \quad \text{or} \quad L = 0. \tag{A.68}$$

The case of $P = 0$ is called a plasma cutoff (P-cutoff), which occurs when the wave propagates perpendicular to the magnetic field and the polarization of it is parallel to the magnetic field, i.e. corresponding dispersion relation is $N^2 = P$. The parameter P decreases with density increment, so that P-cutoff means that if a plasma density is higher than the cutoff density, i.e.

$$n_c = \frac{\epsilon_0 m}{e^2}\omega^2, \tag{A.69}$$

in such plasma, a wave cannot propagate. Here, for simplicity, we neglected the contribution from ions. As shown in Eq. (A.60), if the parameter P equals to 0 and a wave propagates parallel to the magnetic field, any wavelength satisfies the dispersion relation. That wave is so-called the plasma oscillation. In the case of $R = 0$, another cutoff which is called the right-hand cutoff (R-cutoff) occurs. For simplicity, we consider the two case of the propagating direction, i.e. $\theta = 0, \pi/2$. Polarization for the solution of the dispersion relation $N^2 = R$ ($\theta = 0$) corresponds to the right-hand sense of circular polarization. And $N^2 = \frac{RL}{S}$ corresponds to perpendicular both to the magnetic field and a wavevector polarization if plasma is tenuous, whereas the right-hand sense of circular polarization when $R = 0$ is satisfied. In an analogous way, one can easily find $L = 0$ corresponds to the cutoff of the wave exhibiting the left-hand sense of circular polarization (L-cutoff).

The resonance occurs when $A = 0$ or $B = \infty$. The former one corresponds to $S = 0$, which is so-called hybrid resonance, and latter one corresponds to $R = \infty$ or $L = \infty$, which are

so-called electron cyclotron resonance (ECR) and ion cyclotron resonance (ICR), respectively. More precisely, $R = \infty$ is taken place when $\omega + \Omega_s = 0$, so that only negative charged particles, e.g. negative ions and electrons, can resonate with a right hand wave. In this work, the hybrid resonance plays a crucial role. Now we assume a plasma with single ion species, i.e.

$$
\begin{aligned}
S &= 1 - \frac{\omega_{pe}^2}{\omega^2 - \Omega_e^2} - \frac{\omega_{pi}^2}{\omega^2 - \Omega_i^2} \\
&= \frac{\omega^4 - (\Omega_e^2 + \omega_{pe}^2 + \Omega_i^2 + \omega_{pi}^2)\omega^2 + (\Omega_e^2\Omega_i^2 + \omega_{pe}^2\Omega_i^2 + \omega_{pi}^2\Omega_e^2)}{(\omega^2 - \Omega_e^2)(\omega^2 - \Omega_i^2)} \equiv \omega^4 - \omega_1^2\omega^2 + \omega_2^4.
\end{aligned}
$$

$$(A.70)$$

The parameter S goes to zero when

$$
\omega^2 = \frac{1}{2}\left[\omega_1^2 \pm \sqrt{\omega_1^4 - 4\omega_2^4}\right] = \frac{\omega_1^2}{2}\left(1 \pm \left(1 - \frac{2\omega_2^4}{\omega_1^4}\right)\right) \sim \omega_1^2, \frac{\omega_2^4}{\omega_1^2}. \tag{A.71}
$$

Note that the electron mass is much smaller than that of ion. The upper hybrid resonance (UHR) occurs when $\omega^2 = \omega_1^2$, i.e.

$$
\omega_1^2 \sim (\Omega_e^2 + \omega_{pe}^2) \equiv \omega_{UH}^2, \tag{A.72}
$$

is satisfied. On the other hand, the lower hybrid resonance (LHR) occurs when $\omega^2 = \dfrac{\omega_2^4}{\omega_1^2}$, i.e.

$$
\frac{\omega_2^4}{\omega_1^2} \sim \frac{\omega_{pi}^2\Omega_e^2}{\Omega_e^2 - \dfrac{\Omega_e}{\Omega_i}\omega_{pi}^2} = \frac{\omega_{pi}^2\Omega_e\Omega_i}{\Omega_e\Omega_i - \omega_{pi}^2} = \left(\frac{1}{\omega_{pi}^2} + \frac{1}{|\Omega_e\Omega_i|}\right)^{-1} \equiv \omega_{LH}^2, \tag{A.73}
$$

is satisfied.

A.2 Waves in Hot (Kinetic) Plasma

As mentioned in the previous section, the cold plasma approximation is valid when a wavelength is much longer than the Larmor radius. At the resonance point, the cold plasma approximation fails because of shortening of a wavelength. Therefore, we have to consider a gyro-motion of charged particles and its interaction with wave.

A.2.1 Susceptibility Tensor for General Distribution Function

A dielectric tensor can be derived from a current induced by a perturbed electromagnetic field. Moreover, this current is due to a perturbed distribution function f_1. The Vlasov equation (A.8) determines a time evolution of a distribution function in the phase space. For simplicity, we consider linear response of a distribution function, thus a perturbed distribution function is treated as a small variation from an unperturbed distribution function.

In the Lagrangian frame, the Vlasov equation is represented as follows:

$$\left(\frac{\mathrm{d}f_s}{\mathrm{d}t}\right)_L = \frac{\partial f_s}{\partial t} + \frac{\partial f_s}{\partial \mathbf{r}_s} \cdot \frac{\mathrm{d}\mathbf{r}_s}{\mathrm{d}t} + \frac{\partial f_s}{\partial \mathbf{v}_s} \cdot \frac{\mathrm{d}\mathbf{v}_s}{\mathrm{d}t}, \tag{A.74}$$

where $\dfrac{\mathrm{d}\mathbf{r}_s}{\mathrm{d}t} = \mathbf{v}_s$ and $\dfrac{\mathrm{d}\mathbf{v}_s}{\mathrm{d}t} = \dfrac{q_s}{m_s}(\mathbf{E} + \mathbf{v}_s \times \mathbf{B}_0)$. In the uniform and steady plasma, the zeroth order of a distribution function obeys

$$\left(\frac{\mathrm{d}f_{s0}}{\mathrm{d}t}\right)_L = \frac{q_s}{m_s}\mathbf{v}_s \times \mathbf{B}_0 \cdot \frac{\partial f_{s0}}{\partial \mathbf{v}_s} = 0. \tag{A.75}$$

Similarly, the first order distribution function obeys

$$\left(\frac{\mathrm{d}(f_s - f_{s0})}{\mathrm{d}t}\right)_L = \frac{\partial f_{s1}}{\partial t} + \mathbf{v}_s \cdot \nabla f_{1s} + \frac{q_s}{m_s}\mathbf{v}_s \times \mathbf{B}_0 \cdot \frac{\partial f_{s1}}{\partial \mathbf{v}_s} + \frac{q_s}{m_s}(\mathbf{E}_1 + \mathbf{v}_s \times \mathbf{B}_1) \cdot \frac{\partial f_{s0}}{\partial \mathbf{v}_s} = 0. \tag{A.76}$$

Therefore, a time evolution of the first order distribution function is written in the Lagrangian frame,

$$\left(\frac{\mathrm{d}f_{s1}}{\mathrm{d}t}\right)_L = -\frac{q_s}{m_s}(\mathbf{E}_1 + \mathbf{v}_s \times \mathbf{B}_1) \cdot \frac{\partial f_{s0}}{\partial \mathbf{v}_s}. \tag{A.77}$$

In the Eulerian frame, a velocity is independent variable, so that we should relate a velocity in the Lagrangian frame with that in the Eulerian one. If a perturbation from the zeroth orbit by an electromagnetic wave is small, each particle moves on a unique trajectory. Therefore we can easily evaluate a distribution function at a time t from that at t' by solving the equation of motion with adequate initial conditions. Let a time, a location and a velocity of a charged particle be t', $\mathbf{x}'$ and $\mathbf{v}'$, respectively, equation of motion is written as

$$\frac{\mathrm{d}\mathbf{v}'_s}{\mathrm{d}t'} = \mathbf{v}'_s \times \mathbf{\Omega}_s, \tag{A.78}$$

where $\mathbf{\Omega_s}$ is a cyclotron frequency having a direction, i.e. $\mathbf{\Omega_s} = \dfrac{q_s \mathbf{B}}{m_s}$. The solution of Eq. (A.78) with $\mathbf{v}'_s = \mathbf{v}$ at $t' = t$ and $\mathbf{x}'_s = \mathbf{x}$ at $t' = t$ is represented as

$$v'_{sx} = v_x \cos\Omega_s(t - t') - v_y \sin\Omega_s(t - t'), \tag{A.79}$$

$$v'_{sy} = v_x \sin\Omega_s(t - t') + v_y \cos\Omega_s(t - t'), \tag{A.80}$$

$$v'_{sz} = v_z, \tag{A.81}$$

$$x'_s = x - \dfrac{v_x}{\Omega_s}\sin\Omega_s(t - t') + \dfrac{v_y}{\Omega_s}(1 - \cos\Omega_s(t - t')), \tag{A.82}$$

$$y'_s = y - \dfrac{v_x}{\Omega_s}(1 - \cos\Omega_s(t - t')) - \dfrac{v_y}{\Omega_s}\sin\Omega_s(t - t'), \tag{A.83}$$

$$z'_s = z - v_z(t - t'). \tag{A.84}$$

By using these relationships, the Vlasov equation in the Eulerian frame is represented as

$$f_{s1}(\mathbf{x}, \mathbf{v}, t)_E = -\dfrac{q_s}{m_s} \int_{t_0}^{t} dt' [\mathbf{E}_1(\mathbf{x}'_s(t')) + \mathbf{v}'_s \times \mathbf{B}_1(\mathbf{x}'_s(t'))] \cdot \nabla_{v'} f_0(\mathbf{x}'_s) + f_{s1}(\mathbf{x}'_s(t_0), \mathbf{v}'_s(t_0), t_0). \tag{A.85}$$

Hereafter, subscript E, which means the Eulerian, is dropped. Moreover, we assume the angular frequency of perturbed fields $\mathbf{E}_1$ and $\mathbf{B}_1$ have positive imaginary parts, i.e. a perturbed distribution function f_1 at $t' = -\infty$ equals to 0:

$$f_{s1}(\mathbf{x}, \mathbf{v}, t) = -\dfrac{q_s}{m_s} \int_{-\infty}^{t} dt' [\mathbf{E}_1(\mathbf{x}'_s(t')) + \mathbf{v}'_s \times \mathbf{B}_1(\mathbf{x}'_s(t'))] \cdot \nabla_{v'} f_0(\mathbf{x}'_s). \tag{A.86}$$

Perturbed electric and magnetic fields are

$$\mathbf{E}_1(\mathbf{x}, t) = \mathbf{E}\exp[i(\mathbf{k} \cdot \mathbf{x} - \omega t)], \tag{A.87}$$

$$\mathbf{B}_1(\mathbf{x}, t) = \mathbf{B}\exp[i(\mathbf{k} \cdot \mathbf{x} - \omega t)], \tag{A.88}$$

and from Eq. (A.3),

$$\mathbf{B}_1(\mathbf{x}, t) = \dfrac{\mathbf{k} \times \mathbf{E}_1}{\omega}\exp[i(\mathbf{k} \cdot \mathbf{x} - \omega t)] \tag{A.89}$$

can be obtained. Therefore first order of the Coulomb and Lorentz force are represented as

$$\left[\left(1 - \dfrac{\mathbf{k} \cdot \mathbf{v}'_s}{\omega}\right) \mathbf{E} - (\mathbf{v}'_s \cdot \mathbf{E})\dfrac{\mathbf{k}}{\omega}\right] \exp[i(\mathbf{k} \cdot \mathbf{x}'_s - \omega t)]. \tag{A.90}$$

Substituting Eqs. (A.82)-(A.84) into Eq. (A.90), the phase factor of it becomes

$$i\mathbf{k} \cdot \mathbf{x}'_s - i\omega t' = i\mathbf{k} \cdot \mathbf{x} - i\omega t + \dfrac{iv_x}{\Omega_s}[-k_x \sin\Omega_s \tau - k_y(1 - \cos\Omega_s \tau)]$$

$$+ \dfrac{iv_y}{\Omega_s}[-k_y \sin\Omega_s \tau + k_x(1 - \cos\Omega_s \tau)] + i(\omega - k_z v_z)\tau, \tag{A.91}$$

where $\tau = t - t'$. Moreover, since the parameters $v_\perp$ and v_z are constant, following equations,

$$f_{s0}(v_\perp, v_z) = f_{s0}(v'_\perp, v'_z),\tag{A.92}$$

$$\frac{\partial f_{s0}}{\partial v_x} = \frac{v_x}{v_\perp}\frac{\partial f_{s0}}{\partial v_\perp},\tag{A.93}$$

$$\frac{\partial f_{s0}}{\partial v_y} = \frac{v_y}{v_\perp}\frac{\partial f_{s0}}{\partial v_\perp},\tag{A.94}$$

are obtained. The amplitude of an integrand in Eq. (A.86) is

$$
\begin{aligned}
&\left[\left(1 - \frac{\mathbf{k}\cdot\mathbf{v}'_s}{\omega}\right)\mathbf{E} - (\mathbf{v}'_s\cdot\mathbf{E})\frac{\mathbf{k}}{\omega}\right]\cdot\nabla_{v'}f_{s0}(\mathbf{v}')\\
&= (E_x v'_{sx} + E_y v'_{sy})\left[\frac{1}{v_\perp}\frac{\partial f_{s0}}{\partial v_\perp} + \frac{k_z}{\omega}\left(\frac{\partial f_{s0}}{\partial v_z} - \frac{v'_z}{v_\perp}\frac{\partial f_{s0}}{\partial v_\perp}\right)\right]\\
&+ E_z\left[\frac{\partial f_{s0}}{\partial v_z} + -\frac{k_x v'_x + k_y v'_y}{\omega}\left(\frac{\partial f_{s0}}{\partial v_z} - \frac{v'_z}{v_\perp}\frac{\partial f_{s0}}{\partial v_\perp}\right)\right]\\
&= (v_x\cos\Omega_s\tau - v_y\sin\Omega_s\tau)\left[\frac{E_x}{v_\perp}\frac{\partial f_{s0}}{\partial v_\perp} + \frac{E_x k_z - E_z k_x}{\omega}\left(\frac{\partial f_{s0}}{\partial v_z} - \frac{v'_z}{v_\perp}\frac{\partial f_{s0}}{\partial v_\perp}\right)\right]\\
&+ (v_x\sin\Omega_s\tau + v_y\cos\Omega_s\tau)\left[\frac{E_y}{v_\perp}\frac{\partial f_{s0}}{\partial v_\perp} + \frac{E_y k_z - E_z k_y}{\omega}\left(\frac{\partial f_{s0}}{\partial v_z} - \frac{v'_z}{v_\perp}\frac{\partial f_{s0}}{\partial v_\perp}\right)\right]\\
&+ E_z\frac{\partial f_{s0}}{\partial v_z}.
\end{aligned}\tag{A.95}
$$

A first order distribution function in the Eulerian frame can be obtained from Eqs. (A.86), (A.91) and (A.95), which is a function of a zeroth order (unperturbed) distribution function. As shown in Eq. (A.91), the sinusoidal time evolution is contained in the sinusoidal (complex argument of exponential) phase factor of integrand. The Bessel function enables one to simplify the phase factor:

$$
\begin{aligned}
\exp[\mathrm{i}(\mathbf{k}\cdot\mathbf{x}'_s - \omega t')] &= \exp[\mathrm{i}(\mathbf{k}\cdot\mathbf{x} - \omega t)]\exp[-\mathrm{i}b_s(\sin(\phi - \psi + \Omega_s\tau) - \sin(\phi - \psi)) + \mathrm{i}a\tau]\\
&= \exp[\mathrm{i}(\mathbf{k}\cdot\mathbf{x} - \omega t)]\sum_{j,l=-\infty}^{\infty} J_j(b_s)J_l(b_s)e^{\mathrm{i}(j-l)(\phi-\psi)}e^{\mathrm{i}(\omega - l\Omega_s - k_z v_z)\tau},
\end{aligned}\tag{A.96}
$$

where $a \equiv (\omega - k_z v_z)$, $b_s \equiv k_\perp v_\perp/\Omega_s$, $v_x \equiv v_\perp\cos\phi$, $v_y \equiv v_\perp\sin\phi$, $k_x \equiv k_\perp\cos\psi$ and $k_y \equiv k_\perp\sin\psi$, respectively. In the Eq. (A.96), Bessel identity has been used:

$$e^{\mathrm{i}b_s\sin\theta} = \sum_{j=-\infty}^{\infty} J_j(b_s)e^{\mathrm{i}n\theta}.\tag{A.97}$$

An integral with respect to τ is represented as

$$\int \mathrm{d}\tau \rightarrow \frac{-\mathrm{i}}{\omega - l\Omega_s - k_z v_z},\tag{A.98}$$

152

moreover, we assumed ω has a positive imaginary part, then an integral constant should be zero, i.e. it means the zero amplitude at the time $t \to -\infty$. Equation (A.86) becomes

$$
\begin{aligned}
f_{s1}(\mathbf{x}, \mathbf{v}, t) &= \frac{-\mathrm{i}q_s}{m_s} \mathrm{e}^{\mathrm{i}(\mathbf{k} \cdot \mathbf{x} - \omega t)} \sum_{j=-\infty}^{\infty} \sum_{l=-\infty}^{\infty} \frac{J_j(b_s) \mathrm{e}^{\mathrm{i}(j-l)(\phi-\psi)}}{\omega - l\Omega_s - k_z v_z} \\
&\times \left[\frac{l J_l(b_s)}{b_s} \left(\frac{\partial f_{s0}}{\partial v_\perp} + \frac{k_z}{\omega} \left(v_\perp \frac{\partial f_{s0}}{\partial v_z} - v_z \frac{\partial f_{s0}}{\partial v_\perp} \right) \right) (E_x \cos\psi + E_y \sin\psi) \right. \\
&+ \mathrm{i}J_l'(b_s) \left(\frac{\partial f_{s0}}{\partial v_\perp} + \frac{k_z}{\omega} \left(v_\perp \frac{\partial f_{s0}}{\partial v_z} - v_z \frac{\partial f_{s0}}{\partial v_\perp} \right) \right) (-E_x \sin\psi + E_y \cos\psi) \\
&+ \left. J_l(b_s) \left(\frac{\partial f_{s0}}{\partial v_z} - \frac{l\Omega_s}{\omega} \left(\frac{\partial f_{s0}}{\partial v_z} - \frac{v_z}{v_\perp} \frac{\partial f_{s0}}{\partial v_\perp} \right) \right) E_z \right],
\end{aligned} \tag{A.99}
$$

where following Bessel identities have been used

$$
\frac{J_{n-1}(b_s) + J_{n+1}(b_s)}{2} = \frac{n}{b_s} J_n(b_s), \tag{A.100}
$$

$$
\frac{J_{n-1}(b_s) - J_{n+1}(s_s)}{2} = \frac{\mathrm{d}}{\mathrm{d}b_s} J_n(b_s) \equiv J_n'. \tag{A.101}
$$

In order to obtain a susceptibility tensor, the first order distribution function f_{s1} should be integrated in the velocity space. The relationship between a dielectric tensor and a conductivity tensor has been shown in Eq. (A.12), i.e.

$$
\begin{aligned}
\sum_s \mathbf{j}_s &= \sum_s q_s \int \mathrm{d}^3 v \begin{pmatrix} v_x \\ v_y \\ v_z \end{pmatrix} f_{s1} = \sum_s q_s \int_0^{2\pi} \mathrm{d}\phi \int_0^\infty v_\perp \mathrm{d}v_\perp \int_{-\infty}^\infty \mathrm{d}v_z \begin{pmatrix} v_x \\ v_y \\ v_z \end{pmatrix} f_{s1} \\
&= \sum_s q_s \int_0^{2\pi} \mathrm{d}\phi \int_0^\infty \mathrm{d}v_\perp \int_{-\infty}^\infty \mathrm{d}v_z \begin{pmatrix} \cos\phi \\ \sin\phi \\ \frac{v_z}{v_\perp} \end{pmatrix} f_{s1} = \overleftrightarrow{\sigma} \cdot \mathbf{E} = -\mathrm{i}\epsilon_0 \omega \left(\overleftrightarrow{K} - \overleftrightarrow{I} \right) \cdot \mathbf{E},
\end{aligned} \tag{A.102}
$$

where the specific dielectric tensor $\overleftrightarrow{K} = \dfrac{\overleftrightarrow{\epsilon}}{\epsilon_0}$. In order to integrate with respect to angular coordinate in the velocity space, following calculation is necessary:

$$
\sum_{j=-\infty}^\infty J_j(b_s) \int_0^{2\pi} \mathrm{d}\phi \mathrm{e}^{\mathrm{i}(j-l)(\phi-\psi)} \begin{pmatrix} \cos\phi \\ \sin\phi \\ \frac{v_z}{v_\perp} \end{pmatrix} = 2\pi \begin{pmatrix} \frac{l J_l(b_s)}{b_s} \cos\psi + \mathrm{i}J_l'(b_s)\sin\psi \\ \frac{l J_l(b_s)}{b_s} \sin\psi - \mathrm{i}J_l'(b_s)\cos\psi \\ \frac{v_z}{v_\perp} J_l(b_s) \end{pmatrix}. \tag{A.103}
$$

153

Equations (A.99) and (A.103) lead a specific dielectric tensor for a general velocity distribution function $f_{s0}(v_\perp, v_z)$ in a magnetized plasma:

$$\overleftrightarrow{K} = \begin{pmatrix} K_1 + \sin^2\psi K_0 & K_2 - \cos\psi\sin\psi K_0 & \cos\psi K_4 + \sin\psi K_5 \\ -K_2 - \cos\psi\sin\psi K_0 & K_1 + \cos^2\psi K_0 & \sin\psi K_4 - \cos\psi K_5 \\ \cos\psi K_6 - \sin\psi K_7 & \sin\psi K_6 + \cos\psi K_7 & K_3 \end{pmatrix}, \quad (A.104)$$

where

$$K_0 = \sum_s \frac{\omega_{ps}^2}{\omega} \sum_{l=-\infty}^{\infty} \int d^2v \frac{[b_s J_l'(b_s)]^2 - l^2 J_l^2(b_s)}{b_s^2(\omega - l\Omega_s - k_z v_z)} U_s, \quad (A.105)$$

$$K_1 = 1 + \sum_s \frac{\omega_{ps}^2}{\omega} \sum_{l=-\infty}^{\infty} \int d^2v \frac{l^2 J_l^2(b_s)}{b_s^2(\omega - l\Omega_s - k_z v_z)} U_s, \quad (A.106)$$

$$K_2 = i\sum_s \frac{\omega_{ps}^2}{\omega} \sum_{l=-\infty}^{\infty} \int d^2v \frac{l J_l(b_s) J_l'(b_s)}{b_s(\omega - l\Omega_s - k_z v_z)} U_s, \quad (A.107)$$

$$K_3 = 1 + \sum_s \frac{\omega_{ps}^2}{\omega} \sum_{l=-\infty}^{\infty} \int d^2v \frac{J_l^2(b_s)}{(\omega - l\Omega_s - k_z v_z)} W_{sl}, \quad (A.108)$$

$$K_4 = \sum_s \frac{\omega_{ps}^2}{\omega} \sum_{l=-\infty}^{\infty} \int d^2v \frac{l J_l^2(b_s)}{b_s(\omega - l\Omega_s - k_z v_z)} \frac{v_\perp}{v_z} W_{sl}, \quad (A.109)$$

$$K_5 = i\sum_s \frac{\omega_{ps}^2}{\omega} \sum_{l=-\infty}^{\infty} \int d^2v \frac{J_l(b_s) J_l'(b_s)}{(\omega - l\Omega_s - k_z v_z)} \frac{v_\perp}{v_z} W_{sl}, \quad (A.110)$$

$$K_6 = \sum_s \frac{\omega_{ps}^2}{\omega} \sum_{l=-\infty}^{\infty} \int d^2v \frac{l J_l^2(b_s)}{b_s(\omega - l\Omega_s - k_z v_z)} \frac{v_z}{v_\perp} U_s, \quad (A.111)$$

$$K_7 = i\sum_s \frac{\omega_{ps}^2}{\omega} \sum_{l=-\infty}^{\infty} \int d^2v \frac{J_l(b_s) J_l'(b_s)}{(\omega - l\Omega_s - k_z v_z)} \frac{v_z}{v_\perp} U_s, \quad (A.112)$$

where $\int d^2v \equiv 2\pi \int_{-\infty}^{\infty} dv_z \int_0^{\infty} v_\perp dv_\perp$, and U_s and W_{sl} is defined as

$$U_s \equiv v_\perp \left[\frac{\partial f_{s0}}{\partial v_\perp} \left(1 - \frac{k_z v_z}{\omega} \right) + \frac{k_z}{\omega} \frac{\partial f_{s0}}{\partial v_z} \right], \quad (A.113)$$

$$W_{sl} \equiv v_z \left[\frac{\partial f_{s0}}{\partial v_z} + \frac{l\Omega_s}{\omega} \left(\frac{v_z}{v_\perp} \frac{\partial f_{s0}}{\partial v_\perp} - \frac{\partial f_{s0}}{\partial v_z} \right) \right], \quad (A.114)$$

respectively. Equations (A.104)-(A.114) provide a dielectric tensor for a non-relativistic hot magnetized plasma with a general unperturbed distribution function f_0. This series expression is convenient to evaluate each order of the Larmor radius effect.

The cold plasma approximation can be obtained as the limit of a long-wavelength, i.e.

$b_s \to 0$, then

$$J_0(b_s) \to 1, \tag{A.115}$$

$$\frac{\mathrm{d}J_0(b_s)}{\mathrm{d}b_s} \to -\frac{b_s}{2}, \tag{A.116}$$

$$J_1(b_s) \to \frac{b_s}{2}, \tag{A.117}$$

$$J_{-1}(b_s) = J_1(b_s), \tag{A.118}$$

is obtained. Parameters $K_0 = K_4 = K_5 = K_6 = K_7 = 0$, and remaining are

$$K_1 \to S, \tag{A.119}$$

$$K_2 \to -iD, \tag{A.120}$$

$$K_3 \to P. \tag{A.121}$$

The series expansion form is not applicable when each term is of the order of unity or higher. We can simplify dielectric tensor by using sum rules of the Bessel function:

$$\sum_{n=-\infty}^{\infty} \frac{n^2 J_n^2(z)}{p-n} = \frac{\pi p^2}{\sin \pi p} J_p(z) J_{-p}(z) - p, \tag{A.122}$$

$$\sum_{n=-\infty}^{\infty} \frac{[J_n'(z)]^2}{p-n} = \frac{\pi}{\sin \pi p} J_p'(z) J_{-p}'(z) + \frac{p}{z^2}, \tag{A.123}$$

$$\sum_{n=-\infty}^{\infty} \frac{n J_n(z) J_n'(z)}{p-n} = \frac{\pi p}{\sin \pi p} J_p(z) J_{-p}'(z) + \frac{p}{z}, \tag{A.124}$$

$$\sum_{n=-\infty}^{\infty} \frac{n J_n(z) J_n'(z)}{p-n} = \frac{\pi p}{\sin \pi p} J_p(z) J_{-p}'(z) + \frac{p}{z}, \tag{A.125}$$

$$\sum_{n=-\infty}^{\infty} \frac{n J_n^2(z)}{p-n} = \frac{\pi p}{\sin \pi p} J_p(z) J_{-p}(z) - 1, \tag{A.126}$$

$$\sum_{n=-\infty}^{\infty} \frac{n J_n^2(z)}{p-n} = \frac{\pi p}{\sin \pi p} J_p(z) J_{-p}(z). \tag{A.127}$$

Elements of a dielectric tensor without infinite series are written as

$$
K_0 = \sum_s \frac{\omega_{ps}^2}{\omega \Omega_s} \int \mathrm{d}^2 v \left(\frac{\pi J'_{p_s}(b_s) J'_{-p_s}(b_s)}{\sin \pi p_s} + \frac{2 p_s}{b_s} - \frac{\pi p_s^2 J_{p_s}(b_s) J_{-p_s}(b_s)}{b_s^2 \sin \pi p_s} \right) U_s, \quad (A.128)
$$

$$
K_1 = 1 + \sum_s \frac{\omega_{ps}^2}{\omega \Omega_s} \int \mathrm{d}^2 v \left(\frac{\pi p_s^2 J_{p_s}(b_s) J_{-p_s}(b_s)}{b_s^2 \sin \pi p_s} - \frac{p_s}{b_s^2} \right) U_s, \quad (A.129)
$$

$$
K_2 = \mathrm{i} \sum_s \frac{\omega_{ps}^2}{\omega \Omega_s} \int \mathrm{d}^2 v \left(\frac{\pi p_s J_{p_s}(b_s) J'_{-p_s}(b_s)}{b_s \sin \pi p_s} + \frac{p_s}{b_s^2} \right) U_s, \quad (A.130)
$$

$$
K_3 = 1 + \sum_s \frac{\omega_{ps}^2}{\omega \Omega_s} \int \mathrm{d}^2 v \frac{\pi J_{p_s}(b_s) J_{-p_s}(b_s)}{\sin \pi p_s} W_{1s}
$$

$$
+ \sum_s \frac{\omega_{ps}^2}{\omega \Omega_s} \int \mathrm{d}^2 v \left(\frac{\pi p_s J_{p_s}(b_s) J_{-p_s}(b_s)}{\sin \pi p_s} - 1 \right) W_{2s}, \quad (A.131)
$$

$$
K_4 = \sum_s \frac{\omega_{ps}^2}{\omega \Omega_s} \int \mathrm{d}^2 v \left(\frac{\pi p_s J_{p_s}(b_s) J_{-p_s}(b_s)}{\sin \pi p_s} - 1 \right) \frac{1}{b_s} \frac{v_\perp}{v_z} W_{1s}
$$

$$
+ \sum_s \frac{\omega_{ps}^2}{\omega \Omega_s} \int \mathrm{d}^2 v \left(\frac{\pi p_s^2 J_{p_s}(b_s) J_{-p_s}(b_s)}{\sin \pi p_s} - p_s \right) \frac{1}{b_s} \frac{v_\perp}{v_z} W_{2s}, \quad (A.132)
$$

$$
K_5 = \mathrm{i} \sum_s \frac{\omega_{ps}^2}{\omega \Omega_s} \int \mathrm{d}^2 v \left(\frac{\pi J_{p_s}(b_s) J'_{-p_s}(b_s)}{\sin \pi p_s} + \frac{1}{b_s} \right) \frac{v_\perp}{v_z} W_{1s}
$$

$$
+ \mathrm{i} \sum_s \frac{\omega_{ps}^2}{\omega \Omega_s} \int \mathrm{d}^2 v \left(\frac{\pi p_s J_{p_s}(b_s) J'_{-p_s}(b_s)}{\sin \pi p_s} + \frac{p_s}{b_s} \right) \frac{v_\perp}{v_z} W_{2s}, \quad (A.133)
$$

$$
K_6 = \sum_s \frac{\omega_{ps}^2}{\omega \Omega_s} \int \mathrm{d}^2 v \left(\frac{\pi p_s J_{p_s}(b_s) J_{-p_s}(b_s)}{b_s \sin \pi p_s} - \frac{1}{b_s} \right) \frac{v_z}{v_\perp} U_s, \quad (A.134)
$$

$$
K_7 = \mathrm{i} \sum_s \frac{\omega_{ps}^2}{\omega \Omega_s} \int \mathrm{d}^2 v \left(\frac{\pi J_{p_s}(b_s) J'_{-p_s}(b_s)}{b_s \sin \pi p_s} + \frac{1}{b_s} \right) \frac{v_z}{v_\perp} U_s, \quad (A.135)
$$

where $p_s = \dfrac{\omega - k_z v_z}{\Omega_s}$, $W_{1s} = v_z \dfrac{\partial f_{s0}}{\partial v_z}$, $W_{2s} = \dfrac{v_z \Omega_s}{\omega} \left(\dfrac{v_z}{v_\perp} \dfrac{\partial f_{s0}}{\partial v_\perp} - \dfrac{\partial f_{s0}}{\partial v_z} \right)$ and $W_{sl} = W_{1s} + l W_{2s}$, respectively.

156

A.2.2 Susceptibility Tensor for the Maxwellian Distribution

As well known, the Maxwellian distribution function is one of the simplest solution of Eq. (A.75). First, only perpendicular directions are treated, so that f_{s0} with a perpendicular temperature $T_{s\perp}$ can be written as

$$f_{s0}(v_\perp, v_z) = \frac{n_s F_s(v_z)}{\pi v_{sT}^2} e^{-v_\perp^2/v_{sT}^2}, \tag{A.136}$$

where the perpendicular thermal velocity $v_t = \left(\dfrac{2\kappa T_{s\perp}}{m_s}\right)^{1/2}$. The derivatives of f_{s0} with respect to $v_\perp$ and v_z are

$$\frac{\partial f_{s0}}{\partial v_\perp} = -\frac{2n_s v_\perp}{v_{sT}^2} \frac{F_s(v_z)}{\pi v_{sT}^2} e^{-v_\perp^2/v_{sT}^2}, \tag{A.137}$$

$$\frac{\partial f_{s0}}{\partial v_z} = \frac{n_s F_s(v_z)'}{\pi v_{sT}^2} e^{-v_\perp^2/v_{sT}^2}, \tag{A.138}$$

respectively, where $F_s' \equiv \dfrac{\mathrm{d}F_s}{\mathrm{d}v_z}$. Substituting Eqs. (A.137) and (A.138) into Eqs. (A.95) and (A.86), we obtain

$$\begin{aligned}
f_{s1}(\mathbf{x}, \mathbf{v}, t) = & -\frac{q_s}{m_s \pi v_{sT}^2} e^{\mathrm{i}(\mathbf{k}\cdot\mathbf{x}-\omega t)} \int_0^\infty \mathrm{d}\tau (A_{sx} v_x + A_{sy} v_y + \alpha_{sz}) \\
& \times \exp\left[-\frac{v_x^2 + v_y^2}{v_{sT}^2} - \mathrm{i}(a_{sx} v_x - a_{sy} v_y) + \mathrm{i}(\omega - k_z v_z)\tau\right],
\end{aligned} \tag{A.139}$$

where

$$a_{sx} = \frac{1}{\Omega_s}[k_x \sin\Omega_s \tau + k_y(1 - \cos\Omega_s \tau)], \tag{A.140}$$

$$a_{sy} = \frac{1}{\Omega_s}[k_y \sin\Omega_s \tau - k_x(1 - \cos\Omega_s \tau)], \tag{A.141}$$

$$A_{sx} = \alpha_{sx}\cos\Omega_s \tau + \alpha_{sy}\sin\Omega_s \tau, \tag{A.142}$$

$$A_{sy} = \alpha_{sy}\cos\Omega_s \tau - \alpha_{sx}\sin\Omega_s \tau, \tag{A.143}$$

$$\frac{\alpha_{sx}}{n_s} = -\frac{2F_s}{v_{sT}^2} E_x + \left(F_s' + \frac{2v_z}{v_{sT}^2} F_s\right)\left(\frac{k_z E_x - k_x E_z}{\omega}\right), \tag{A.144}$$

$$\frac{\alpha_{sy}}{n_s} = -\frac{2F_s}{v_{sT}^2} E_y + \left(F_s' + \frac{2v_z}{v_{sT}^2} F_s\right)\left(\frac{k_z E_y - k_y E_z}{\omega}\right), \tag{A.145}$$

$$\frac{\alpha_{sz}}{n_s} = F_s' E_z. \tag{A.146}$$

In order to obtain a susceptibility tensor, integrating $f_{s1}\mathbf{v}$ in the velocity space should be done:

$$< v_x f_{s1} >_\perp \equiv \int dv_x \int dv_y v_x f_{s1}$$

$$= \frac{q_s}{m_s} \int_0^\infty d\tau e^{\phi_s} \left[\frac{v_{sT}^4}{4}(A_x a_x + A_y a_y)a_x + \frac{v_{sT}^2}{2}(ia_x \alpha_z - A_x) \right], \quad (A.147)$$

$$< v_y f_{s1} >_\perp \equiv \int dv_x \int dv_y v_y f_{s1}$$

$$= \frac{q_s}{m_s} \int_0^\infty d\tau e^{\phi_s} \left[\frac{v_{sT}^4}{4}(A_x a_x + A_y a_y)a_y + \frac{v_{sT}^2}{2}(ia_y \alpha_z - A_y) \right], \quad (A.148)$$

$$< v_z f_{s1} >_\perp \equiv \int dv_x \int dv_y v_z f_{s1}$$

$$= \frac{q_s}{m_s} \int_0^\infty d\tau e^{\phi_s} v_z \left[\frac{iv_{sT}^2}{2}(A_x a_x + A_y a_y) - \alpha_z \right], \quad (A.149)$$

where the parameters ϕ_s and λ_s are written as

$$\phi_s = i(\omega - k_z v_z)\tau - \lambda_s(1 - \cos\Omega_s\tau), \quad (A.150)$$

$$\lambda_s = \frac{1}{2}k_\perp^2 \rho_{Ls}^2. \quad (A.151)$$

and the averaged Larmor radius for species 's' is defined as $\rho_{sL} = \dfrac{v_{sT}}{\Omega_s}$.

In order to integrate Eqs. (A.147)-(A.149) with respect to time, the following identity is convenient:

$$e^{\lambda_s \cos\Omega_s\tau} = \sum_{l=-\infty}^{\infty} I_l(\lambda_s)e^{il\Omega_s\tau} = \sum_{l=-\infty}^{\infty} I_l(\lambda_s)e^{-il\Omega_s\tau}, \quad (A.152)$$

where $I_l(\lambda_s)$ is the modified Bessel function of the first kind. Since the following equation is satisfied,

$$\sum_{l=-\infty}^{\infty} \int_0^\infty d\tau I_l(\lambda_s)e^{i(\omega - l\Omega_s - k_z v_z)\tau} \begin{pmatrix} 1 \\ \cos\Omega_s\tau \\ \sin\Omega_s\tau \\ \cos\Omega_s\tau\cos\Omega_s\tau \\ \sin^2\Omega_s\tau \end{pmatrix}$$

$$= \sum_{l=-\infty}^{\infty} \begin{pmatrix} iI_l(\lambda_s) \\ iI_l'(\lambda_s) \\ \frac{l}{\lambda_s}I_l(\lambda_s) \\ \frac{l}{\lambda_s^2}(\lambda_s I_l'(\lambda_s) - I_l(\lambda_s)) \\ \frac{i}{\lambda_s^2}(\lambda_s I_l'(\lambda_s) - l^2 I_l(\lambda_s)) \end{pmatrix} \frac{1}{\omega - l\Omega_s - k_z v_z}, \quad (A.153)$$

equations (A.147)-(A.149) can be written as

$$< v_x f_{s1} >_\perp = -\frac{iv_{sT}^2 q_s e^{-\lambda}}{2\Omega_s m_s} \sum_{l=-\infty}^{\infty} \frac{\kappa_{lx} l I_l + (i\kappa_{ly} - \kappa_- k_y v_{sT}^2/\Omega_s)\lambda_s(I_l - I_l')}{\omega - l\Omega_s - k_z v_z}, \quad \text{(A.154)}$$

$$< v_y f_{s1} >_\perp = -\frac{iv_{sT}^2 q_s e^{-\lambda}}{2\Omega_s m_s} \sum_{l=-\infty}^{\infty} \frac{\kappa_{ly} l I_l + (i\kappa_{lx} - \kappa_- k_x v_{sT}^2/\Omega_s)\lambda_s(I_l - I_l')}{\omega - l\Omega_s - k_z v_z}, \quad \text{(A.155)}$$

$$< v_z f_{s1} >_\perp = \frac{iv_{sT}^2 q_s e^{-\lambda} v_z}{2\Omega_s m_s} \sum_{l=-\infty}^{\infty} \frac{\kappa_+ l I_l/\lambda_s + i\kappa_-(I_l - I_l') - 2\alpha_z \Omega_s I_l/v_{sT}^2}{\omega - l\Omega_s - k_z v_z}, \quad \text{(A.156)}$$

where $\kappa_+ = \alpha_x k_x + \alpha_y k_y$, $\kappa_- = \alpha_y k_x - \alpha_x k_y$, $\kappa_{lx} = \alpha_x l\Omega_s - \alpha_z k_x$ and $\kappa_{ly} = \alpha_y l\Omega_s - \alpha_z k_y$, respectively.

Next, we shall integrate over the parallel velocity. We assume that the parallel distribution function $F_s(v_z)$ is the shifted Maxwellian, i.e.

$$F_s(v_z) = \frac{1}{\sqrt{\pi} v_{sL}} \exp\left[-\frac{(v_z - u_{s0})^2}{v_{sL}^2}\right], \quad \text{(A.157)}$$

where v_{sL} is the parallel thermal velocity, which is defined as $v_{sL} = \dfrac{2\kappa T_{s//}}{m_s}$. Now we define a function $F_{sl,m}$ as

$$F_{sl,m} = \int_{-\infty}^{\infty} dv_z \frac{v_z^m F_s(v_z)}{\omega + l\Omega_s - k_z v_z},$$

$$F_{sl,m}(\zeta_{sl}) = -\frac{1}{k_z v_{sL}\sqrt{\pi}} \int_{-\infty}^{\infty} du' \frac{(u_{s0} + u' v_{sL})^m e^{-u'^2}}{u' - \zeta_{s,n}}, \quad \text{(A.158)}$$

where

$$u' = \frac{v_z - u_{s0}}{v_{sL}}, \quad \text{(A.159)}$$

$$\zeta_{sl} = \frac{\omega + l\Omega_s - k_z u_{s0}}{k_z v_{sL}}. \quad \text{(A.160)}$$

Then we obtain

$$F_{sl,0}(\zeta_{sl}) = -\frac{1}{k_z v_{sL}} Z(\zeta_{sl}), \quad \text{(A.161)}$$

$$F_{sl,1}(\zeta_{sl}) = \frac{1}{k_z}\left[\frac{1}{2}Z'(\zeta_{sl}) - \frac{u_{s0}}{v_{sL}}Z(\zeta_{sl})\right], \quad \text{(A.162)}$$

$$F_{sl,2}(\zeta_{sl}) = \frac{v_{sL}}{k_z}\left[\left(\frac{\zeta_{sl}}{2} + \frac{u_{s0}}{v_{sL}}\right)Z'(\zeta_{sl}) - \frac{u_{s0}^2}{v_{sL}^2}Z(\zeta_{sl})\right], \quad \text{(A.163)}$$

$$\int_{-\infty}^{\infty} dv_z \frac{F'(v_z)}{\omega + l\Omega_s - k_z v_z} = -\frac{1}{k_z v_{sL}^2} Z'(\zeta_{sl}), \quad \text{(A.164)}$$

$$\int_{-\infty}^{\infty} dv_z \frac{v_z F'(v_z)}{\omega + l\Omega_s - k_z v_z} = -\frac{1}{k_z v_{sL}}\left(\zeta_{sl} + \frac{u_{s0}}{v_{sL}}\right) Z'(\zeta_{sl}), \quad \text{(A.165)}$$

where the functions $Z\zeta_{sl}$ and $Z'(\zeta_{sl})$ are the plasma dispersion function and its derivative with respect to ζ_{sl} [17]. The perturbed current density can be obtained from the following equation:

$$\mathbf{j}_1 = \sum_s q_s \int_{-\infty}^{\infty} dv_z [< v_x f_{s1} >_\perp \hat{x} + < v_y f_{s1} >_\perp \hat{y} + < v_z f_{s1} >_\perp \hat{z}]. \qquad (A.166)$$

Therefore a dielectric tensor for the Maxwellian distribution function is

$$\overleftrightarrow{K} = \begin{pmatrix} K_1 + \sin^2\psi K_0 & K_2 - \cos\psi\sin\psi K_0 & \cos\psi K_4 + \sin\psi K_5 \\ -K_2 - \cos\psi\sin\psi K_0 & K_1 + \cos^2\psi K_0 & \sin\psi K_4 - \cos\psi K_5 \\ \cos\psi K_4 - \sin\psi K_5 & \sin\psi K_4 + \cos\psi K_5 & K_3 \end{pmatrix}, \qquad (A.167)$$

where

$$K_0 = 2\sum_s \frac{\omega_{ps}^2 e^{-\lambda_s}}{\omega k_z v_{sL}} \sum_{l=-\infty}^{\infty} \lambda_s (I_l(\lambda_s) - I_l'(\lambda_s)) A_{sl}, \qquad (A.168)$$

$$K_1 = 1 + \sum_s \frac{\omega_{ps}^2 e^{-\lambda_s}}{\omega k_z v_{sL}} \sum_{l=-\infty}^{\infty} \lambda_s \frac{l^2 I_l(\lambda_s)}{\lambda_s} A_{sl}, \qquad (A.169)$$

$$K_2 = i\sum_s \frac{\omega_{ps}^2 e^{-\lambda_s}}{\omega k_z v_{sL}} \sum_{l=-\infty}^{\infty} l(I_l(\lambda_s) - I_l'(\lambda_s)) A_{sl}, \qquad (A.170)$$

$$K_3 = 1 - \sum_s \frac{\omega_{ps}^2 e^{-\lambda_s}}{\omega k_z v_{sL}} \sum_{l=-\infty}^{\infty} I_l(\lambda_s) \frac{\omega + l\Omega_s}{k_z v_{sL}} B_{sl}, \qquad (A.171)$$

$$K_4 = \sum_s \frac{k_\perp \omega_{ps}^2 e^{-\lambda_s}}{\omega k_z \Omega_s} \sum_{l=-\infty}^{\infty} \frac{l I_l(\lambda_s)}{\lambda_s} C_{sl}, \qquad (A.172)$$

$$K_5 = i\sum_s \frac{k_\perp \omega_{ps}^2 e^{-\lambda_s}}{\omega k_z \Omega_s} \sum_{l=-\infty}^{\infty} (I_l(\lambda_s) - I_l'(\lambda_s)) C_{sl}, \qquad (A.173)$$

$$A_{sl} = \left[\left(1 - \frac{k_z u_{s0}}{\Omega_s}\right) + \frac{k_z v_{sL}}{\omega}\left(1 - \frac{T_{\perp s}}{T_{//s}}\right)\frac{Z'(\zeta_{sl})}{2}\right], \qquad (A.174)$$

$$B_{sl} = \left[1 + \frac{l\Omega_{sl}}{\omega}\left(1 - \frac{T_{\perp s}}{T_{//s}}\right)Z'(\zeta_{sl}) + \frac{2l\Omega_s T_{//s} u_{s0}}{\omega T_{\perp s} v_{sL}}\left(Z(\zeta_{sl}) + \frac{k_z v_{sl}}{\omega + l\Omega_s}\right)\right], \qquad (A.175)$$

$$C_{sl} = \left[\frac{l\Omega_s u_{s0}}{\omega v_{sL}} Z(\zeta_{sl}) + \left[\frac{T_{\perp s}}{T_{//s}} - \frac{l\Omega_s}{\omega}\left(1 - \frac{T_{\perp s}}{T_{//s}}\right)\right]\frac{Z'(\zeta_{sl})}{2}\right]. \qquad (A.176)$$

If the parallel and the perpendicular temperatures have a same value and assuming there is no flow, i.e. $T_{//} = T_{\perp}$, $u_{s0} = 0$, each component of the dielectric tensor is simplified as follows:

$$K_0 = 2 \sum_s \frac{\omega_{ps}^2 e^{-\lambda_s}}{\omega k_z v_{sL}} \sum_{l=-\infty}^{\infty} \lambda_s (I_l(\lambda_s) - I_l'(\lambda_s)) Z(\zeta_{sl}), \tag{A.177}$$

$$K_1 = 1 + \sum_s \frac{\omega_{ps}^2 e^{-\lambda_s}}{\omega k_z v_{sL}} \sum_{l=-\infty}^{\infty} \frac{l^2 I_l(\lambda_s)}{\lambda_s} Z(\zeta_{sl}), \tag{A.178}$$

$$K_2 = i \sum_s \frac{\omega_{ps}^2 e^{-\lambda_s}}{\omega k_z v_{sL}} \sum_{l=-\infty}^{\infty} l(I_l(\lambda_s) - I_l'(\lambda_s)) Z(\zeta_{sl}), \tag{A.179}$$

$$K_3 = 1 - \sum_s \frac{\omega_{ps}^2 e^{-\lambda_s}}{\omega k_z v_{sL}} \sum_{l=-\infty}^{\infty} I_l(\lambda_s) \zeta_{sl} Z'(\zeta_{sl}), \tag{A.180}$$

$$K_4 = \sum_s \frac{k_{\perp} \omega_{ps}^2 e^{-\lambda_s}}{2\omega k_z \Omega_s} \sum_{l=-\infty}^{\infty} \frac{l I_l(\lambda_s)}{\lambda_s} Z'(\zeta_{sl}), \tag{A.181}$$

$$K_5 = i \sum_s \frac{k_{\perp} \omega_{ps}^2 e^{-\lambda_s}}{2\omega k_z \Omega_s} \sum_{l=-\infty}^{\infty} (I_l(\lambda_s) - I_l'(\lambda_s)) Z'(\zeta_{sl}). \tag{A.182}$$

A.3 Plasma Dispersion Function

Definition of the plasma dispersion function is [17]

$$Z(\zeta) \equiv \frac{1}{\sqrt{\pi}} \int_{-\infty}^{\infty} \frac{e^{-x^2} dx}{x - \zeta} \quad \mathrm{Im}(\zeta) > 0. \tag{A.183}$$

If the absolute value of ζ is less than unity, the power series expansion is convenient:

$$\begin{aligned} Z(\zeta) &= i\sqrt{\pi} \sum_{n=0}^{\infty} \frac{(i\zeta)^n}{\Gamma\left(\frac{n}{2} + 1\right)} \\ &= i\sqrt{\pi} e^{-\zeta^2} - 2\zeta \left[1 - \frac{2}{3}\zeta^2 + \frac{4}{15}\zeta^4 + \cdots \right]. \end{aligned} \tag{A.184}$$

On the other hand, if the absolute value of ζ is much greater than unity, the asymptotic is useful:

$$\begin{aligned} Z(\zeta) &= -\frac{1}{\zeta} \sum_{n=0}^{N} \frac{(2n-1)!!}{(2\zeta^2)^n} + i\sigma\sqrt{\pi} e^{-\zeta^2} \\ &= -\frac{1}{\zeta} \left[1 + \frac{1}{2\zeta^2} + \frac{3}{4\zeta^4} + \cdots \right] + i\sigma\sqrt{\pi} e^{-\zeta^2}, \end{aligned} \tag{A.185}$$

where $(-1)!! = 1$, N indicates the series truncates when successive terms no longer decrease in magnitude, and

$$\sigma = \begin{cases} 0 & (\mathrm{Im}(\zeta) > 0) \\ 1 & (\mathrm{Im}(\zeta) = 0) \\ 2 & (\mathrm{Im}(\zeta) < 0). \end{cases} \tag{A.186}$$

Figure A.2 shows the real part of the plasma dispersion function with the power series and the asymptotic expansion forms when a imaginary part of an argument equals to zero. Plasma dispersion function is calculated by using a numerical code, which was developed by T. Watanabe [79]. One can see that real part of the plasma dispersion function goes to minimum value of ~ -1.08 when the valuable x is around 0.92. In addition, imaginary part of the plasma dispersion relation, which is monotonic function, is shown in Fig. A.3.
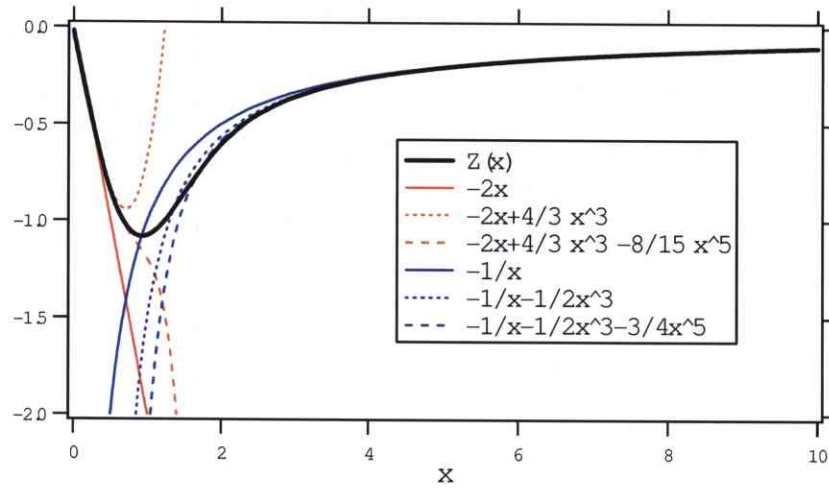

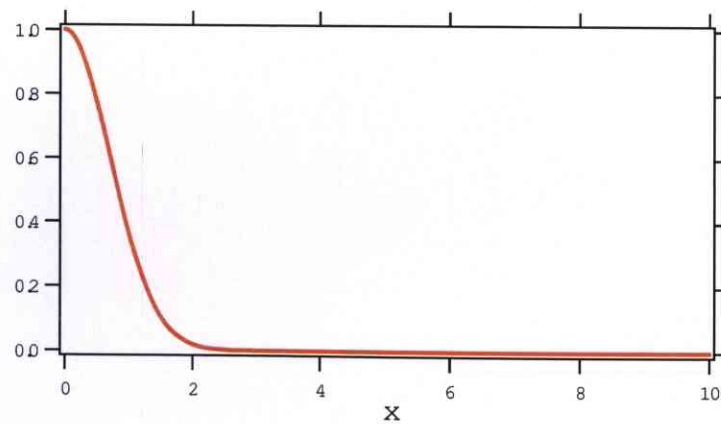Figure A.2: Real part of the plasma dispersion function.

Figure A.3: imaginary part of the plasma dispersion function.

A.4 Damping of Waves in Plasmas

A plasma can be heated by the energy transformation from a field to a plasma. The decay of a field energy can be derived from Maxwell equations, i.e. Eqs. (A.3), (A.4)

$$\nabla \cdot \mathbf{Y} + \mathbf{E} \cdot \frac{\partial \mathbf{D}}{\partial t} + \frac{1}{\mu_0} \mathbf{B} \cdot \frac{\partial \mathbf{B}}{\partial t} = 0, \tag{A.187}$$

where $\mathbf{Y}$ is the Poynting vector

$$\mathbf{Y} = \mathbf{E} \times \frac{1}{\mu_0} \mathbf{B}. \tag{A.188}$$

Second and third terms of Eq. (A.187) are electric and magnetic energy, respectively. Time average of the product of virtually periodic value A and B is written as

$$\overline{AB} \equiv \text{Re}[A]\text{Re}[B] = \frac{1}{4}(A_0 B_0^* + A_0^* B_0)\exp(2\phi_i) = (A_0 B_0^* + A_0^* B_0)\exp\left[2\int_{-\infty}^{t} \omega_i \mathrm{d}t'\right], \tag{A.189}$$

where we assumed A and B vary as

$$A = A_0\exp\left[-\mathrm{i}\int_{-\infty}^{t} (\omega_r + \mathrm{i}\omega_i)\mathrm{d}t'\right], \tag{A.190}$$

$$B = B_0\exp\left[-\mathrm{i}\int_{-\infty}^{t} (\omega_r + \mathrm{i}\omega_i)\mathrm{d}t'\right]. \tag{A.191}$$

The Poynting vector can be averaged as

$$< \mathbf{Y} >= \frac{1}{4\mu_0}(\mathbf{E}_1^* \times \mathbf{B}_1 + \mathbf{E}_1 \times \mathbf{B}_1^*)e^{2\phi_i}. \tag{A.192}$$

Similarly, the average of electromagnetic field energy density per unit time is

$$\left\langle \frac{\partial W}{\partial t} \right\rangle \equiv \left[\frac{\omega_i}{2\mu_0}\mathbf{B}_1 \cdot \mathbf{B}_1^* + \frac{1}{2}\left[\omega_i \mathbf{E}_1^* \cdot \overleftrightarrow{\epsilon_H} \cdot \mathbf{E}_1 + \omega_r \mathbf{E}_1 \cdot \overleftrightarrow{\epsilon_A} \cdot \mathbf{E}_1^*\right]\right]e^{2\phi_i}, \tag{A.193}$$

where the Hermitian and the anti-Hermitian part of a dielectric tensor are

$$\overleftrightarrow{\epsilon} = \left(\frac{\overleftrightarrow{\epsilon} + \overleftrightarrow{\epsilon}^\dagger}{2}\right) + \mathrm{i}\left(\frac{\overleftrightarrow{\epsilon} - \overleftrightarrow{\epsilon}^\dagger}{2\mathrm{i}}\right) \equiv \overleftrightarrow{\epsilon}_H + \mathrm{i}\overleftrightarrow{\epsilon}_A, \tag{A.194}$$

$$\epsilon_{ij}^\dagger \equiv \epsilon_{ji}^*, \tag{A.195}$$

$$\overleftrightarrow{\epsilon}_H^\dagger = \overleftrightarrow{\epsilon}_H, \ \overleftrightarrow{\epsilon}_A^\dagger = -\overleftrightarrow{\epsilon}_A. \tag{A.196}$$

Even if the decaying of a wave amplitude ω_i equals to zero, the wave energy can be damped due to the anti-Hermitian part of a dielectric tensor. The physical meaning of this term is a work per unit time and volume by electric field into charged particles

$$\frac{\omega_r}{2}\mathbf{E}_1^* \cdot \overleftrightarrow{\epsilon}_A \cdot \mathbf{E}_1 = \frac{\omega_r}{2}\text{Re}[\mathbf{E}_1^* \cdot (-\mathrm{i})\overleftrightarrow{\epsilon} \cdot \mathbf{E}_1] = \frac{1}{2}\text{Re}[\mathbf{E}_1^* \cdot \mathbf{j}_1] = \overline{\mathbf{E} \cdot \mathbf{j}}. \tag{A.197}$$

Then let propagation angle ψ be 0, wave energy absorption per unit time and volume is

$$P_{abs} = \frac{\epsilon_0 \omega_r}{2} \left(|E_x|^2 \text{Im}[K_{xx}] + |E_y|^2 \text{Im}[K_{yy}] + |E_z|^2 \text{Im}[K_{zz}] \right.$$

$$\left. + 2\text{Im}[E_x^* E_y]\text{Re}[K_{xy}] + 2\text{Im}[E_y^* E_z]\text{Re}[K_{yz}] + 2\text{Re}[E_x^* E_z]\text{Im}[K_{xz}] \right). \qquad (A.198)$$

For a uniform plasma, we can evaluate the power absorption by solving a dispersion relation and a polarization for it.

The series expansion of a dielectric tensor provides the finite Larmor radius (FLR) effects for each order cyclotron harmonic damping:

$$K_0 = \sum_s \frac{2\omega_{ps}^2 \lambda_s}{\omega k_z v_{sL}} [Z(\zeta_{s0}) - \frac{1}{2}[Z(\zeta_{s1}) + Z(\zeta_{s-1})]] + \cdots, \qquad (A.199)$$

$$K_1 = 1 + \sum_s \frac{\omega_{ps}^2}{2\omega k_z v_{sL}} [[Z(\zeta_{s1}) + Z(\zeta_{s-1})](1 - \lambda_s) + \lambda_s[Z(\zeta_{s2}) + Z(\zeta_{s-2})]] + \cdots, \quad (A.200)$$

$$K_2 = i \sum_s \frac{\omega_{ps}^2}{2\omega k_z v_{sL}} [[-Z(\zeta_{s1}) + Z(\zeta_{s-1})](1 - 2\lambda_s) - \lambda_s[Z(\zeta_{s2}) - Z(\zeta_{s-2})]] + \cdots, \quad (A.201)$$

$$K_3 = 1 - \sum_s \frac{\omega_{ps}^2 \lambda_s}{\omega k_z v_{sL}} [\zeta_{s0} Z'(\zeta_{s0})(1 - \lambda_s) - \frac{\lambda_s}{2}[\zeta_{s1} Z'(\zeta_{s1}) + \zeta_{s-1} Z'(\zeta_{s-1})]] + \cdots, \quad (A.202)$$

$$K_4 = \sum_s \frac{\omega_{ps}^2 \sqrt{\lambda_s}}{2\sqrt{2}\omega k_z v_{sL}} [Z'(\zeta_{s1}) - Z'(\zeta_{s-1})] + \cdots, \qquad (A.203)$$

$$K_5 = i \sum_s \frac{\omega_{ps}^2 \sqrt{\lambda_s}}{\sqrt{2}\omega k_z v_{sL}} [Z'(\zeta_{s0}) - \frac{1}{2}[Z'(\zeta_{s1}) - Z'(\zeta_{s-1})]] + \cdots. \qquad (A.204)$$

The imaginary parts of Z and Z' functions contribute to damping effects.

A.5   Mode Conversion Theory

In this section, the theory of mode conversion efficiency with X-Wave injection from low field side is reviewed. The conversion efficiency from an electromagnetic wave into an EBW is a function of density, magnetic field strength and gradients of them. K.G. Budden carried out an investigation of mode conversion efficiency [10]. He constructed a model of a refractive index profile at the vicinity of the UHR, and obtained analytical solutions, i.e. Whittaker function which is one of a confluent hypergeometric function. Assuming perpendicular propagation ($\cos\theta = 0$, $\mathbf{k} \parallel \hat{x}$), inhomogeneous in the x-direction and uniform in the y-direction, Equation (A.53) can be represented as

$$\frac{d^2 E_y}{d\xi^2} + \Phi(\xi)E_y = 0, \qquad (A.205)$$

where

$$\xi \equiv \frac{\omega x}{c}, \qquad \text{(A.206)}$$

$$\Phi(\xi) \equiv \frac{S^2 - D^2}{S}, \qquad \text{(A.207)}$$

where parameters S and D are defined in Eq. (A.40) and (A.41). K.G. Budden made the model of $\Phi(\xi)$, which is called potential function and approximately corresponds to the square of refractive index, (note that the notation of this paper differs from Budden's one)

$$\Phi(\xi) = \gamma - \frac{\beta}{\xi}. \qquad \text{(A.208)}$$

This model represents that the location of the UHR corresponds to $\xi = 0$ and $\sqrt{\gamma}$ corresponds to $n_\perp$ for sufficiently large ξ. Furthermore the location of the R-Cutoff is at $\xi = \beta/\gamma$. Refractive index of X-wave modeled by K.G. Budden is shown in Fig. A.4. By defining

$$\zeta \equiv 2i\sqrt{\gamma}\xi, \qquad \text{(A.209)}$$

$$-\frac{i}{2}\frac{\beta}{\sqrt{\gamma}} \equiv -\frac{i}{2}\eta \equiv \kappa, \qquad \text{(A.210)}$$

Eq. (A.205) can be written as

$$\frac{d^2 E_y}{d\zeta} + \left(-\frac{1}{4} - \frac{i\eta/2}{\zeta} \right) E_y = 0. \qquad \text{(A.211)}$$

Equation (A.211) is the special case of Whittaker's differential equation. General solutions of Eq.(A.211) are

$$E_y = c_1 W_{\kappa,1/2}(\zeta) + c_2 W_{-\kappa,-1/2}(-\zeta), \qquad \text{(A.212)}$$

where c_1 and c_2 are arbitrary constants which depend on boundary conditions. The function $W_{\kappa,\mu}$ denotes the Whittaker function [3].

In order to investigate the mode conversion efficiency, the asymptotic form of Whittaker functions $W_{\kappa,\mu}(\zeta)$ are used. Let ξ be ∞, then

$$W_{\kappa,1/2}(\zeta) \sim \zeta^\kappa e^{-z/2} = |2\sqrt{\gamma}\xi|^{-i\eta/2} e^{-\pi\eta/4} e^{i\sqrt{\gamma}\xi}, \qquad \text{(A.213)}$$

$$W_{-\kappa,1/2}(-\zeta) \sim \left(\zeta^{-\kappa} e^{z/2} - \frac{2\pi i}{\Gamma(\frac{1}{2} - \mu + \kappa)\Gamma(\frac{1}{2} + \mu + \kappa)} \zeta^\kappa e^{-\zeta/2} \right) e^{i\pi\kappa}$$

$$= |2\sqrt{\gamma}\xi|^{i\eta/2} e^{3\pi\eta/4} e^{-i\sqrt{\gamma}\xi} - \frac{2\pi i}{\Gamma(-i\eta/2)\Gamma(1 - i\eta/2)} |2\sqrt{\gamma}\xi|^{-i\eta/2} e^{\pi\eta/4} e^{i\sqrt{\gamma}\xi}, \qquad \text{(A.214)}$$
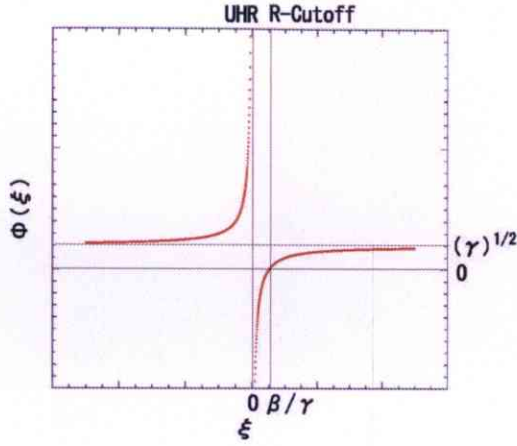
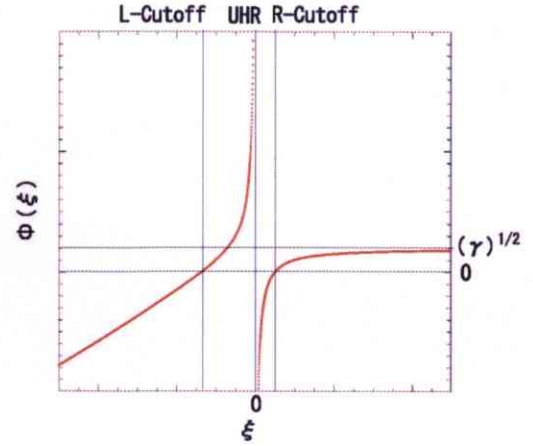Figure A.4: Refractive index of X-wave modeled by K. G. Budden.

Figure A.5: Refractive index of X-wave modeled by A. K. Ram.

and for $\xi \to -\infty$

$$W_{\kappa,1/2}(\zeta) \sim \zeta^\kappa e^{-\zeta/2} = |2\sqrt{\gamma}\xi|^{-i\eta/2} e^{\pi\eta/4} e^{-i\sqrt{\gamma}\xi}, \tag{A.215}$$

$$W_{-\kappa,1/2}(-\zeta) \sim \zeta^{-\kappa} e^{i\pi\kappa} e^{\zeta/2} = |2\sqrt{\gamma}\xi|^{i\eta/2} e^{\pi\eta/4} e^{-i\sqrt{\gamma}\xi} \tag{A.216}$$

are obtained. Note that we assumed the $\exp(-i\omega t)$ of time dependence. Thus for $\xi \to \infty$, $W_{\kappa,1/2}(\zeta)$ represents an incoming wave (toward $\xi = 0$), whereas $W_{-\kappa,1/2}(-\zeta)$ represents an outgoing wave. For $\xi \to -\infty$, $W_{\kappa,1/2}(\zeta)$ represents an outgoing wave while $W_{-\kappa,1/2}(-\zeta)$ represents combination of an incoming wave and an outgoing wave. In this model, the relevant solution to Eq.(A.211) is $W_{-\kappa,1/2}(-\zeta)$ because of no source of wave at $\xi \to -\infty$. The ratio of the amplitude of an incident wave to a reflected wave gives the reflection coefficient,

$$|R| = \frac{2\pi \exp(-\pi\eta/2)}{|\Gamma(-i\eta/2)\Gamma(1-i\eta/2)|} = 1 - e^{-\pi\eta}. \tag{A.217}$$

Similarly the ratio of the amplitude of an incident wave to a transmission wave gives the transmission coefficient,

$$|T| = e^{-\pi\eta/2}. \tag{A.218}$$

The conversion efficiency is written as

$$C = 1 - |R^2| - |T^2| = e^{-\pi\eta}(1 - e^{-\pi\eta}), \tag{A.219}$$

where η is called the tunneling parameter which means the product of wave number in vacuum and distance from the R-Cutoff to the UHR. The maximum mode conversion efficiency with Budden's model is $\frac{1}{4}$ when $|T|^2 = \frac{1}{2}$ is satisfied.

166

A.K. Ram investigated excitation, propagation and damping of an EBW [61][60]. In his theory, the effect of reflection of a transmitted X-Wave at the L-Cutoff was considered. Figure A.5 shows the refractive index profile of an X-Wave in his model. The term $\Psi(\xi)$ in Eq.(A.205) is written in Ram's model as

$$\Phi(\xi) = \begin{cases} \gamma - \dfrac{\beta}{\xi} & \xi > 0 \\[2mm] \alpha\xi + \gamma' - \dfrac{\beta}{\xi} & \xi < 0, \end{cases} \tag{A.220}$$

which is shown in Fig. A.5 In this case, the mode conversion efficiency is written as follows:

$$C(\eta, \phi) = 4e^{-\pi\eta}(1 - e^{-\pi\eta})\cos^2(\phi/2 + \theta). \tag{A.221}$$

Here θ is the phase of $\Gamma(-i\eta/2)$ and ϕ is determined by all of the locations of the R-Cutoff, the L-Cutoff and the UHR. In this case, completely mode conversion may occur if the following two waves are same amplitude and the phase difference is π. One is the X-wave reflected at the R-Cutoff directly, the other is X-wave which tunnels an evanescent region, and reflected at the L-Cutoff, and again tunnels an evanescent region. The tunneling parameter η is important for the mode conversion. Since η corresponds to the distance from the UHR and the R-Cutoff, it is obtained by using profiles of density and magnetic field strength and of those gradient length:

$$\eta = \frac{\Omega_e L_n}{c}\frac{\alpha}{\sqrt{\alpha^2 + 2(L_n/L_B)}}\left(\frac{\sqrt{1+\alpha^2} - 1}{\alpha^2 + (L_n/L_B)\sqrt{1+\alpha^2}}\right)^{1/2}, \tag{A.222}$$

where $\alpha \equiv \dfrac{\omega_{pe}}{\Omega_e}$, $L_n \equiv \dfrac{n}{|dn/dr|}$ and $L_B \equiv \dfrac{B}{|dB/dr|}$ [61].